Improved image speckle noise reduction and novel dispersion cancellation in Optical Coherence Tomography

by

Prabakar Puvanathasan

A thesis
presented to the University of Waterloo
in fulfillment of the
thesis requirement for the degree of
Master of Applied Science
in
Systems Design Engineering

Waterloo, Ontario, Canada, 2008

Abstract

Optical coherence tomography (OCT) is an innovative modern biomedical imaging technology that allows in-vivo, non-invasive imaging of biological tissues. At present, some of the major challenges in OCT include the need for fast data acquisition system for probing fast developing biochemical processes in biological tissue, for image processing algorithms to reduce speckle noise and to remove motion artefacts, and for dispersion compensation to improve axial resolution and image contrast.

To address the need for fast data acquisition, a novel, high speed ($47,000$ A-scans/s), ultrahigh axial resolution ($3.3\mu m$) Fourier Domain Optical Coherence Tomography (FD-OCT) system in the $1060nm$ wavelength region has been built at the University of Waterloo. The system provides $3.3\mu m$ image resolution in biological tissue and maximum sensitivity of $110dB$. Retinal tomograms acquired in-vivo from a human volunteer and a rat animal model show clear visualization of all intra-retinal layers and increased penetration into the choroid.

OCT is based on low-coherence light interferometry. Thus, image quality is dependent on the spatial and temporal coherence properties of the optical waves backscattered from the imaged object. Due to the coherent nature of light, OCT images are contaminated with speckle noise. Two novel speckle noise reduction algorithms based on interval type II fuzzy sets has been developed to improve the quality of the OCT images. One algorithm is a combination of anisotropic diffusion and interval type II fuzzy system while the other algorithm is based on soft thresholding wavelet coefficients using interval type II fuzzy system.

Application of these novel algorithms to Cameraman test image corrupted with speckle noise ($\sigma_n^2 = 0.1$) resulted in a root mean square error (RMSE) of 0.07 for both fuzzy anisotropic diffusion and fuzzy wavelet algorithms. This value is less compared to the results obtained for Wiener ($RMSE = 0.09$), adaptive Lee ($RMSE = 0.09$), and median ($RMSE = 0.12$) filters. Applying the algorithms to optical coherence tomograms acquired in-vivo from a human finger-tip show reduction in the speckle noise and image SNR improvement of $13dB$ for fuzzy anisotropic diffusion and $11db$ for fuzzy wavelet. Comparison with the Wiener (SNR improvement of $3dB$), adaptive Lee (SNR improvement of $5dB$) and median (SNR improvement of $5dB$) filters, applied to the same images, demonstrates the better performance of the fuzzy type II algorithms in terms of image metrics improvement.

Micrometer scale OCT image resolution is obtained via use of broad bandwidth light sources. However, the large spectral bandwidth of the imaging beam results in broadening of the OCT interferogram because of the dispersive properties of the imaged objects. This broadening causes deterioration of the axial resolution and as well as loss of contrast in OCT images. A novel even-order dispersion cancellation interferometry via a linear, classical interferometer has been developed which can be further expanded to dispersion cancelled OCT.

Acknowledgements

This work would not be possible without the guidance, support and experience of my supervisors Prof. Kostadinka Bizheva (Physics & Astronomy) and Prof. Hamid Tizhoosh (SYDE). I would also like to thank Prof. K.J. Resch (Physics & Astronomy) with the dispersion cancellation interferometry experiment. I would like to thank P. Forbes and Z. Ren for assistance with the imaging of human patient and animals. Finally, I would like to thank all the little people who made this possible.

Dedication

This is dedicated to my family.

Contents

List of Tables

List of Figures

Chapter 1

Introduction

Humans are constantly being threatened by various type of diseases. There is constant need for novel imaging techniques that can be used in medicine for earlier and improved diagnosis of various diseases and for monitoring the effect of therapeutic treatment. During the past decades, non-invasive biomedical imaging techniques such as ultrasound, Computed Tomography (CT), Magnetic Resonance Imaging (MRI), and Positron Emission Tomography (PET) have played vital role in diagnostic medicine. Even though some of these techniques allow three-dimensional (3D) visualization; they provide limited spatial resolution in the range of few millimetres (mm) [11]. MRI imaging can provide large spatial resolution, but at the expense of prolonged imaging procedure. There is a trade-off between the image spatial resolution and image acquisition time.

Over the past few decades, technological advancements in optical devices and laser technology have given birth to a novel non-invasive optical biomedical imaging technique called optical coherence tomography (OCT). OCT is an imaging technology that allows for in vivo, non-invasive high-resolution, two- or three dimensional cross-sectional imaging of the morphology of partially transparent and highly scattering biological tissues on a microscopic level [11]. The axial OCT resolution can range from $0.5\mu m$ to few micrometers, while the penetration depth in biological tissue is limited to 1.5 to $2mm$. Hence, OCT is uniquely suited for performing non-invasive optical biopsy of biological tissues such as skin, cornea, retina, arterial plaques, cervical and gastro-intestinal epithelium, etc. In addition to structural imaging, OCT can also provide information about the blood flow, birefringence, and physiological information.

Currently Ophthalmic OCT is the most advanced application of this imaging technique with clinical ophthalmic OCT systems being manufactured and sold by companies around the world. The popularity and the commercial success of ophthalmic OCT are largely due to the fact that ocular media is transparent and thus provides direct access to the retina, and the retina is only $500\mu m$ thick.

1.1 Problem Statement

OCT technology is more than a decade old. However, from an engineering point of view there are still many challenges related to improving the performance of this imaging technique. Retinal imaging with ophthalmic OCT invovles very high scanning rates to suppress micro saccades and other types of biological noise (breathing rate, heart rate, etc.) when large volumes of retinal tissue are raster scanned with high spatial resolution. This requires a system with high-speed data acquisition, data processing, and real-time image display. Another challenge is the need for development of micrometer scale axial resolution retinal OCT system in the 1060nm wavelength range. This will serve a dual purpose - provide access to the choroid for imaging of choroid blood vessel network and measurement of choroid blood flow; and provide an opportunity for probing the health of retinal neurons (photoreceptors) by measuring their response to light stimulation. Other challenges include the development of image processing algorithms for speckle noise removal, segmentation and analysis; as well as alternative methods for combating the adverse effect of material dispersion on the OCT axial resolution. Presence of speckle noise in the OCT tomograms results in loss of image contrast, signal-to-noise ratio (SNR) and in general degrades the overall image quality. Material dispersion of polychromatic light degrades both axial OCT resolution and image contrast as a function of depth within the imaged object.

This MSc thesis focuses on some of the engineering and scientific problems in OCT technology. Specifically:

1. Improvement of the data acquisition rate of an Ophthalmic OCT system designed for retinal imaging in the 1060nm wavelength region.
2. Development of speckle noise reduction algorithms for OCT
3. Development of a dispersion cancellation method for OCT.

This thesis has the following organization: Chapter 2 describes in detail the design and performance of an Ophthalmic OCT system operating in the 1060nm wavelength region and our approach to achieving 10 times improvement in the data acquisition rate as compared to previously published system designs. Chapter 3 defines and discusses speckle noise in OCT tomograms, its origins and its negative effect on the OCT image contrast and overall image quality. Chapter 4 introduces the interval-type II fuzzy sets. Chapters 5 and 6 discuss two novel speckle noise reduction algorithms based on combining fuzzy type II sets with wavelet and anisotropic diffusion respectively. Chapter 7 compares the results obtained from testing the algorithms on a standard test image and OCT tomograms of human finger tip and human retinal images. The second problem in OCT, material dispersion, and a novel solution for removing even-order dispersion is discussed in chapter 8. Conclusions and future works are then presented based on the algorithm analyzes and dispersion compensated interferometry (Chapter 9).

Chapter 2

Ultra-high resolution fourier domain optical coherence tomography (UHR-FD-OCT)

The principle operation of OCT imaging is similar to conventional ultrasound B-mode imaging, however rather than recording the pulsed sound echo OCT detects the intensity and echo time delay of light, back-scattered or back-reflected from various features within the imaged tissue [56]. OCT data sets are either 2D or 3D and it represent the variation in optical back-scattering or back-reflection in a cross-sectional plane or volume within the imaged object.

Fig. 2.1 shows the schematic for the acquisition of a single A-scan (the building block of any 2D and 3D OCT images) in the eye. By directing light into the eye and measuring the echo time delay and intensity of back-reflection or back-scattering from different structures, the distance measurement can be obtained. A two dimensional reflectivity profile (OCT tomogram consisting of a number of single line measurements: A-scans) of the imaged object is created by scanning the optical beam transversely (X or Y) over the sample. The two-dimensional data set can be post-processed and displayed as a gray scale or a false color image of the sample. Similarly, a three dimensional reflectivity profile is created by scanning the optical beam in both X and Y direction. Tissues that have different optical properties back-scatter the incident light differently while boundaries between different tissues back-reflect the incident optical beam [56]. By measuring the echo time delay of light that is back-reflected or back-scattered from the different structures at varying axial distances the distances and dimensions of different tissues can be found [15]. Distance information can be found by Eqn. 2.1. In Eqn. 2.1, ΔT is the echo delay, Δz is the distance that the echo travels, and v is the velocity of the light wave [56].

$$\Delta T = \frac{\Delta z}{v} \tag{2.1}$$

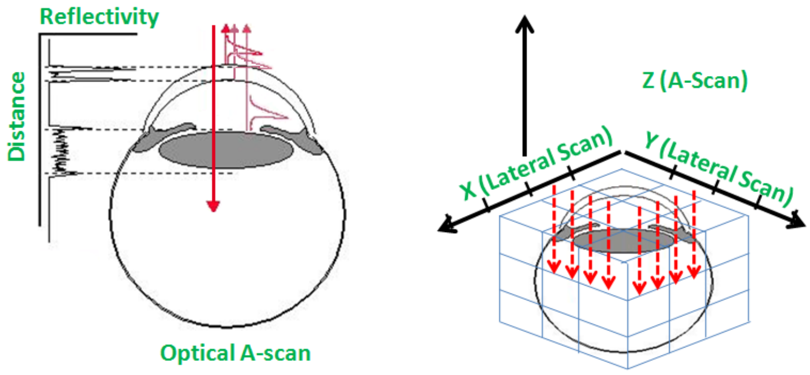

(a) (b)

Figure 2.1: Optical coherence tomography imaging of a human eye. a) Acquisition of an OCT tomogram, comprised of a number of A-scans and each A-scan represents a cross-sectional reflectivity profile of the imaged object. b) Surface of the tissue sample is divided into imaginary grid with each block in the grid represents a pixel in the OCT image. 3D data set is obtained by lateral scanning in both X and Y direction. 2D data set is obtained by scanning in either X or Y direction. A single A-scan corresponds to the depth profile in Z direction.

2.1 Theory of low coherence interferometry

OCT uses low-coherence interferometry to achieve ultrahigh-resolution time and distance measurements for imaging. Coherence length is the propagation distance from the coherent light source where the electromagnetic wave maintains a specified degree of coherence. Fig. 2.2 demonstrates the principle of operation of OCT. The light emitted from the light source is divided by the beamsplitter into two beams: the reference beam and the sample beam. The reference beam is directed towards the reference mirror while the sample beam is directed towards the sample. The reference beam reflects from the reference mirror while the sample beam back-reflects or back-scatters from the tissue sample being imaged. The back-reflected beams with electric fields E_R and E_S, interfere at the beamsplitter and a portion of the interference light is detected with a photo-detector, E_O [56]:

$$E_O(t)\ E_R(t) + E_S(t) \tag{2.2}$$

The photo detector measures the intensity of the output light from the interferometer which is proportional to the square of the electric field [56]. If there is a single reflecting surface at the tissue sample, then Eqn. 2.3 represents the output intensity of the interferometer as a function of E_R, E_S, and ΔL (path difference) [56].

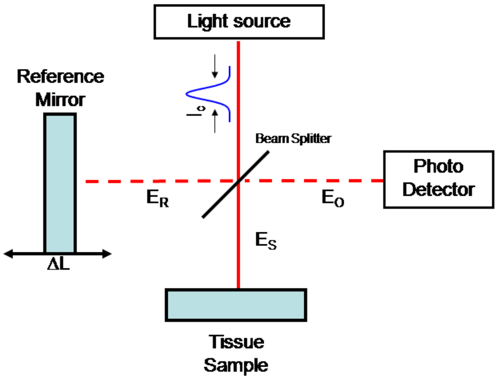

Figure 2.2: OCT system is based on a Michelson Interferometer along with a low coherence light source. A beam from the light source is split by a beam splitter. The resulting beams traverse down the reference and sample paths. The interference pattern of the back-reflected beams is registered with a photo detector.

$$I_O(t) \sim (1/4)|E_R|^2 + (1/4)|E_S|^2 + (1/2)E_R E_S cos(2 * (2\pi/\lambda) * \Delta L) \qquad (2.3)$$

Eqn. 2.3 shows that the output intensity from the interferometer will oscillate as a function of the path difference ΔL because of interference effects [56]. As the reference mirror is scanned, the path length of the reference beam will change which results in a variable time delay. This results in either destructive or constructive interference at the beamsplitter. Thus, interference effect can be seen in the output intensity as ΔL changes.

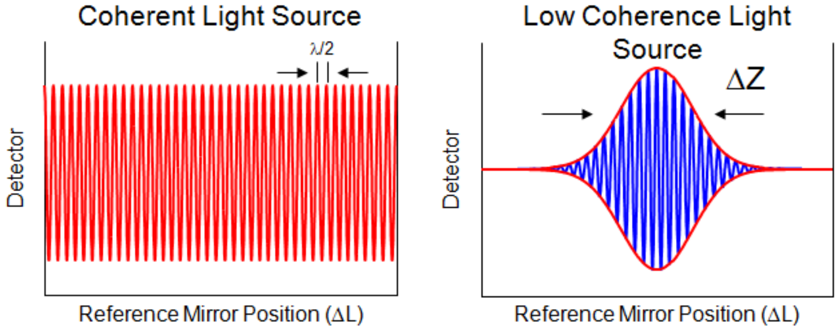

(a) (b)

Figure 2.3: a) When coherent light is used, interference occurs for all relative delays, ΔL. b) In contrast, if low-coherence light is used, interference occurs when the relative delay, ΔL, is less than the coherence length of the light.

When a coherent light source (long coherence length, I_c) is used, the back-reflected beams interfere and produce at the detector an interferogram with constant amplitude (see Fig. 2.3(a)). This will not be useful for precisely measuring the absolute position of a structure within a tissue because interference will be detected for wide range of ΔL changes. For applications in OCT, light with short coherence length (or low-coherence light) is required. When a low coherent light source is used, interference occurs only when the difference in the optical paths traversed by the two beams is smaller than the coherence length of the light source (i.e. $\Delta L < I_c$), and as a result the interferogram is amplitude modulated (see Fig. 2.3(b)). The magnitude of the interferogram is proportional to the amount of back-reflected light, while its time delay determines the position within the imaged object from which the back-reflected light had originated. The length ΔZ over which interference occurs (OCT axial resolution) is determined by the spectrum of the light source (coherence length of the light which is defined by λ_c and $\Delta\lambda$). OCT transverse resolution is determined by the imaging optics and the central wavelength (λ_c) of the light source. In summary, by measuring the interference at the output of the interferometer as ΔL is changed, the echo time delay of light can be found. The correlation between the back-reflected or back-scattered light from the sample and the reference light that has a known delay, results in the echo delay which is what the interferometer measures.

2.2 Principle of operation of Fourier-domain optical coherence tomography (FD-OCT)

The section above describes the principle of operation of "Time-domain OCT" (TD-OCT). In TD-OCT, the reference mirror is scanned to match the optical path from reflections within the sample to obtain the depth information. Since mechanical scanning of the reference mirror is limited to frequencies below 16kHz and there is an inverse dependence between the SNR and data acquisition speed of TD-OCT, this version of the OCT technology has limited biomedical applications. By using Fourier-Domain OCT (FD-OCT), the disadvantage of relatively slow image acquisition can be avoided. FD-OCT has the advantage that no moving parts are required and thus provides significant imaging speed and improved sensitivity [66].

Referring back to Fig. 2.2, in FD-OCT, the reference path (ΔL) is fixed and a spectrometer is used in place of the photo detector. In FD-OCT, also known as spectral-domain OCT (SD-OCT), depth-resolved information is encoded in the cross-spectral density function, as measured in the detection arm of an interferometer [8]. By measuring the echo time delay and magnitude of back-reflected or back-scattered light, cross-sectional images can be generated in the Fourier domain. When illuminated with a low-coherence light source, the light signal is back-reflected or back-scattered from different depths that correspond to different delays. This light signal interferes with the light from the reference path with a known delay. The interference fringe pattern is detected by a high-speed charged couple device (CCD) camera. By applying, discrete Fourier transform (DFT) to the spectral interference signal, the delay and the magnitude of the optical reflections from the sample can be detected as a function of τ or z. The cross-sectional image is obtained by scaling the Fourier transformed data and using a gray scale or false color map.

The axial image resolution, ΔZ, is inversely proportional to the bandwidth of the light source used for imaging:

$$\Delta z = \frac{2ln2}{\pi}\frac{\lambda_c^2}{\Delta\lambda} \tag{2.4}$$

where $\Delta\lambda$ is the full width half maximum (FWHM) of the light source and λ_c is the center wavelength. If there are N CCD pixel arrays, then the axial measurement range ΔL_z over which reflected signals can be measured is given by:

$$\Delta L_z = \frac{\Delta z}{2}\frac{N}{2} = \frac{ln2}{2\pi}\frac{\lambda_c^2}{\Delta\lambda}N \tag{2.5}$$

The total number of pixels carrying unique information about the axial scan is reduced by a factor of 2, because Fourier transform of the real spectrum has conjugate symmetry about the zero delay [66].

2.3 FD-OCT operating at 1060nm

This section presents the first FD-OCT system operating in the 1060nm wavelength range that combines high image acquisition speed (47,000 A-scans /s) and ultrahigh axial resolution (3.3m) in biological tissue, which was developed at the Biomedical Optics Imaging Lab (BOIL) at the University of Waterloo.

A schematic of the FD-OCT system is presented in Fig. 2.4. The output of a custom-built broad bandwidth superluminescent diode, SLD (Superlum Ltd., $\lambda_c = 1020nm, \Delta\lambda = 108nm$ and $P_{out} = 9mW$) is interfaced to a compact, fiber-based FD-OCT system. A fiber-optic isolator is used at the input to minimize back-reflections to the SLD that can affect negatively its performance. A broad bandwidth, 30/70 fiber coupler (Gould Fiberoptics) is used as a core of the FD-OCT system. The reference arm of the system is comprised of an achromatic collimator (LINUS, $f = 10mm$), a tunable dispersion compensation unit based on a pair of BK7 glass prisms, a focusing achromat lens (LINUS, $f = 10mm$) and an Ag mirror mounted on a translation stage. The sample arm of the FD-OCT system is interfaced to a modified slitlamp biomicroscope. The interference signal is detected with a custom designed, high performance spectrometer (P&P Optica Inc.), interfaced to a novel 1024 pixel linear array InGaAs CCD camera (SUI, Goodrich Corp.) with $47kHz$ readout rate. The spectrometer is custom designed for the $940-1120nm$ spectral range and provides average absolute grating efficiency $> 80\%$ over the entire spectral range, and spectral resolution of $0.18nm$.

Data is acquired with NI PCI-1428 a frame grabber (National Instruments) connected to a computer with an Intel Xeon CPU at 3.6 GHz and 2GB RAM. The detected spectrum, as a function of pixel number x, is given by [66]:

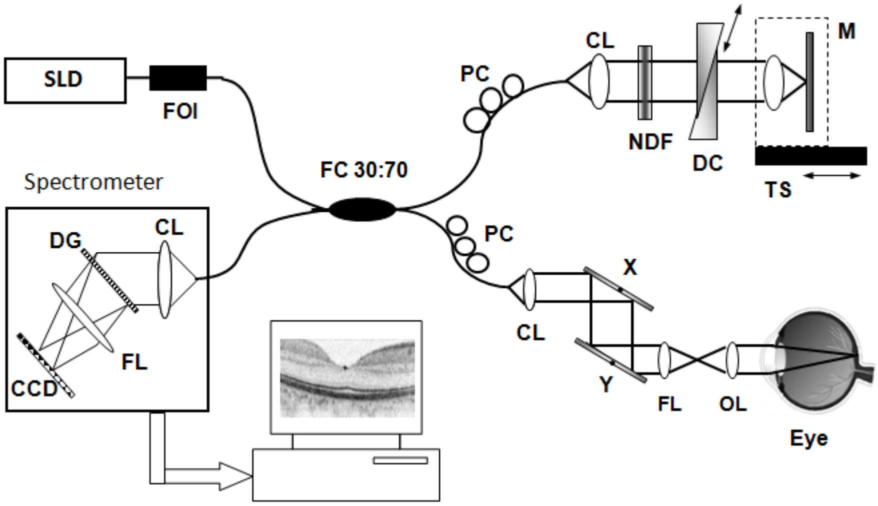

Figure 2.4: Diagram of the ultrahigh-resolution FD-OCT system: (CL) - collimating lenses, (DC) - dispersion compensation unit, (NDF) - neutral-density filters, (FOI) - fiberoptic isolator, (M) mirror, (PC) - polarization controllers, (SLD) superluminescent diode and (TS) - translation stage. The spectrometer consists of a collimating lens (CL), a volumetric diffraction grating (DG), a focusing lens (FL) and a high speed InGaAs CCD camera.

$$S_{out}(x) = |E_R(x)|^2 + 2Re\{E_R(x) * E_S(x)\} + |E_S(x)|^2 \tag{2.6}$$

where E_R is the reference arm field and E_S is the field from the sample. Last term in Eqn. 2.6 can be ignored, because the intensity from the sample is usually small compared to the intensity from the reference arm [66].

Fig. 2.5 depicts the processing algorithm. The data processing algorithm involves first subtracting from $S_{out}(x)$, the spectrum of the reference light obtained by blocking the tissue sample ($S_{reference}(x)$), which provides the pure interferometric signal $S_{int}(x)$ [66]:

$$S_{int}(x) = 2Re\{E_R(x) * E_S(x)\} = 2Re\{\sum_n (\sqrt{I_n(x) I_r(x)}) e^{i(x\tau_n + \Phi(x,\tau_n))}\} \tag{2.7}$$

In Eqn. 2.7, $S_{int}(x)$ is the sum of fringes that are generated by the interference of light reflected or back-scattered from different interfaces within the tissue sample with the light reflected from the reference mirror. By calibrating the spectrometer, the pixel numbers can be mapped to the corresponding wavelength. In the spectrometer, the data is available as an array of points evenly spaced in the wavelength domain. However, the fast Fourier transform (FFT) algorithms are most efficient when the data points are evenly spaced in the frequency domain (ω or k space) [10]. Hence, conversion from wavelength (λ) to frequency (ω or k space) must be

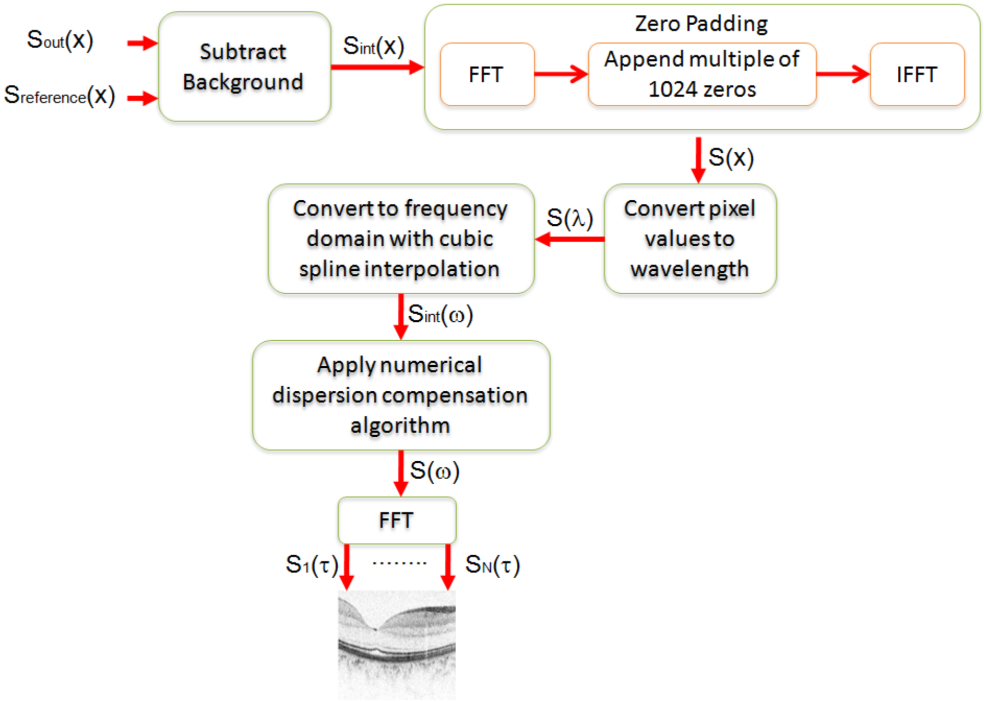

Figure 2.5: The interference spectrum is first zero padded to create finer sampling points. The finer sampled points are then rescaled to convert from wavelength to frequency. The resulting spectrum is Fourier transformed to calculate the axial A-scan. To generate an OCT image, N number of laterally scanned axial A-scans are used.

done prior to discrete Fourier transforming the data. This conversion requires the use of cubic interpolation since data must be evenly spaced. Interpolation of the spectral data is best performed with finer sampling [10]. Thus, prior to interpolation and conversion from pixel to wavelength, the spectral data is zero-padded to obtain finer sampling points [10, 8]. Once the data has been converted to frequency domain, the next step involves the application of a numerical dispersion compensation algorithm described in reference [66]. Then, taking the DFT of the result, gives us the processed A-scan as a function of τ (or z). To obtain the image, multiple laterally scanned A-scans are processed (I.e. 512 or 1024) in a single 2D frame. During real-time acquisition of the data, every 5th frame is shown on the computer screen due to the fast acquisition time but slow image processing time. Also, because of time limitations, numerical dispersion compensation is not done during real-time acquisition. It is only used during post-processing due to its time consuming iterative process.

2.3.1 System Analysis

To evaluate the optical transfer function of the FD-OCT system, both the direct output of the SLD spectrum (Fig. 2.6, dashed line) and the spectrum at the output

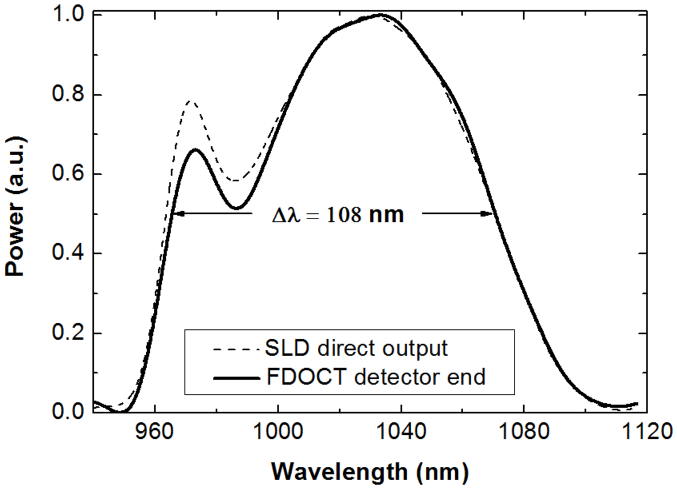

Figure 2.6: SLD spectrum measured with the high efficiency spectrometer directly at the source output (dashed line) and at the detector end of the FD-OCT system (solid line)

of the FD-OCT system (Fig. 2.6, solid line) were measured with the spectrometer. The results show preferential attenuation of the SLD spectrum at shorter wavelengths, partially due to wavelength dependent attenuation in the fiber coupler, as well as chromatic aberrations in the optics and polarization sensitive losses in the fiber optics. As a result, the spectral valley at $980nm$ drops close to the $3dB$ level. For measurements in air, or clear media with wavelength independent absorption, the FD-OCT system throughput can be optimized to the full spectral bandwidth of $108nm$, which results in $4.3\mu m$ (expected) and $4.5\mu m$ (measured) axial resolution, that corresponds to $3.3\mu m$ in biological tissue, assuming average tissue refractive index of 1.38. A representative axial point spread function (PSF), acquired in air from an Ag mirror, is shown in Fig. 2.7.

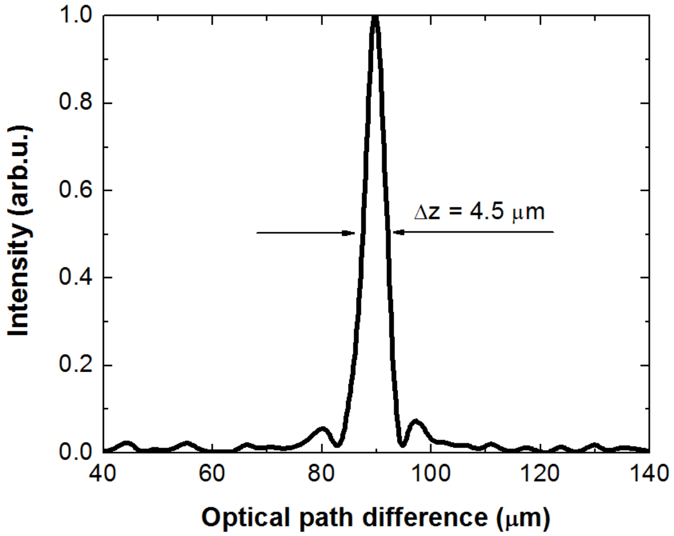

Figure 2.7: FD-OCT axial point-spread function measured from an Ag mirror

The small difference between the calculated and measured axial OCT resolution is most likely due to chromatic aberrations in the optics and finite pixel size of the CCD array. This is the second best axial OCT resolution achieved in the 1060nm wavelength region, superseded only by 4μm free-space axial resolution reported for a time domain OCT system interfaced to a supercontinuum based light source [43]. The loss of fringe visibility at the edges of the scanning range results in further degradation of the axial OCT resolution from 4.5μm at the zero delay to 5μm at 1.1mm imaging depth.

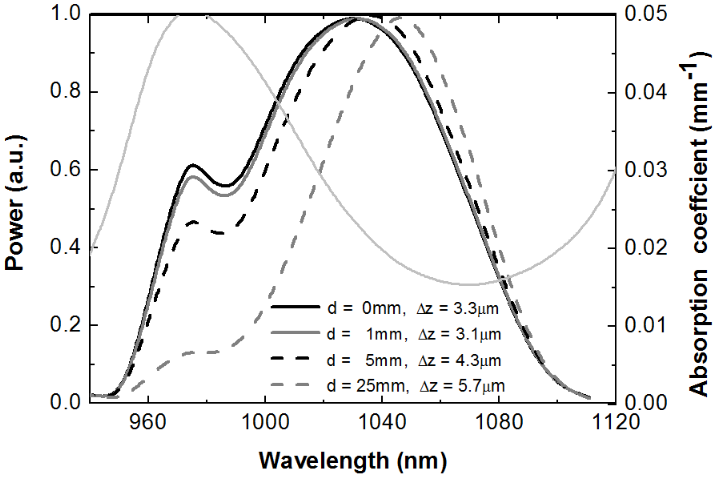

Figure 2.8: Simulation of the effect of water absorption (pale gray line) on the SLD spectral shape, central wavelength and OCT axial resolution, δz, as a function of the thickness, d, of the water layer

Since the height of the spectral valley at 980nm is susceptible to wavelength dependent water absorption and scattering in biological tissue, the effective SLD

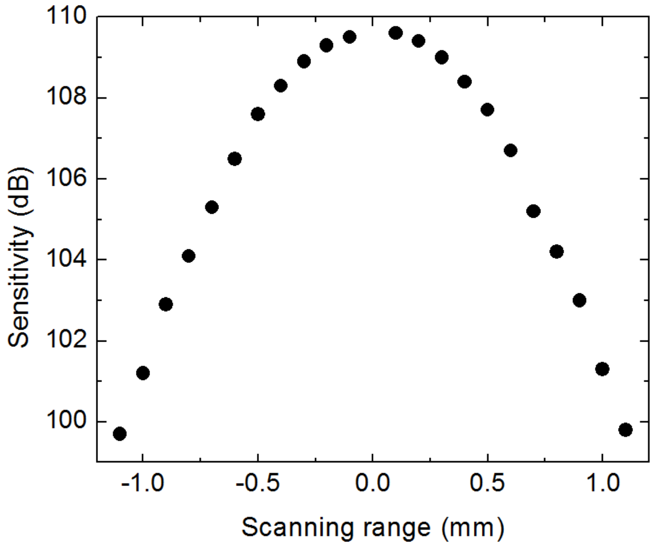

Figure 2.9: Sensitivity of the FD-OCT system, measured as a function of the optical path difference

spectral bandwidth in biological media is reduced, and the central wavelength is shifted to longer wavelengths, which results in broadening of FD-OCT PSF function. We have simulated the effect of water absorption on the spectral bandwidth and central wavelength of the SLD spectrum for variable thickness d of the water layer, that approximate ex-vivo imaging of excised tissue samples submerged in saline ($d = 1mm$), as well as the approximate water content of rat ($d = 5mm$) and human ($d = 25mm$) eye. The simulation results presented in Fig. 2.8 show no significant change of the FD-OCT axial resolution for the case of ex-vivo imaging of tissue samples, however 36% to 72% reduction in the FD-OCT axial resolution is expected for the cases of imaging rat and human eye respectively. The sensitivity of the FD-OCT system, measured as a function of the optical path difference is depicted in 2.9.

The FD-OCT resolution measurements were performed at a speed of $47,000$ A-scans/sec with $21\mu s$ exposure time and $47kHz$ read out rate. Maximum sensitivity of $110dB$ was achieved for $870\mu W$ optical power incident on the mirror at zero delay, while the sensitivity dropped by about $10dB$ at the end of the $1.1mm$ scanning range of the system. This degradation is associated with loss of fringe visibility caused by finite pixel width of the camera, the focused spot size on the CCD and resolution limiting aberrations induced by the spectrometer optics.

Chapter 3

Speckle noise

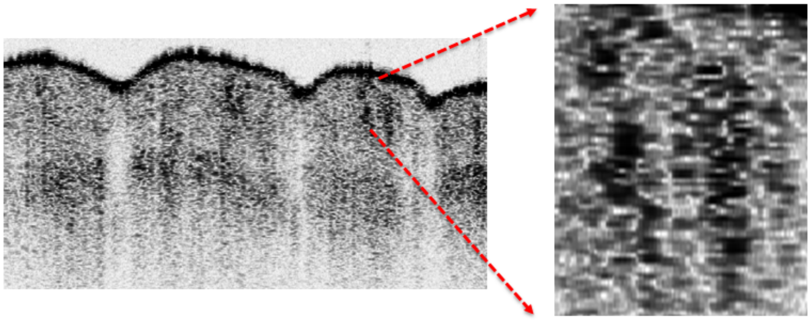

Figure 3.1: An OCT image of a human fingertip acquired in-vivo. The enlarged region shows the granular appearance of speckle noise which reduces the sharpness of the boundaries of the sweat glands.

Fig. 3.1 show the image obtained with the FD-OCT system mentioned in section 2.3. The word “coherence” in optical coherence tomography describes the weakness of this new imaging modality. OCT is based on interferometry of light with low coherence length, which utilizes the spatial and temporal coherence properties of optical waves backscattered from biological tissue [11]. As any imaging technique that is based on detection of coherent waves, OCT images are subjected to presence of speckle noise. The presence of speckle noise results in granular appearance of the image, which in turn obscures small or low reflectivity features and makes boundaries between highly scattering structures in tissue difficult to resolve [53].

Referring back to Fig. 2.2, when the optical path in the reference arm of the interferometer varies during the scanning procedure, a photocurrent is generated by the photo detector at the output of the interferometer. This photocurrent is proportional to the real part of the cross-correlation product of the optical field U_s back-reflected or back-scattered from the sample and reference optical field U_r [53]:

$$i_d \backsim Re < U_r U_s^* > \tag{3.1}$$

The brackets <> in Eqn. 3.1 denotes an average over time and space. The photocurrent can be expressed in terms of the optical path difference ΔL between the two arms [53],

$$i_d(\Delta L) = K|g(\Delta L)|cos[2\pi\nu_0\Delta L + \phi(\Delta L)] \tag{3.2}$$

In Eqn. 3.2, K is a constant that relates optical and electronic variables and ν_0 denotes the center frequency of the light source used for imaging. $|g(\Delta L)|$ and $\phi(\Delta L)$ are the argument and phase of the cross-correlation of Eqn. 3.1 respectively. The sensitivity of the photocurrent to the phase ($\phi(\Delta L)$) that makes OCT susceptible to the effects of speckle [53]. Speckle is generated by the interference of waves with the random phases and is dependent on the wavelength of the imaging beam and the structural details of the imaged object. In addition, speckle is influenced by optical properties and motion of the target object and the aperture of the detector. The sum of the multiple backscattered waves arising from within the sample carries both information (signal carrying speckle) and noise (signal degrading speckle). A thorough analysis of the speckle pattern in OCT is beyond the scope of this thesis, but for now the interest lies in removing the signal degrading speckle noise.

3.1 Noise model

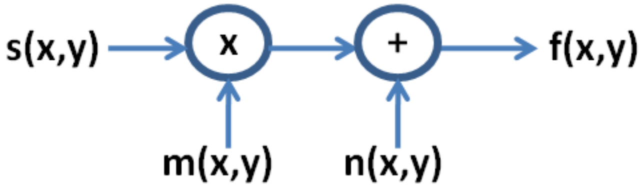

Figure 3.2: System diagram representing the noise model in OCT imaging system. $s(x, y)$ is the noise free OCT image, $f(x, y)$ is the noise observation of $s(x, y)$, $m(x, y)$ and $n(x, y)$ are the speckle and additive noise.

The system diagram presented in Fig. 3.2 represents the noise model in OCT imaging system [3, 64]. In OCT, the observed image signal, $f(x, y)$, is corrupted by both a multiplicative and additive noise. The speckle noise is being approximated as multiplicative noise [3, 64]. Eqn. 3.3 represents the system diagram in Fig. 3.2.

$$f(x, y) = s(x, y)m(x, y) + n(x, y) \tag{3.3}$$

(x, y) is the spatial location in the image plane, $s(x, y)$ represents the noise free OCT image, $f(x, y)$ is the noise observation of $s(x, y)$, $m(x, y)$ and $n(x, y)$ are the speckle (approximated as multiplicative) and additive noise respectively. In Eqn. 3.3, the additive noise component comes from the shot noise, light intensity noise, and electronic noise inherent in OCT imaging system and can be ignored because speckle noise is the more dominant term [64]. For developing speckle reduction filters, multiplicative noise has to be transformed into additive noise. This can be achieved by use of logarithmic transformation, resulting in Eqn. 3.4.

$$f_L(x, y) = s_L(x, y) + m_L(x, y) \tag{3.4}$$

To obtain the noise free image $s_L(x, y)$, image processing algorithm is needed that would remove the unwanted signal $m_L(x, y)$ from the observed signal $f_L(x, y)$.

3.2 Existing speckle noise reduction techniques in OCT

Speckle in OCT tomograms is dependent both on the wavelength of the imaging beam and the structural details of the imaged object [53]. Therefore, speckle carries information about the morphology of the imaged object as well as a noise component, and the latter is responsible for the granular appearance of OCT images. Development of successful speckle noise reduction algorithms for OCT is particularly challenging, because of the difficulty in separating the noise and the information components of a speckle pattern.

In the past, extensive research has been conducted both in the fields of medical imaging and remote sensing for suppressing speckle noise. Many methods have been developed to improve the image quality degraded by speckle noise. Several speckle-reduction procedures are described by [54]. In this work, speckle reduction techniques in OCT are classified into four categories: polarization diversity, spatial compounding, frequency compounding, and digital signal processing. These categories can be summed into either numerical image processing algorithms, or alternative detection schemes of the OCT system design. Polarization diversity, spatial compounding, and frequency compounding are based on modification to the OCT system design.

Zero adjustment procedure is a digital signal processing technique that detects and reduces speckle in the phase space [22, 67]. Speckle denoising using ZAP has a number of deficiencies with main set back of image blurring [67]. CLEAN, another digital signal processing technique based on iterative point-deconvolution that was developed originally for use in radio astronomy, was investigated for speckle reduction in OCT images [52]. Adaptive filters have been widely used in SAR, ultrasound and OCT images to reduce speckle. Adaptive weighted median filter was applied for speckle suppression in medical ultrasonic images [32]. Rotating Kernel Transformation, an adaptive speckle suppression filter was applied to coronary OCT images [48]. Filtering techniques based on the rotating kernel transform can produce good contrast enhancement of image features, however they result in significant edge blurring when strong noise reduction is required [3]. Modified Lee and Kuan adaptive filters have been applied to SAR speckle reduction [33]. Higher statistical moments based adaptive filters has been applied to ultrasonic images [21]. Neural network has been applied to ultrasound images to suppress speckle noise [63].

A wavelet based soft thresholding technique has been previously applied to OCT images corrupted by speckle noise [3]. It computes the undecimated wavelet transform and applies soft thresholding to the horizontal, vertical, and diagonal subbands. The threshold is obtained using the statistics of the wavelet coefficients. The wavelet based technique described in [3] does not reduce the image sharpness significantly but the execution time for the algorithm is about 7 min using Matlab implementation. In a different study [41], the performance of various digital filters was compared by applying the algorithms to an OCT tomogram of a bovine retina acquired ex-vivo. More specifically, the results presented in reference [41] indicate that non-orthogonal wavelet-transform-based filters together with enhanced Lee and adaptive Wiener filters can reduce speckle and increase SNR while preserving fine details of the image. The non-orthogonal wavelet-transformed filter applies a separate threshold for each individual wavelet level. Enhanced Lee filter is an improved version of the original Lee filter which a minimization of the mean square error estimate of the true image with the multiplicative noise model transformed into an independent additive noise [33]. The Adaptive Wiener filter is also determined from the minimization of the mean square error estimate of the true image and the filter is implemented based on the local statistics (mean and variance) within the smoothing window centered on each pixel of the input image [41].

Anisotropic diffusion is another digital algorithm that has been previously applied for speckle noise reduction in OCT images. For example, in references [12, 13, 64] the gradient of the image is used for the calculation of the diffusion coefficient with no consideration to the actual noise present. In reference [49] the performance of two algorithms based on anisotropic diffusion was compared as they were applied to speckled OCT images. The main problem with any image processing algorithm based on anisotropic diffusion is the large number of iterations, necessary to reach a steady state solution [4]. As a result, longer computational time is required, along with more blurring, resulting in loss of sharpness at edges that correspond to real image features. Also for images with a large noise component, anisotropic diffusion will have no significant effect [4].

In addition to algorithms, modifications to the OCT system design have been suggested to reduce speckle noise. One of the techniques uses a multimode fiber and a spatially coherent broadband light source to reduce speckle noise [26]. Spatial and frequency compounding are alternative techniques for reducing speckle noise in OCT images, however, these techniques require significant modifications to the design of the OCT system. A frequency compounding technique that is based on summing two incoherent, independent interferometric signals was investigated in [34] and results shows increased image contrast without loss of resolution. Recently, a spatial diversity technique based on shifting the focal plane of the probe beam was introduced to suppress speckle noise [60]. In a different study, angular compounding technique based on path length encoding was presented to reduce presence of speckle in OCT images [39]. Speckle noise reduction in OCT images was recently achieved by use of angular compounding at multiple backscattering angles [9]. A recent study proves that the combination of experimental techniques (specifically angular compounding) and digital filter processing can result in over all superior image quality enhancement of OCT tomograms [41] . Speckle noise cannot be removed from standard OCT images using spatial and frequency compounding because the speckle pattern is uncorrelated at different positions, angles, and optical wavelengths [3].

The performance of the above mentioned digital algorithms varies depending on the type of image being used. An algorithm may perform superiorly for retinal tomograms while at the same time degrade in performance for skin OCT tomograms [3]. On the other hand, algorithm that performs well for skin OCT tomograms will degrade in performance for retinal tomogram [52]. The modifications to the existing OCT system means, more time spend on re-design and new components are needed.

An algorithm, that is robust, spatially adaptive, and one that can be applied to images obtained from different tissue type is investigated in this manuscript. The next few chapters will discuss two speckle reduction techniques based on the interval type II fuzzy sets. One algorithm utilizes the wavelet domain and soft thresholding [44]. The approach is a modification and improvement to previously published work [55] that uses type I fuzzy sets for additive Gaussian noise reduction. The other algorithm is based on anisotropic diffusion. The novelty of this algorithm is in the use of interval type II fuzzy sets to determine the uncertainty in the diffusion process and the appropriate adjustment of the diffusion coefficient parameter that can result in significant speckle noise reduction with minimum blurring of image features edges.

Chapter 4

Fuzzy logic

The two algorithms developed in this report utilize fuzzy logic. More specifically interval type II fuzzy sets. This chapter introduces the concept of fuzzy logic. Fuzzy set theory was first introduced by L. A. Zadeh in 1965 [68]. Fuzzy set deals with the imprecision and vagueness of human understanding systems. Using fuzzy sets, one can describe, analyze, and interpret the vague and uncertain events. During the transformation of 3D tissue sample into 2D world, numerous uncertainties arise. As a result, human knowledge in the form of fuzzy if-then-else rules can be applied to describe, analyze and interpret the OCT images. Fuzzy sets have been extensively used in computer vision and machine intelligence after being introduced by L. A. Zadeh [2].

4.1 Type I fuzzy set

In a binary image with intensity values 0 and 1, a pixel belongs to either an image feature (intensity of 1) or a background (intensity of 0). A pixel has a membership of 1 or 0 of belonging to the set "image feature" or to the set "background". However, on a gray scale OCT image of a tissue sample, each pixel has an ambiguous status with respect to the two sets. The gray scale OCT image will contain inherent ambiguities due to light dispersion on the physical surfaces. The neighbouring pixels may have very different intensity values and yet represent the same image feature of interest region. For normalized intensity values between 0 and 1, the image feature set can be defined by "all intensity values which are much greater than 0.5". Clearly, this does not constitute a set in the usual mathematical sense. Yet, this imprecisely defined set plays an important role in human thinking, particularly in the domain of image processing. This imprecisely defined set introduces the concept of a "fuzzy set".

A type I fuzzy set A in X is defined by a membership function (MF) $\mu_A(x)$ where $x \in \mathbf{X}$ and $\mu_A \subseteq [0, 1]$. X is a space containing objects with a specific element being denoted by x. The MF associates each objects in X a real number in the interval $[0, 1]$, with the value of $\mu_A(x)$ at x representing the "grade of membership" of x

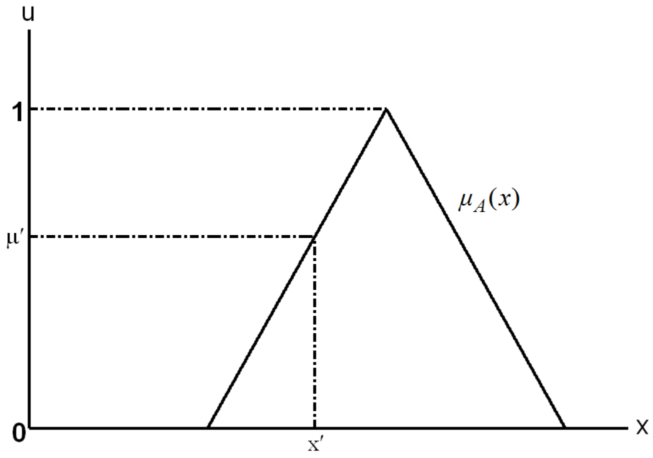

Figure 4.1: Membership function of a type I fuzzy set A. A specific value of $x^{'}$ has a membership degree of $\mu^{'}$.

in A. When the value of $\mu_A(x)$ is close to 1, x has higher grade of membership in A. When A is the set in the usual mathematical sense of the term, then $\mu_A(x)$ can take on only two values 0 and 1, with $\mu_A(x) = 1$ if x belongs to the set A or $\mu_A(x) = 0$ if x does not belong to the set A. This set is called the ordinary set, or crisp sets. As an example, Fig. 4.1 depicts the MF of type I fuzzy set A. The MF has a triangular shape and for $x = x^{'}$, it has a membership value of $u^{'}$.

Table 4.1: Triangular norms (T-norms) and triangular conorms (T-conorms)

T-Norm	
Minimum	$min(\mu_A(x), \mu_B(x))$
Algebraic Product	$\mu_A(x) \cdot \mu_B(x)$
Weak	$\begin{cases} min(\mu_A(x), \mu_B(x)) & \text{if } max(\mu_A(x), \mu_B(x)) = 1 \\ 0 & \text{otherwise.} \end{cases}$
Bounded Sum	$max(0, \mu_A(x) + \mu_B(x) - 1)$
T-Conorm	
Maximum	$max(\mu_A(x), \mu_B(x))$
Probabilistic Sum	$\mu_A(x) + \mu_B(x) - \mu_A(x) \cdot \mu_B(x)$
Strong	$\begin{cases} max(\mu_A(x), \mu_B(x)) & \text{if } min(\mu_A(x), \mu_B(x)) = 0 \\ 1 & \text{otherwise.} \end{cases}$
Bounded Sum	$min(1, \mu_A(x) + \mu_B(x))$

The logical operations of "complement (NOT)", "union (OR)", and "intersection (AND)" of ordinary sets can be extended to fuzzy sets for use in fuzzy logic and fuzzy reasoning. For fuzzy sets, these operations are expressed in terms of the MF of the sets which are operated on. For fuzzy set A in a universe X, $A^{'}$ is the complement (NOT) of A whose membership function is given by $\mu_{A'}(x) = 1 - \mu_A(x)$ for all $x \in \mathbf{X}$. Union of two fuzzy sets A and B in the same universe X is a fuzzy set containing all the elements from both sets, in a fuzzy sense. The membership function of the resulting set is given by $\mu_{A\cup B}(x) = max[\mu_A(x), \mu_B(x)]$ for all $x \in \mathbf{X}$. Similarly, the membership function of the intersection of two fuzzy sets A and B in the same universe X is given by $\mu_{A\cap B}(x) = min[\mu_A(x), \mu_B(x)]$ for all $x \in \mathbf{X}$. The "min" and "max" operations in the fuzzy set theory is called the "triangular norm" and "triangular conorms" respectively [25]. Table 4.1 lists some of the well-known triangular norms and triangular conorms from [55].

Image processing can be approached via fuzzy set theory. This form of image processing is called fuzzy image processing. Fuzzy image processing is defined as the collection of all approaches that understand, represent and process the images, their segments and features as fuzzy sets [61]. Fig. 4.2 shows the rule based type I fuzzy image processing. It has three main steps [36]: i) fuzzification ii) inference iii) output processing (defuzzification). Fuzzification takes the input gray scale image and generates data that can be processed with fuzzy techniques. In this step, the image data is transformed from gray level plane into a membership plane. The inference modifies the membership values using rule based fuzzy techniques. Deffuzifiation takes the membership plane data and converts it back to gray level plane. Fuzzy set theory is utilized in all three stages.

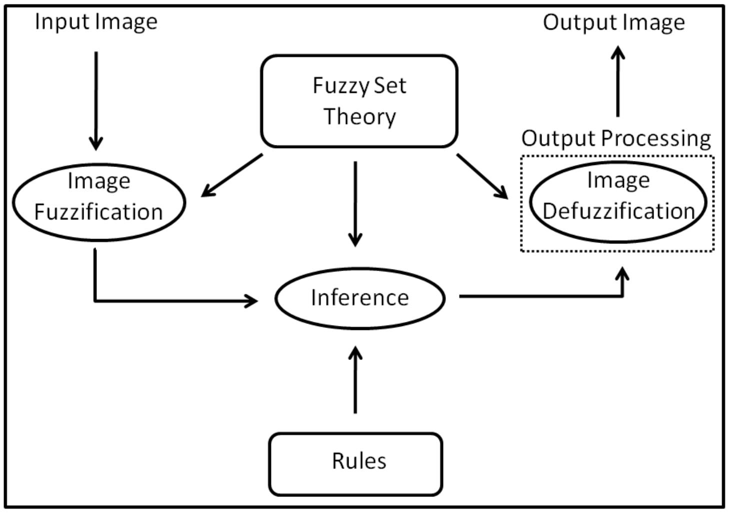

Figure 4.2: Type I fuzzy image processing.

4.2 Interval type II fuzzy set

In fuzzy set theory, the exact membership function for a fuzzy set is determined based on expert knowledge. This introduces ambiguity to type I fuzzy sets and leads to the formation of type II fuzzy sets. Type II fuzzy sets model and minimize the effects of uncertainties in rule-based type I fuzzy logic systems and it is useful when the exact membership function (MF) for type I fuzzy set cannot be determined [37].

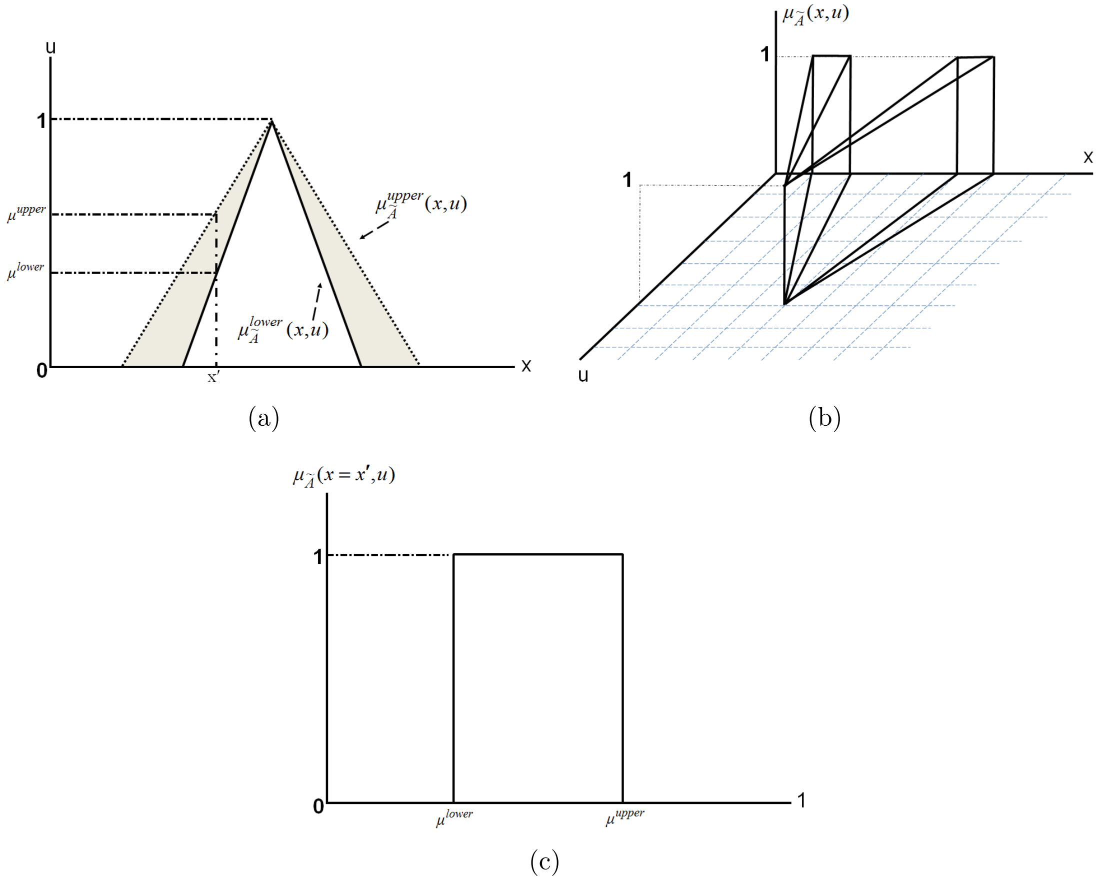

Figure 4.3: a) Blurred membership function of a type I fuzzy set A with shaded region representing the field of uncertainty. b) Three-dimensional membership function of an interval type II fuzzy set A with the third dimension all having a unit value. c) Example of a vertical slice for the interval type II membership function depicted in (a).

A type II fuzzy set $\widetilde{A}$ can be obtained from the type I fuzzy set A by shifting the MF of Fig. 4.1 to both the left and right [38]. Fig. 4.3(a) shows the results of this shift. The shaded region is called the footprint of uncertainty (FOU). So, for a specific value of x in type I fuzzy, type II fuzzy no longer has a single value for the membership function. Instead, the membership function takes on values wherever the vertical line intersects the FOU. These membership values need not all be weighted the same. Assigning weights to these membership values results in an amplitude distribution. When this is done for all $x \in \mathbf{X}$, a three-dimensional membership function, a type II membership function, that characterizes a type II fuzzy set is created [38].

A type II fuzzy set $\widetilde{A}$ is defined by a type II MF $\mu_{\widetilde{A}}(x,u)$ where $x \in \mathbf{X}$ and $u \in J_x \subseteq [0,1]$ [37]. When all $\mu_{\widetilde{A}}(x,u) = 1$ then type II is an interval type II fuzzy set. Fig. 4.3(b) depicts an interval type II 3D fuzzy membership function. In interval type II fuzzy set, the third dimension is no longer needed since it conveys no new information. Fig. 4.3(c) shows the vertical slice of the 3D interval type II membership function for a specific x value, I.e. $\mu_{\widetilde{A}}(x = \grave{x}, u)$. In an interval type II fuzzy system, the FOU can be represented easily using an upper and lower MFs as seen in Fig. 4.3(a). Thus, application of fuzzy logic for interval type II fuzzy sets is performed on the upper and lower membership functions.

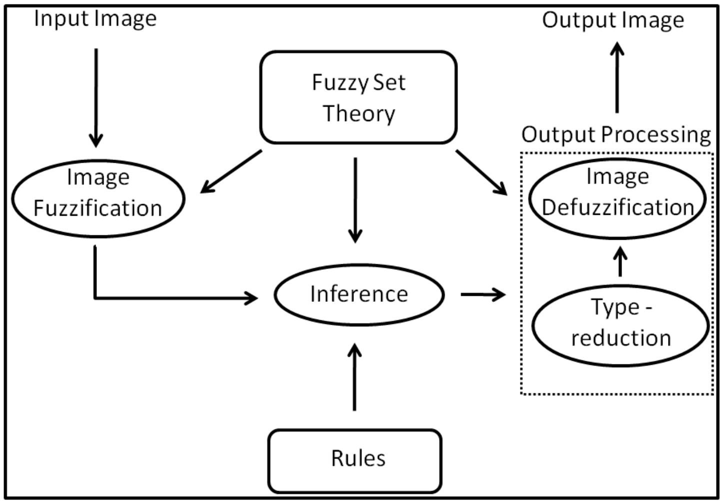

Figure 4.4: A flow chart describing the Type II fuzzy image processing.

Similar to the type I fuzzy image processing, a type II fuzzy system for image processing is depicted in Fig. 4.4. The only difference from the type I fuzzy image processing is the "'Type - reduction". The output from the Inference must be converted to a type I fuzzy sets before defuzzification can be applied.

Chapter 5

Interval type II fuzzy wavelet thresholding

In 1989, Mallat introduced a multi-resolution representation of an image that can be used to analysis the information content present in both coarse and fine details [35]. A wavelet transform is a multi-resolution decomposition tool, which allows an image to be represented at various resolutions or levels. By filtering and scaling the input image, the image space is divided into sequences of four lower resolution (or lower scale) components containing the approximation, horizontal, vertical, and diagonal detail coefficients represented by $W_{\varphi}(j,m,n)$, $W_{\psi}^{H}(j,m,n)$, $W_{\psi}^{V}(j,m,n)$, and $W_{\psi}^{D}(j,m,n)$ respectively. The variable j represents the decomposition scale level and represents the image spatial location. The crucial image information is compressed and represented along several resolution scales by few of these large valued coefficients [47]. Thus, by analyzing images at various resolutions, one can remove the unwanted noise, represented by the low valued coefficients.

In image processing, the application of a wavelet based de-noising method consists of the following three steps: i) computing the two-dimensional discrete wavelet transform (2D-DWT) of the image at various levels of decomposition ii) removing noise from the detail wavelet coefficients (W_{ψ}^{H}, W_{ψ}^{V}, and W_{ψ}^{D}) by soft thresholding iii) finally, reconstructing the enhanced image using inverse 2D-DWT. For an image, Mallat's 2D-DWT can be implemented using 4 frequency channel filter banks corresponding to the four orientations. The wavelet transform of natural images has special properties like inter-scale and intra-scale dependencies and as a result de-noising using wavelet transform has proven to be very effective. Inter-scale dependency refers to large wavelet coefficients propagating across the scales and intra-scale dependency refers to neighbourhood of similar valued coefficients (large or small) at each scale.

$$f_{j,d}(m,n) = s_{j,d}(m,n) + n_{j,d}(m,n) \tag{5.1}$$

Applying the 2D-DWT to the log transformed OCT image results in Eqn. 5.1. In Eqn. 5.1, $f_{j,d}$ denotes the noisy wavelet coefficient of the observed image at scale j and at orientation d, $s_{j,d}$ is the noise-free wavelet coefficient of the image and $n_{j,d}$ represents the wavelet coefficient of the speckle noise. Additive noise in the image domain remains additive in the transformed wavelet domain due to the linearity of the wavelet transform. The next step in the wavelet based denoising algorithm is thresholding the detail wavelet coefficients, $f_{j,d}(m, n)$ where $d \in \{H, V, D\}$, by use of a soft threshold. In soft thresholding if the magnitudes of the coefficients are below the threshold then they are set to zero while the coefficients with the magnitudes above the threshold are scaled towards zero. This is because the coefficients that contain mostly noise should be reduced to negligible values, while the ones containing a substantial noise free component should be reduced less. In wavelet domain different types of noise are associated with small magnitude coefficients. Important image structures are contained within the magnitude of the high coefficients. The coefficients around the threshold contain both noise and image features of interest. Therefore, an optimal threshold is reached when most of the coefficients below it are noise and the coefficients above it represent image features of interest.

Due to the ambiguity in choosing a suitable threshold fuzzy set theory can be applied. Using fuzzy set theory, more specifically, using fuzzy rule-based approach, the wavelet thresholding can be expressed as a fuzzy wavelet thresholding. The fuzzy wavelet thresholding procedure is divided into four main steps which are discussed in detail below.

5.1 Step 1: Image features

The first step in fuzzy based image processing is to establish the image features, each corresponding to linguistic labels. Each feature is then fuzzified by their appropriate membership function. Linguistic label is a verbal scale of qualitative linguistic estimates [5], for expressing one's own subjective judgments about both the support and the negation of a proposition [5]. For example, "likely in very high degree" and "unlikely in high degree" are two examples of linguistic labels that can be used to describe the proposition "Is that person tall?" These linguistic labels help to translate human reasoning to digital operations. These labels are represented by fuzzy sets in fuzzy set theory.

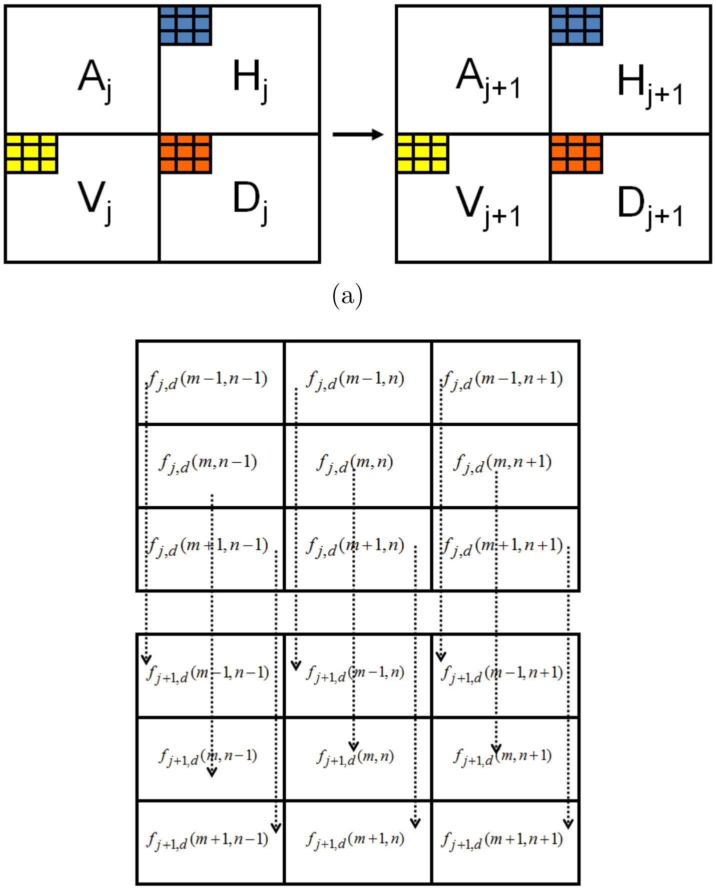

(a)

(b)

Figure 5.1: Two-dimensional wavelet decomposition at level j and $j+1$. The intra-scale and inter-scale relationship among the horizontal (H), vertical (V) and diagonal (D) detail coefficients is shown

As described in chapter 4, the membership function is a mathematical function that specifies the degree to which a given input belongs to the set defined by the linguistic labels. The output of the membership function is between 0 and 1. In this manuscript, two fuzzy variables are defined and the following describes it.

At position (m, n), if the wavelet coefficient has a magnitude that is large, then the coefficient at (m, n) represents image feature of interest for "almost certain" and should not be set to zero but scaled towards zero. The reason for this statement is due to the property of image edges appearing as large magnitude wavelet coefficients due to the rapid changes in intensity values. Large image structures can be found in many scales of the wavelet decomposition, but small image details can only be revealed in several fine scales and to determine small image details, inter-scale correlation involving two adjacent scales can be used [29]. A hierarchical correlation map that considers both the correlation between neighbouring coefficients (intra-scale) and correlation between two adjacent levels (inter-scale) can be obtained to determine fine image features. Fig. 5.1 shows the intra-scale and inter-scale relationship among the wavelet coefficients. In the correlation map that is generated, large values indicate position of edges in the original image, and zero coefficients correspond to smooth areas which are noise regions [29]. This leads to the following statement: at position (m, n), if the correlation map value is large, then the coefficient at (m, n) represents fine image structures of interest for "almost certain" and should not be set to zero but scaled towards zero. Conversely, a correlation value close to zero indicates an area which needs to be smoothed due to noise.

Using the linguistic labels, large magnitude wavelet coefficient at position (m, n) and large correlation map value at position (m, n), two fuzzy variables can be defined as follows:

Large magnitude wavelet coefficient (Eqn. 5.2):

$$w_{j,d}(m, n) = |f_{j,d}(m, n)| \tag{5.2}$$

Large correlation map value modified from reference [29] to account for the undecimated 2D wavelet transform (Eqn. 5.3, 5.4, and 5.5):

$$x_{j,d}(m, n) = \sqrt{inter_{j,d}(m, n) \cdot intra_{j,d}(m, n)} \tag{5.3}$$

$$inter_{j,d}(m, n) = \sqrt{\sum_{a=-N}^{a=N} \sum_{b=-N}^{b=N} |f_{j,d}(m + a, n + b) \cdot f_{j+1,d}(m + a, n + b)|} \tag{5.4}$$

$$intra_{j,d}(m, n) = \sqrt{\prod_{a=-N}^{a=N} \prod_{b=-N}^{b=N} |f_{j,d}(m + a, n + b)|} \tag{5.5}$$

Fine image structures which do not appear as local maxima will now be revealed in the correlation map [29]. Due to oriented edges being visible in certain subbands, subands of different orientations should be treated separately. As a result, the correlation map is found for the horizontal, vertical, and diagonal subbands separately, i.e. $d \in \{H, V, D\}$. The correlation map value $x_{j,d}(m, n)$ at decomposition level j and orientation d is based on nine wavelet coefficients in a 3x3 window ($N = 1$) at level j and orientation d, and the nine coefficients in the next level $j + 1$ and orientation d. The subbands in each of the wavelet levels have the same size due to the Stationary Wavelet Transform (SWT). As a result, the coefficients have one-to-one correspondence in terms of the position (m, n).

Now, two corresponding tnterval type II fuzzy sets (IT2FS) can be assigned to these fuzzy variables. Type II fuzzy set A corresponds to the large magnitude

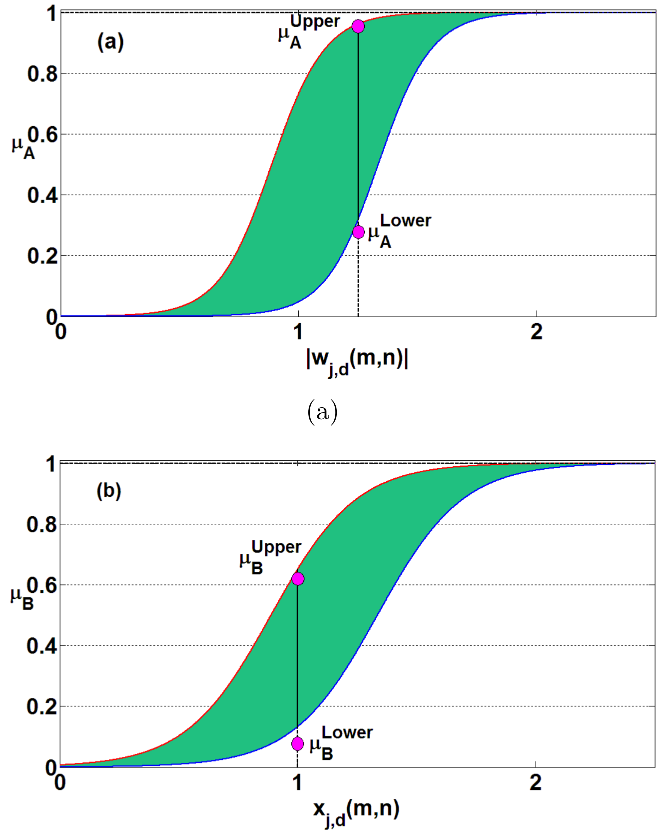

(a)

(b)

Figure 5.2: Interval type II fuzzy membership functions for the fuzzy variables a) “large magnitude wavelet coefficient” and b) “large correlation map value”.

wavelet coefficient and type II fuzzy set B corresponds to the large correlation map value. The corresponding type II sigmoid membership functions are presented in Fig. 5.2. The shaded regions in the figures correspond to the areas where the uncertainty lies in determining if the coefficient is noisy or not. In Fig. 5.2, the fuzzy membership values are near one when the magnitude of the wavelet coefficient is large and when the correlation map value is also large. Similarly, if the magnitude of the wavelet coefficient or correlation map value is small or near zero, then the fuzzy membership value is near zero. However, if the magnitude of the wavelet coefficient and the correlation map value are neither large nor small, then the fuzzy membership value takes on a range of values. The range of values are indicated on Fig. 5.2 by the vertical line intersecting the upper and lower membership functions. These range of values are defined by the upper and lower membership values (μ_A^{Upper}, μ_B^{Upper}, μ_A^{Lower}, and μ_B^{Lower}) and it incorporates the uncertainty involved in deciding if the magnitude of the wavelet coefficient and the correlation map value near the threshold is indicating if noise is present at that location. The membership values represent the degree by which a wavelet coefficient represents an image feature of interest. High membership value corresponds to high degree that the wavelet coefficient belongs to an image feature of interest. Likewise, a low membership value corresponds to a low degree that the wavelet coefficient belongs to an image feature of interest.

The general equation for a sigmoid membership function is given in Eqn. 5.6 and it has two parameters associated with it, its center (c) and its width (w).

$$\mu(x) = \frac{1}{1 + e^{\frac{c-x}{w}}} \tag{5.6}$$

The upper and lower MFs are determined based on Eqn. 5.7 and Eqn. 5.8.

$$\mu_A^{Upper} = [\mu_A(x)]^{\frac{1}{\beta_A}} \text{ and } \mu_A^{Lower} = [\mu_A(x)]^{\beta_A} \tag{5.7}$$

$$\mu_B^{Upper} = [\mu_B(x)]^{\frac{1}{\beta_B}} \text{ and } \mu_B^{Lower} = [\mu_B(x)]^{\beta_B} \tag{5.8}$$

In Eqn. 5.7 and Eqn. 5.8, there are various parameters involved. First of all, β parameter controls the width of the footprint of uncertainty in the interval type II fuzzy set A and B. A β value of 1 reduces the interval type II fuzzy set to a type I fuzzy set. According to Tizhoosh [62], β should be between 1 and 2 and $\beta \gg 2$ is usually not meaningful for image data. The center, c, of the membership functions control the location of the footprint of uncertainty while the width, w of the membership functions controls the shape of the footprint of uncertainty. It is important to note that the center, c, and the width, w, associated with the membership functions for fuzzy set A and B does not have to be the same. By adjusting these parameters, the amount of speckle noise removed can be varied. Thus, allowing for more or less smoothing depending on the input image being used and the amount of speckle present.

5.2 Step 2: Knowledge-base

After image data is transformed from input plane to the membership plane, fuzzy rule-based approach is applied to modify the membership values. The next step in fuzzy wavelet thresholding is to set up a knowledge-base that is composed of fuzzy if-then rules. Utilizing the fuzzy variables from the previous section that represents the image features the following fuzzy rule is obtained:

Rule 1: If the magnitude of the wavelet coefficient at (m, n) is “large” AND the correlation map value at (m, n) is “large” then “scale towards zero the wavelet coefficient at (m, n)”.

General wavelet based thresholding can be achieved by either a hard thresholding or by a soft thresholding [20]. Hard thresholding corresponds to setting to zero the wavelet coefficients when its absolute values are below a threshold. On the other hand, soft thresholding corresponds to first setting to zero the coefficients whose absolute values are lower than the threshold. Then, the non-zero coefficients are scaled towards zero. Soft-thresholding eliminates the discontinuity (at the threshold) that is inherent in hard thresholding [20]. Thus, in the fuzzy wavelet thresholding, the soft thresholding technique is achieved by the membership functions. The membership values, essentially represents the scaling factor. When membership value is 0, then it corresponds to setting the wavelet coefficients to zero and a non zero membership value corresponds to the wavelet coefficient being scaled towards zero. By adding new fuzzy rules, the algorithm can be changed effortlessly to include other information from the image to further improve speckle reduction performance.

5.3 Step 3: Rule strength

For the fuzzy rule, the fuzzified inputs are combined and a rule strength is obtained. This rule strength is used as the consequence of the rule. The strength of rule 1 is computed via the algebraic product triangular norm (see table 4.1) and is given by the following:

$$\alpha_{j,d}^{Upper}(m,n) = \mu_A^{Upper}(|w_{j,d}(m,n)|) \cdot \mu_B^{Upper}(x_{j,d}(m,n)) \tag{5.9}$$

$$\alpha_{j,d}^{Lower}(m,n) = \mu_A^{Lower}(|w_{j,d}(m,n)|) \cdot \mu_B^{Lower}(x_{j,d}(m,n)) \tag{5.10}$$

Since, interval type II fuzzy set is being used; there are two consequences for the rules each corresponding to the upper and lower limit. This consequence represents the degree by which the wavelet coefficient should be scaled. Once the consequences from various rules have been obtained, in general they are combined to obtain an output distribution range. Since, in this manuscript only one fuzzy rule is being used, there is no need for combining fuzzy rules. In general, the probabilistic sum triangular conorm (see table 4.1) is used to combine various rules.

5.4 Step 4: Scaling factor

Finally, a value representing the scaling factor for the wavelet coefficient at (m,n) is obtained by type reducing and defuzzifying the output from step 3. There is more than one approach to defuzzifying the output distribution; here the average of the upper and lower value is utilized.

$$\gamma_{j,d}(m,n) = \frac{\alpha_{j,d}^{Upper}(m,n) + \alpha_{j,d}^{Lower}(m,n)}{2} \tag{5.11}$$

Now, a new coefficient can be obtained at position (m, n) which has been reduced of noise. This is obtained by applying Eqn. 5.12. The filtering is performed at each scale of the wavelet domain and for each of the three detail coefficients $(d \in \{H, V, D\})$.

$$\widehat{f}_{j,d}(m,n) = f_{j,d}(m,n) \cdot \gamma_{j,d}(m,n) \tag{5.12}$$

Once, all the coefficients have been found, applying the inverse two-dimensional discrete wavelet transform to the processed data will result in a de-noised final image.

5.5 Proposed Algorithm

The following summarizes the interval type II based fuzzy wavelet thresholding algorithm.

1. Add BIAS to the OCT image and take the logarithmic transform of the speckled image. (BIAS prevents $log(0)$).
2. Apply the two-dimensional discrete wavelet transform to the log transformed image.
3. For each detail coefficients (horizontal, vertical and diagonal) at each subband levels $(1, 2, 3...N)$ with N levels of decomposition.
    - apply Eqn. 5.12, the interval type II fuzzy shrinkage method to the coefficients of the corresponding subband.
4. Apply the inverse two-dimensional discrete wavelet transform to reconstruct the denoised image.
5. Take the exponent of the reconstructed image and subtract the BIAS that was added initially to obtain the final image.

The implementation of the interval type II fuzzy wavelet thresholding filter involved many parameters. The orthogonal Daubechies wavelet, more specifically "db4", was utilized for the 2D-DWT with four levels of decomposition. Fourth-order Daubechies wavelet brings smoothing effects due to the longer filter lags [51] and this reduces the pixilation effect seen when lower-order Daubechies wavelet is utilized. The 2D-DWT was implemented using an undecimated filter bank and this formulation is known as the stationary wavelet transform (SWT) [19]. Although SWT requires excessive computer memory and longer CPU run-time, it is able to denoise and detect edges better [19]. Mallat's 2D-DWT is not used in this manuscript. Although, Mallat's 2D-DWT runs at half the speed of SWT but the implementation uses the decimated filter bank, which is prone to Gibbs artefacts caused by sharp edges in the image [3]. The digital implementation of SWT algorithm was done using the Fast Wavelet Transform (FWT) technique outlined in [20]. The image is convolved with the “db4” decomposition low-pass and high-pass filters in various sequences. The next scale of the image in the wavelet transform is obtained by up sampling the low-pass and high-pass filters by a factor of two. As mentioned earlier in the manuscript, the four frequency channel filter banks for the 2D-DWT are the four sequences of convolution involving decomposition “db4” low-pass and high-pass filters (low-low, low-high, high-high, and high-low). The Matlab *conv*2() function was utilized for the convolution. Similarly, the image is reconstructed by up sampling the low scale images and convolving it with the “db4” low-pass and high-pass reconstruction filters. The experimental results from applying the above algorithm on OCT images are discussed in chapter 7.

Chapter 6

Interval type II fuzzy anisotropic diffusion

Consider the diffusion of heat throughout a material. Heat diffuses over time and its time dynamics can be modelled by the partial differential "heat equation" given in Eqn. 6.1.

$$\frac{\partial u(x,y,t)}{\partial t} = c(t)\Delta u(x,y,t) \tag{6.1}$$

In Eqn. 6.1, Δ represents the Laplace operator and $c(t)$ is the "diffusion rate constant" or the "diffusion coefficient" which is spatially invariant. When the origin of heat is a single spike in time and space, the solution to Eqn. 6.1 is a time progression of Gaussian functions, with progressively larger σ as time goes on. An example of this spread in one dimension is depicted in Fig. 6.1.

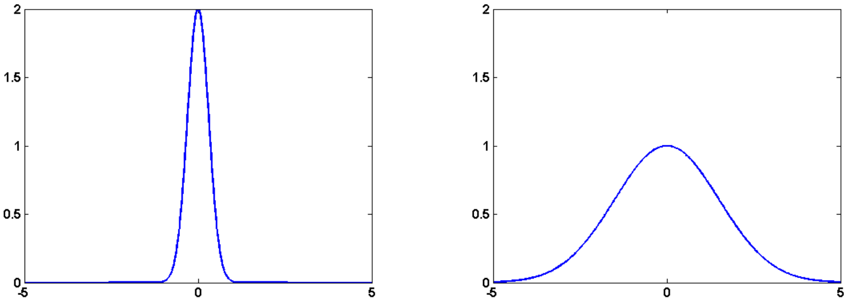

(a) At time $t = 0$ (b) At time $t = t_N$

Figure 6.1: 1D Heat diffusion over time

Therefore, any heat distribution can be represented as a combination of heat spikes. Since the differential operators are linear, the evolution of the heat distribution with time can be represented as a superposition of a group of spreading Gaussian functions.

The spreading of a Gaussian function is equivalent to convolving it with a Gaussian kernel, which in image processing can describe a blurring or smoothing process. Now, consider an image as a function indicating the temperature distribution in two-dimensional space. One way to blur the image is to let it evolve using the heat equation. Koenderink has shown that computing the convolution of an image with a Gaussian kernel is in fact equivalent to the solution of the standard heat conduction equation [27]. Therefore, we can consider that in Eqn. 6.1, u is the $2D$ image and Δ represents the Laplace Operator performed on the image. The diffusion process described so far is isotropic. One drawback of using isotropic diffusion for image processing is that although it filters out noise, it also blurs the edges of the image, which reduces the image sharpness. The image blur can be minimized by varying the rate of diffusion in space so that diffusion is slower near the edges. Mathematically, anisotropic diffusion can be described with a spatially varying diffusion coefficient $c(x, y, t)$.

6.1 Anisotropic diffusion

Anisotropic Diffusion is a mutli-scale smoothing and edge enhancement image processing technique that has been proposed by Perona and Malik [42]. The idea behind anisotropic diffusion is to let the diffusion rate constant, $c(t)$ be a function of image space as given in Eqn. 6.2.

$$c(x, y, t) = \begin{cases} \text{large in homogeneous region} \\ \text{small near image edges} \end{cases} \tag{6.2}$$

By making the diffusion coefficient small near edges, the smoothing of edge regions can be avoided. If blurring takes place separately in each image region with no interaction between regions, the region boundaries will remain sharp. Such approach can enhance the image region corrupted by speckle noise. Any edges in an image can be found using the gradient of the image. Thus, to construct a spatially varying diffusion constant $c(x, y, t)$, the magnitude of the image gradient can be utilized. The gradient can be computed using the first difference. However, in this manuscript, Prewitt Operator defined by the convolution kernels given in Eqn. 6.3 is used to obtain the image gradients. The Prewitt operator is less sensitive to noise than the first difference operators.

$$\nabla_x = \begin{pmatrix} -1 & 0 & 1 \\ -1 & 0 & 1 \\ -1 & 0 & 1 \end{pmatrix} \text{ and } \nabla_y = \begin{pmatrix} 1 & 1 & 1 \\ 0 & 0 & 0 \\ -1 & -1 & -1 \end{pmatrix} \tag{6.3}$$

To achieve a more stable performance, Catte et.al [7] proposed to calculate the gradient of the image after the image has been smoothed, i.e., calculate the gradient on the image after it has been convolved with a Gaussian kernel. This way, the noise does not significantly affect the calculation of the image gradient. Also, according to [57], post-edge detection process also helps to enhance the edges. A Gaussian and a median filter were applied to the edges obtained after the Prewitt operator to obtain edges with fine neighbourhoods. The new edge based anisotropic diffusion coefficient is given by Eqn. 6.4.

$$c(x,y,t) = g\Big(G_\sigma * med\Big\langle \sqrt{\mid \nabla_x * (G_\sigma * I) \mid^2 + \mid \nabla_y * (G_\sigma * I) \mid^2} \Big\rangle\Big) \tag{6.4}$$

In Eqn. 6.4, $*$ denotes the convolution operator, G_σ is the Gaussian kernel, and $med\langle\rangle$ is the median filter. When the argument of the function $g(\cdot)$ is small (for homogeneous regions), the diffusion coefficient, $c(x,y,t)$ is large and conversely when the argument of the function is large (at or near edges), the diffusion coefficient is small, which corresponds to slower diffusion rates. The diffusion coefficient is a function of the image space. An example diffusion function proposed by Perona et.al. [42] and modified by Lin, et.al. [31] is presented in Eqn. 6.5. This is the function utilized in this manuscript for the anisotropic diffusion. The function $g(x)$ in Eqn. 6.5 is plotted in Fig. 6.2.

$$g(x) = \frac{1}{1 + \frac{x}{K^2}} \tag{6.5}$$

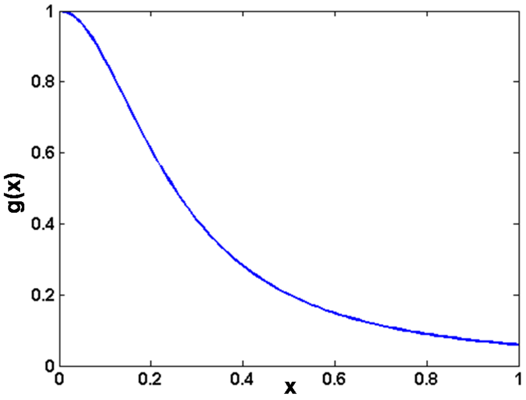

Figure 6.2: Diffusion function

When applied to speckled images, the function $g(x)$ results in blurring of small discontinuities and sharpening of edges. The parameter K in Eqn. 6.5 is chosen according to the speckle noise level and the edge strength. The noise level is not known apriori with certainty. Furthermore, because of inherent speckle noise, the calculated edge strength based on gradient is not a true reflection of the edge strength. In anisotropic diffusion, ambiguity in the diffusion coefficient results due to the ambiguity of choosing a suitable value for the parameter K and the ambiguity in the edge strength. This justifies the use of the fuzzy set theory for anisotropic diffusion.

6.2 Interval type II fuzzy anisotropic diffusion

Fuzzy set theory is a soft computing technique that deals with the imprecision and vagueness of human understanding systems. It is able to directly model and minimize the effect of uncertainty in the chosen parameters of anisotropic diffusion. By using fuzzy set theory, more specifically, by using fuzzy rule-based approach the anisotropic diffusion algorithm can be expressed as a fuzzy anisotropic diffusion algorithm. In the past, the Type I fuzzy anisotropic diffusion was applied for speckle noise reduction by a number of research groups for images acquired with imaging modalities different than OCT [57, 4]. Also, Song et.al [57] and Aja et. al. [4] utilized Type I fuzzy with more rule sets than necessary while Sanchez-Ortiz [50] used a fuzzy clustering approach to enhance cardiac MR images. By applying interval type II fuzzy set, all the rules presented in references [57] and [4] can be reduced to a single rule. The uncertainty in reducing the number of rule sets in type I fuzzy is incorporated into the type II fuzzy set. The interval type II fuzzy anisotropic diffusion procedure is divided into four main steps which are discussed in detail below.

6.2.1 Step 1: Image features

The first step in interval type II fuzzy based anisotropic diffusion is to establish the image features, each corresponding to linguistic labels. Then, using the appropriate membership functions, each feature is fuzzified. As mentioned before, the diffusion coefficient $c(x, y, t)$ must be such that, it is greatest near homogenous regions and lowest at edge regions. But, it must also be greatest near noisy regions to filter the noise. Therefore, at time t, in the image location (x, y), if the edge value is low and noise level is high then this pixel must be smoothed definitely and thus the diffusion coefficient should be set to high. From this statement two linguistic variables can be identified; edge value at pixel location (x, y) and noise level at pixel location (x, y). Using these linguistic labels, two fuzzy variables are defined as follows:

$$E(x, y, t) = G_\sigma * med\left\langle \sqrt{\mid \nabla_x * (G_\sigma * I) \mid^2 + \mid \nabla_y * (G_\sigma * I) \mid^2} \right\rangle \tag{6.6}$$

$$N(x, y, t) = \left| I(x, y, t) - \frac{1}{(2L+1)^2 - 1} \sum_{i=-L}^{i=L} \sum_{j=-L}^{j=L} I(x+i, y+j, t) \right| \tag{6.7}$$

Eqn. 6.6 represents the edginess measure. Eqn. 6.7 represents the noisiness measure according to reference [57]. Edginess measure $E(x, y, t)$ is based on median filtering the gradient of smoothed version of the image $I(x, y)$ at time t as defined before in Eqn. 6.4. Song et.al. [57], used the standard deviation as a noisiness measure for each image pixel, which was calculated as the absolute difference between the pixel intensity and the local mean of its neighbourhood. In this report, similar noisiness measure $N(x, y, t)$ is implemented. A $7x7$ window was used to calculate the local mean of the image (i.e. $L = 3$). It is important to note that high noisiness measure at (x, y) corresponds to high noise level at (x, y). Both edginess and noisiness measures were normalized to be between 0 and 1.

Two corresponding interval type II fuzzy sets can be assigned to these fuzzy variables. Type II fuzzy set A corresponds to the low edginess measure and type II fuzzy set B corresponds to high noisiness measure (i.e. high noise level). Eqn. 6.8 and 6.9 represents the corresponding type II membership functions and Fig. 6.3 shows an example of such functions. The shapes of the membership functions defined by Eqn. 6.8 and 6.9 are obtained from Eqn. 6.5. That is, $g_A(x) = g(x)$ for $K = K_A$ and $g_B(x) = g(1 - x)$ for $K = K_B$.

$$\mu_A^{Upper} = g_A(x)^{\frac{1}{\beta_A}} \text{ and } \mu_A^{Lower} = g_A(x)^{\beta_A} \tag{6.8}$$

$$\mu_B^{Upper} = g_B(x)^{\frac{1}{\beta_B}} \text{ and } \mu_B^{Lower} = g_B(x)^{\beta_B} \tag{6.9}$$

In Eqn. 6.8 and 6.9, there are various parameters involved. First of all, β parameter controls the width of the footprint of uncertainty in the interval type-II fuzzy set A and B. As mentioned in the previous chapter, a β value of 1 reduces the interval type-II fuzzy set to a type-I fuzzy set. β should be between 1 and 2 and $\beta \gg 2$ is usually not meaningful for image data [62]. The parameter K controls the shapes of the membership functions of fuzzy set A and B. It is important to note that the parameter K, associated with the membership functions for fuzzy set A and B does not have to be the same. By adjusting these parameters, the amount of speckle noise removed can be varied. Thus, allowing for more or less smoothing depending on the input image being used and the amount of speckle present.

The shaded regions in Fig. 6.3 correspond to the areas where the uncertainty lies in determining the diffusion coefficient $c(x, y, t)$. In Fig. 6.3(a) if the value of $E(x, y, t)$ is low corresponding to low edge values, the fuzzy membership value is near one. Consequently, if the value of $E(x, y, t)$ is large, then the fuzzy membership value is near zero. However, if the value of $E(x, y, t)$ is neither large nor small, then the fuzzy membership value takes on a range of values defined by the upper and lower membership values μ_A^{Upper} and μ_A^{Lower}. Similarly, in Fig. 6.3(b) if the value of $N(x, y, t)$ is high corresponding to high noise level, the fuzzy membership value is near one. Consequently, if the value of $N(x, y, t)$ is low, then the fuzzy membership value is near zero. If the value of $N(x, y, t)$ is neither high nor low, then the fuzzy membership value takes on the range of values defined by the upper and lower

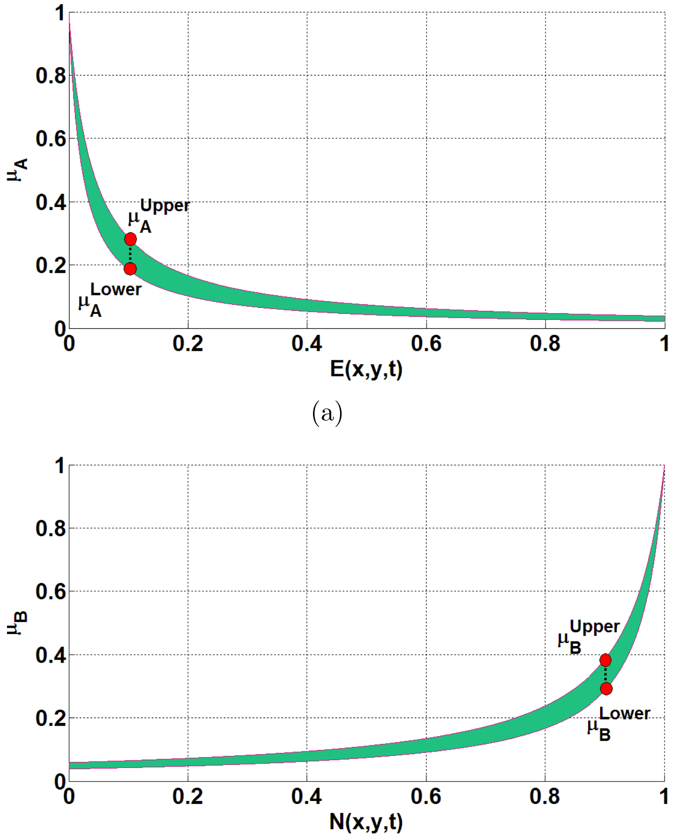

(a)

(b)

Figure 6.3: Interval Type II Fuzzy Membership functions for the fuzzy variables a) "low edginess measure" and b) "high noisiness measure".

membership values μ_B^{Upper} and μ_B^{Lower}. An example of the range of values defined by the upper and lower membership values is depicted for both fuzzy sets in Fig. 6.3. The uncertainty in choosing a value for the parameter K in the anisotropic diffusion function (Eqn. 6.5) lies in this region. The membership values represent the degree by which the pixel value located at (x, y) needs to be smoothed. High membership value corresponds to high degree of smoothing. Likewise, a low membership value corresponds to low degree of smoothing.

6.2.2 Step 2: Knowledge-base

After image data is transformed from input plane to the membership plane, fuzzy rule-based approach is applied to modify the membership values. The next step in interval type II fuzzy anisotropic diffusion is to set up a knowledge-base that is composed of fuzzy **if-then** rules. Utilizing the fuzzy variables from the previous section that represents the image features the following fuzzy rule is obtained:

Rule 1: If edginess measure ($E(x, y, t)$) is a low value AND noisiness measure

$(N(x, y, t))$ is a high value THEN the diffusion coefficient $c(x, y, t)$ is a high value.

The reason behind the rule is quite simple. When there is an edge, then do not smooth. However, when there is no edge and it is noisy, then perform strong smoothing. In summary, with increasing degree of noisiness the coefficient increases and with decreasing degree of edginess the coefficient decreases. In this way, edges will not be smoothed and will remain sharp while the interior homogenous regions will be smoothed. It is important to remember that higher diffusion coefficient at (x, y) is required when edge value is low and noise level is high.

6.2.3 Step 3: Rule strength

For the previous mentioned fuzzy rule, the fuzzified inputs are combined and rule strength is obtained. This rule strength is used as the consequence of the rule. Applying the algebraic product triangular norm (see table 4.1) to "$E(x, y, t)$ is a low value AND $N(x, y, t)$ is a high value," the following truth value is obtained:

$$\gamma^{Upper}(x, y, t) = \mu_A^{Upper}(E(x, y, t)) \cdot \mu_B^{Upper}(N(x, y, t)) \tag{6.10}$$

$$\gamma^{Lower}(x, y, t) = \mu_A^{Lower}(E(x, y, t)) \cdot \mu_B^{Lower}(N(x, y, t)) \tag{6.11}$$

There are two consequences for the rule each corresponding to the upper and lower limit. This consequence represents the degree by which the pixel value at (x, y) should be smoothed. More specifically, Eqn. 6.10 and 6.11 represent the degree of activation of Rule 1 at the pixel location (x, y) at time t. This range of values $(\gamma^{Upper}(x, y, t), \gamma^{Lower}(x, y, t))$ indicates the degree of membership in the fuzzy set "diffusion coefficient $c(x, y, t)$ is a high value". If the range of values are close to 1, this means that the diffusion coefficient is also close to 1 indicating maximum smoothing, while a degree value close to 0 indicates that the diffusion coefficient is close to 0 indicating no smoothing.

6.2.4 Step 4: Diffusion coefficient

Finally, a single value representing the diffusion coefficient is obtained by type reducing and defuzzifying the output from step 3. Eqn. 6.10 and 6.11 represent the index of ultrafuzziness, which is an interval. In order to use the ultrafuzziness in the interval type II fuzzy anisotropic diffusion algorithm it must be transformed to an index of fuzziness (type reduced). By using the average of the upper and the lower fuzziness values, the ultrafuzziness can be converted to index of fuzziness. Thus, the new diffusion coefficient for interval type II fuzzy anisotropic diffusion is represented by Eqn. 6.12.

$$c(x, y, t) = \frac{\gamma^{Upper}(x, y, t) + \gamma^{Lower}(x, y, t)}{2} \tag{6.12}$$

6.3 Proposed Algorithm

This section details the digital implementation of the anisotropic diffusion algorithm. As seen in Eqn. 6.1, the digital implementation starts with the partial differential Eqn. [16]:

$$\begin{aligned}
\frac{\partial I(x,y,t)}{\partial t} &= c(x,y,t)\Delta I(x,y,t) \qquad (6.13)\\
&= c(x,y,t)\nabla \cdot \nabla I(x,y,t)\\
&= \nabla[c(x,y,t)\nabla I(x,y,t)]\\
&= div[c(x,y,t)\nabla I(x,y,t)]\\
&= \frac{\partial}{\partial x}[c(x,y,t)\frac{\partial}{\partial x}I(x,y,t)]\\
&+ \frac{\partial}{\partial y}[c(x,y,t)\frac{\partial}{\partial y}I(x,y,t)]
\end{aligned}$$

In Eqn. 6.13, *div* denotes the divergence operator and ∇ denotes the gradient of the image. The diffusion coefficient, $c(x,y,t)$ in conjunction with the image gradient describe the diffusion flow between the image pixels, i.e. $c(x,y,t)\nabla I(x,y,t)$. Applying central differencing for $\frac{\partial}{\partial x}$ and $\frac{\partial}{\partial y}$ results in the following [16],[4]:

$$\begin{aligned}
\frac{\partial I(x,y,t)}{\partial t} &= \Phi_E - \Phi_W + \Phi_N - \Phi_S \qquad (6.14)\\
\Phi_E &= \frac{1}{\Delta x^2}\Big[C_E(x,y,t) * (I(x+\Delta x,y,t) - I(x,y,t))\Big]\\
\Phi_W &= \frac{1}{\Delta x^2}\Big[C_W(x,y,t) * (I(x,y,t) - I(x-\Delta x,y,t))\Big]\\
\Phi_N &= \frac{1}{\Delta y^2}\Big[C_N(x,y,t) * (I(x,y+\Delta y,t) - I(x,y,t))\Big]\\
\Phi_S &= \frac{1}{\Delta y^2}\Big[C_S(x,y,t) * (I(x,y,t) - I(x,y-\Delta y,t))\Big]
\end{aligned}$$

For the anisotropic diffusion represented by Eqn. 6.14, the local flow is a function of the diffusion coefficient for every direction and the difference between the central pixel and each of the 4-connected pixels in every orientation. C_N, C_S, C_E, and C_W are the diffusion coefficients for each orientation Up, Down, Left, and Right respectively. Now, approximating $\frac{\partial I(x,y,t)}{\partial t}$ as $\frac{I(x,y,t+\Delta t)-I(x,y,t)}{\Delta t}$. The final equation representing the anisotropic diffusion is the following:

$$
\begin{aligned}
\frac{I(x,y,t+\Delta t)-I(x,y,t)}{\Delta t} &\approx \frac{\partial I(x,y,t)}{\partial t} \\
I(x,y,t+\Delta t) &\approx I(x,y,t)+\Delta t\frac{\partial I(x,y,t)}{\partial t} \\
&\approx I(x,y,t)+\Delta t(\Phi_E-\Phi_W+\Phi_N-\Phi_S)
\end{aligned} \tag{6.15}
$$

Eqn. 6.15 describes the iterative process of the anisotropic diffusion. At each new time step $t+\Delta t$ a new image is obtained from the previous image at time step t. $I(x,y)$ at a time $t+\Delta t$. A particular note about the time variable t in the anisotropic diffusion algorithm is that, in the 2D discrete implementation, this variable represents the iteration number, n. Δt is an integration constant and it determines the iterative approximation stability of Eqn. 6.15 [16]. Perona et. al [42] defines a range for Δt, $\Delta t \in (0, 0.25]$, for stability of Eqn. 6.15. In Eqn. 6.15, the number of iterations to perform is not known in advance. Thus, a stopping parameter N controls the number of iterations required for the anisotropic diffusion and in essence, it acts as stopping time. By adjusting the parameter N, the amount of speckle removed can be varied, resulting in less or more smoothing, depending on the input image used and the amount of speckle present. There is a trade-off between the integration constant, Δt, and the iteration parameter N [16]. A small value of Δt will yield a good approximation for the partial differential equation of the fuzzy anisotropic diffusion however, it requires many iteration steps (i.e. large N value.).

6.3.1 Digital implementation of interval type II fuzzy anisotropic diffusion algorithm

According to Intajag et.al.[24] anisotropic diffusion algorithms were originally designed for additive noise. However, speckle noise is multiplicative in nature. Multiplicative noise can be transformed into additive noise by a logarithmic transformation. Therefore, the first step in the image enhancement algorithm involves transformation of the image into log domain.

In Eqn. 6.14, the diffusion coefficients are separate for each of the Up, Down, Left, and Right orientations. Similarly, for the interval type II fuzzy anisotropic diffusion, the coefficients are separate for each of the orientations. Fuzzy diffusion coefficient is calculated as the minimum of the center pixel and its neighbouring pixel. The minimum operator is used to ensure that the diffusion process will not occur in the corresponding direction as soon as one pixel in that direction reaches an edge [57]. The interval type II fuzzy diffusion coefficients are given by the following equations:

$$
\begin{aligned}
C_N(x,y,t) &= \frac{1}{2}\sum_{\rho\in\{Upper,Lower\}} min\Big[\mu_A^\rho(E(x,y,t))\cdot\mu_B^\rho(N(x,y,t)),\\
&\quad \mu_A^\rho(E(x-1,y,t))\cdot\mu_B^\rho(N(x-1,y,t))\Big] \qquad (6.16)
\end{aligned}
$$

$$
\begin{aligned}
C_S(x,y,t) &= \frac{1}{2}\sum_{\rho\in\{Upper,Lower\}} min\Big[\mu_A^\rho(E(x,y,t))\cdot\mu_B^\rho(N(x,y,t)),\\
&\quad \mu_A^\rho(E(x+1,y,t))\cdot\mu_B^\rho(N(x+1,y,t))\Big] \qquad (6.17)
\end{aligned}
$$

$$
\begin{aligned}
C_E(x,y,t) &= \frac{1}{2}\sum_{\rho\in\{Upper,Lower\}} min\Big[\mu_A^\rho(E(x,y,t))\cdot\mu_B^\rho(N(x,y,t)),\\
&\quad \mu_A^\rho(E(x,y+1,t))\cdot\mu_B^\rho(N(x,y+1,t))\Big] \qquad (6.18)
\end{aligned}
$$

$$
\begin{aligned}
C_W(x,y,t) &= \frac{1}{2}\sum_{\rho\in\{Upper,Lower\}} min\Big[\mu_A^\rho(E(x,y,t))\cdot\mu_B^\rho(N(x,y,t)),\\
&\quad \mu_A^\rho(E(x,y-1,t))\cdot\mu_B^\rho(N(x,y-1,t))\Big] \qquad (6.19)
\end{aligned}
$$

In Eqn. 6.16, 6.17, 6.18, and 6.19, A and B represents the fuzzy sets “edginess” and “noisiness” respectively. $E(x,y,t)$ and $N(x,y,t)$ are represented by Eqn. 6.6 and 6.7 respectively. The interval type II fuzzy anisotropic diffusion is given by the following equation:

$$I(x,y,t+1) = I(x,y,t) + \Delta t(\Phi_E - \Phi_W + \Phi_N - \Phi_S) \qquad (6.20)$$

Φ_E, Φ_W, Φ_N, and Φ_S are defined in Eqn. 6.14 and the coefficients $C_N(x,y,t)$, $C_S(x,y,t)$, $C_E(x,y,t)$, and $C_W(x,y,t)$ are defined by Eqn. 6.16, 6.17, 6.18, and 6.19.

Chapter 7

Algorithm results and analysis

The interval type II fuzzy speckle noise reduction algorithms were implemented in MATLAB (v.7.0.1) and the performance of the algorithms were evaluated using well-known speckle-reduction performance metrics for images; they include the signal-to-noise ratio (SNR), contrast-to-noise ratio (CNR), equivalent number of looks (ENL), edge preservation ($\in$), and structure similarity index (SSIM). The image quality metrics definitions as described in references [3, 41, 49, 65] are presented below.

$$SNR = 10log_{10}\left[\frac{max(I^2)}{\sigma_n^2}\right] \tag{7.1}$$

In the expression for SNR (Eqn. 7.1), I and σ_n^2 represent the linear magnitude image and the variance of the background noise region in the linear magnitude image respectively.

$$ENL = \frac{1}{H}\left[\sum_{h=1}^{H}\frac{\mu_h^2}{\sigma_h^2}\right] \tag{7.2}$$

ENL measures the smoothness of a homogenous region of interest. ENL measurement can show the smoothness in regions on the image that are suppose to have homogeneous appearance but are corrupted by speckle noise. In the expression for ENL (Eqn. 7.2), μ_h and σ_h^2 represent the mean and variance of the h^{th} homogenous region of interests respectively.

$$CNR = \frac{1}{R}\left[\sum_{r=1}^{R}\frac{(\mu_r - \mu_b)}{\sqrt{\sigma_r^2 + \sigma_b^2}}\right] \tag{7.3}$$

CNR provides an objective measure of useful contrast between an area of image feature and an area of background noise. In the definition of CNR (Eqn. 7.3), μ_b and σ_b^2 represent the mean and variance of the same background noise region as in

SNR and μ_r and σ_r^2 represent the mean and variance of the r^{th} region of interest which includes the homogeneous regions.

$$\in = \frac{\sum_{(i,j)}(\Delta I_{i,j} - \bar{\Delta}\bar{I}_{i,j}) \cdot (\Delta\hat{I}_{i,j} - \Delta\bar{\hat{I}}_{i,j})}{\sqrt{\sum_{(i,j)}(\Delta I_{i,j} - \bar{\Delta}\bar{I}_{i,j}) \cdot (\Delta I_{i,j} - \bar{\Delta}\bar{I}_{i,j}) \cdot \sum_{(i,j)}(\Delta\hat{I}_{i,j} - \Delta\bar{\hat{I}}_{i,j}) \cdot (\Delta\hat{I}_{i,j} - \Delta\bar{\hat{I}}_{i,j})}} \tag{7.4}$$

Since, the interest is in reducing speckle noise while at the same time preserving the edges of the original image, a qualitative measure for edge preservation is used. Edge preservation ($\in$) is a correlation measure that indicates how the edges in the image are degrading. An edge preservation value close to unity indicates the filtered image is similar to the original image. In the edge preservation measure (Eqn. 7.4), $\Delta I_{i,j}$ and $\Delta\hat{I}_{i,j}$ represent the Laplace operator performed on the original image I and the filtered image $\hat{I}$ respectively. Also, $\Delta\bar{I}_{i,j}$ and $\Delta\bar{\hat{I}}_{i,j}$ represent the mean value of a $3x3$ neighbourhood around the pixel location (i, j) of ΔI and $\Delta\hat{I}_{i,j}$ respectively.

$$SSIM(X,Y) = \frac{4\sigma_{xy}\bar{x}\bar{y}}{(\sigma_x^2 + \sigma_y^2)[(\bar{x})^2 + (\bar{y})^2]} \tag{7.5}$$

Structure similarity index is a measure to compare the luminance, contrast, and structure of two different images [65]. Here, the original image and the filtered images are used for the SSIM measurement. The dynamic range for SSIM is $[-1, 1]$. In the expression for SSIM (Eqn. 7.5), X and Y represents original and denoised images, respectively. μ_x and μ_y are the mean intensities of the images and σ_x^2 and σ_y^2 are the variance of images. σ_{xy} is the covariance between the original image (X) and denoised image (Y). Following a previous work [3], all the image metric calculations were performed in logarithmic domain of an OCT image except for the SNR and SSIM calculations.

The algorithms were tested on various images obtained from the high speed, ultrahigh resolution FD-OCT system mentioned in section 2.3 (FD-OCT operating at $1060nm$). Fig. 7.1 shows the images that were obtained in-vivo from the cornea of a human volunteer (A), retina of a human volunteer (B and C), fingertip of a human volunteer (D), and retina of living rats (E). The tomograms were acquired at the rate of $47,000 A-scans/s$. The image size is $2000x512$ (A-scans x pixels) for the human retina, $1000x512$ (A-scans x pixels) for the human cornea, human fingertip and the rat retina. In Fig. 7.1, the layered structures of the retina, cornea, and the fingertip is labelled with the following: nerve fiber layer (NFL), ganglion cell layer (GCL), inner plexiform layer (IPL), inner nuclear layer (INL), outer plexiform layer (OPL), outer nuclear layer (ONL), external limiting membrane (ELM), photoreceptor inner and outer segment junction (IS/OS), retinal pigment epithelium (RPE), choriocapillaris (CC), sclera (S), ephithelium (EPH), basement membrane (BM), dermis (D), and subcutis (SC). These images provide details into the different tissue structures that can be imaged with OCT. Algorithms must be tested on

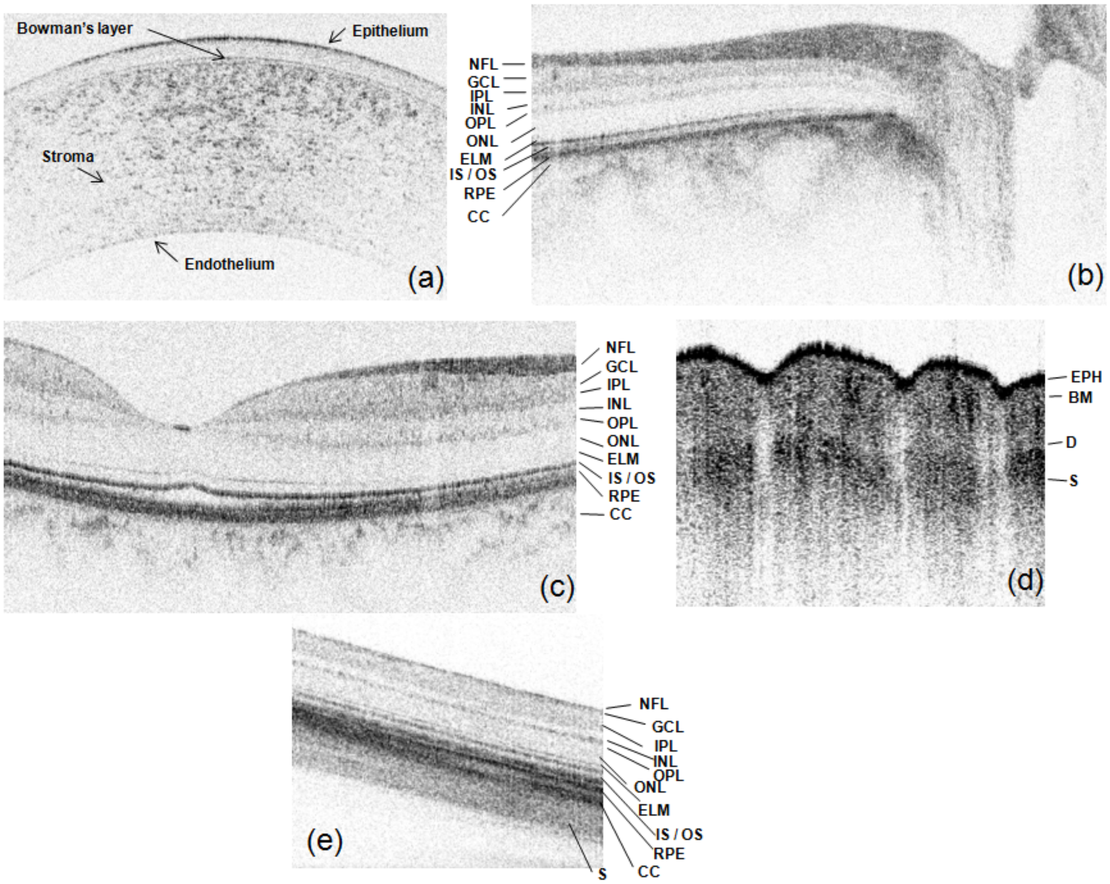

Figure 7.1: Ultrahigh resolution FD-OCT images used for testing of the algorithms. a) human cornea b) human optical disk c) human fovea d) human fingertip and e) rat retina. The size of the tomograms is 2000 x 512 (A-scans x pixels) for the human retina and 1000 x 512 for the human cornea, human fingertip and rat retina.

variety of images to find its strength and weakness. By fine tuning the algorithm parameters to each image, optimal results can be achieved.

The next section details the experimental results obtained from applying the algorithms on simulated speckle noise. The remaining subsequent sections detail the results of applying the algorithms on the test images in Fig. 7.1.

7.1 Simulated speckle noise

The experiment was initially conducted on a standard test image (cameraman) with a pixel dimension of $256x256$. This image was corrupted with normally distributed speckle noise with mean of 1 and at different noise levels. To assess the performance of the fuzzy wavelet and anisotropic diffusion algorithms, results were compared with the median, Wiener [30] and modified adaptive Lee filters [33]. To quantify the achieved performance, the root mean square error (RMSE) quality measure was computed using the original test image and denoised image. The image metrics discussed above are not used for the simulated speckle noise because the true image is known. Table 7.1 summarizes the root mean square error for the Cameraman test image for the various noise levels. The original image, noisy image, and the filtered images are shown in Fig.7.2 for a specific speckle noise variance. Qualitatively, the results show that interval type II algorithms removes the simulated speckle noise without distorting useful image information and without destroying important edges. Quantitatively, the RMSE is lowest for all the noise levels for both the fuzzy anisotropic diffusion and fuzzy wavelet algorithms. Fuzzy wavelet algorithm has lower RMSE value than fuzzy anisotropic diffusion algorithm for very high and very low noise levels.

Table 7.1: RMSE metric evaluated for Cameraman test image

σ_n^2	Wiener	Adpative Lee	Median	Fuzzy II diffusion	Fuzzy II Wavelet
0.01	0.038	0.058	0.108	0.033	**0.032**
0.02	0.049	0.063	0.110	0.046	**0.042**
0.03	0.057	0.065	0.111	0.050	**0.047**
0.04	0.063	0.068	0.112	**0.053**	0.055
0.05	0.068	0.072	0.114	**0.056**	0.058
0.06	0.074	0.074	0.116	**0.060**	0.061
0.07	0.077	0.076	0.117	**0.064**	**0.064**
0.08	0.082	0.080	0.119	**0.066**	0.067
0.09	0.087	0.084	0.121	**0.069**	0.070
0.1	0.088	0.085	0.122	**0.070**	0.072
0.2	0.109	0.106	0.138	**0.085**	0.097
0.3	0.121	0.119	0.152	**0.099**	0.119
0.4	0.129	0.129	0.166	0.111	**0.106**
0.5	0.133	0.133	0.174	0.119	**0.111**
0.6	0.136	0.136	0.181	0.125	**0.117**
0.7	0.141	0.141	0.188	0.129	**0.123**
0.8	0.142	0.142	0.193	0.132	**0.125**
0.9	0.143	0.143	0.198	0.139	**0.129**

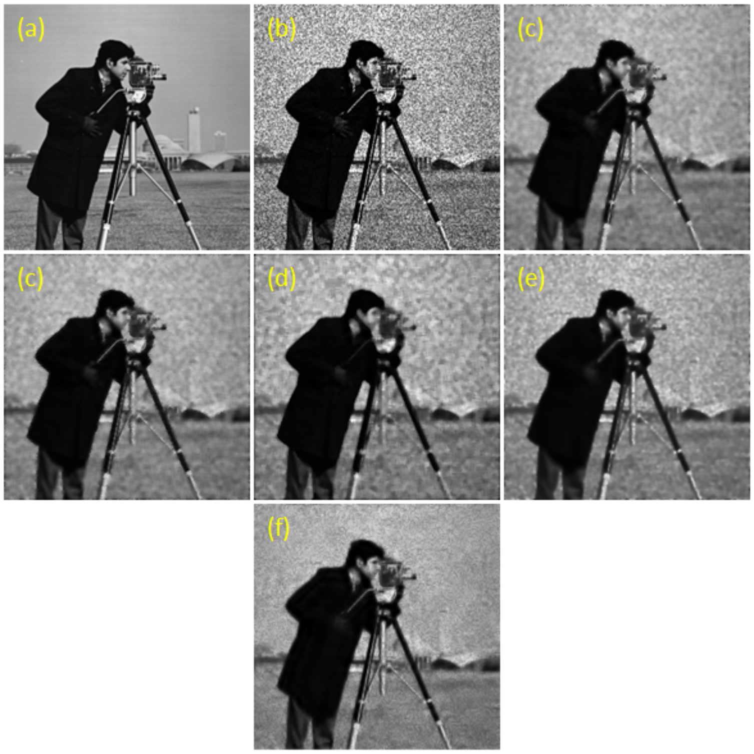

Figure 7.2: Cameraman test image. a) Original image b) simulated speckle with $\sigma_n^2 = 0.1$ c) Wiener filtered d) Lee filtered e) median filtered f) fuzzy type II anisotropic diffusion filtered and g) fuzzy type II wavelet filtered. The size of the image is 256 x 256 (pixels x pixels).

7.2 Human Cornea

Fig. 7.3(a) shows the unprocessed human cornea which has a grainy appearance due to the presence of speckle noise. Eight regions of interest on the image have been marked. These regions were used in the calculation for the image metrics CNR and ENL. Regions labelled (1 and 2) are the background, regions labelled (3 and 4) are the homogeneous regions while the rest are the non-homogeneous regions. These regions were selected because they contain blood vessels and important image features. The CNR and ENL image metrics are discussed in the algorithm comparison section 7.8. The processed images after it has been optimized for the parameters C_A and K_B is shown in Fig. 7.3(b) and (c).

The optimization curves are displayed on Fig. 7.3(d) and (e). The center C_A is part of the fuzzy wavelet algorithm that controls the location of the membership function of the type II fuzzy set A which corresponds to the large magnitude wavelet coefficient. The parameter K_B is part of the fuzzy anisotropic diffusion algorithm and it controls the shape of the membership function of the type II fuzzy set B which corresponds to high noisiness measure. The filtered images have reduced granular

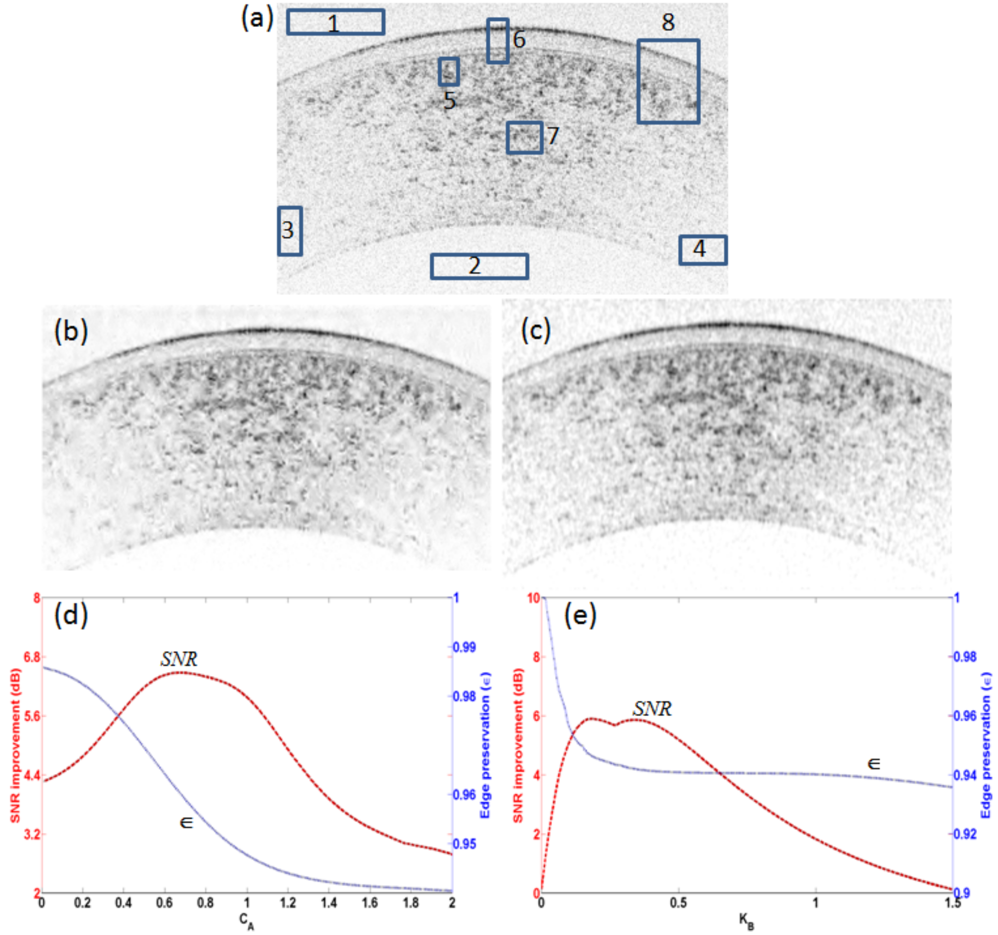

Figure 7.3: Fuzzy filtering of a human cornea image acquired with the FD-OCT 1060nm system: a) original image b) Interval type II fuzzy wavelet filtered image with optimal SNR parameter c) Interval type II fuzzy anisotropic diffusion filtered image with optimal SNR parameter d) SNR improvement and edge preservation curves for the interval type II fuzzy wavelet algorithm using the center of fuzzy set A (C_A) as the optimization parameter and e) SNR improvement and edge preservation curves for the interval type II fuzzy anisotropic diffusion algorithm using the shape parameter of fuzzy set B (K_B) as the optimization parameter. The images are 1000 x 512 (lateral x axial) pixels dimensions. The regions in (a), identified with numbers 1 to 8 are used for CNR and ENL image metrics.

appearance with enhancement between the Bowman's layer and the Epithelium. The trade-off between the SNR improvement and edge details can be seen in the optimization curve. Maximum SNR improvement of $6.47dB$ is achieved for $C_A = 0.68$ and SNR of $5.89dB$ for $K_B = 0.19$. Increase in SNR improvement result in reduction of edge sharpness.

7.3 Human Retina - Fovea

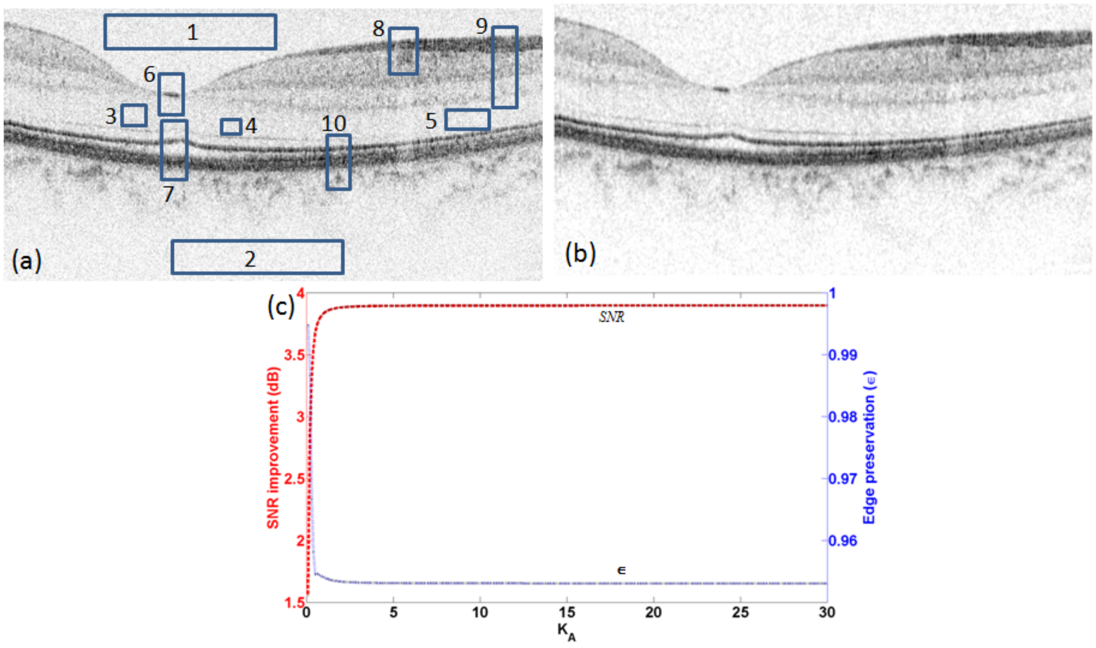

Figure 7.4: Fuzzy filtering of a human retinal (fovea) image acquired with the FD-OCT 1060nm system: a) original image b) Interval type II fuzzy anisotropic diffusion filtered image with optimal SNR parameter c) SNR improvement and edge preservation curves for the interval type II fuzzy anisotropic diffusion algorithm using the shape parameter of fuzzy set A (K_A) as the optimization parameter. The images are 2000 x 512 (lateral x axial) pixels dimensions. The regions in (a), identified with numbers 1 to 10 are used for CNR and ENL image metrics.

Fig. 7.4(a) shows the unprocessed human fovea that has grainy appearance due to the presence of speckle noise. Ten regions of interest on the image have been marked. These regions were used in the calculation for the image metrics CNR and ENL. Regions labelled (1 and 2) are the background, regions labelled (3, 4, and 5) are the homogeneous regions while the rest are the non-homogeneous regions. These regions were selected because they contain blood vessels and important image features. The CNR and ENL image metrics are discussed in the algorithm comparison section 7.8. The processed image after it has been optimized for the parameter K_A is shown in Fig. 7.4(b). The optimization curve is displayed on Fig.

7.4(c). The parameter K_A is part of the fuzzy anisotropic diffusion algorithm and it controls the shape of the membership function of the type II fuzzy set A which corresponds to low edginess measure. The filtered images show reduced granular appearance with enhanced boundary between the nerve fiber layer and ganglion cell layer. The trade-off between the SNR improvement and edge details can be seen in the optimization curve. Maximum SNR improvement of $3.90dB$ is achieved for $K_A = 30$. However, the SNR improvement curve taper off after $K_A = 5$. Increase in SNR improvement results in reduction of edge sharpness.

7.4 Human Retina - Optical Disk

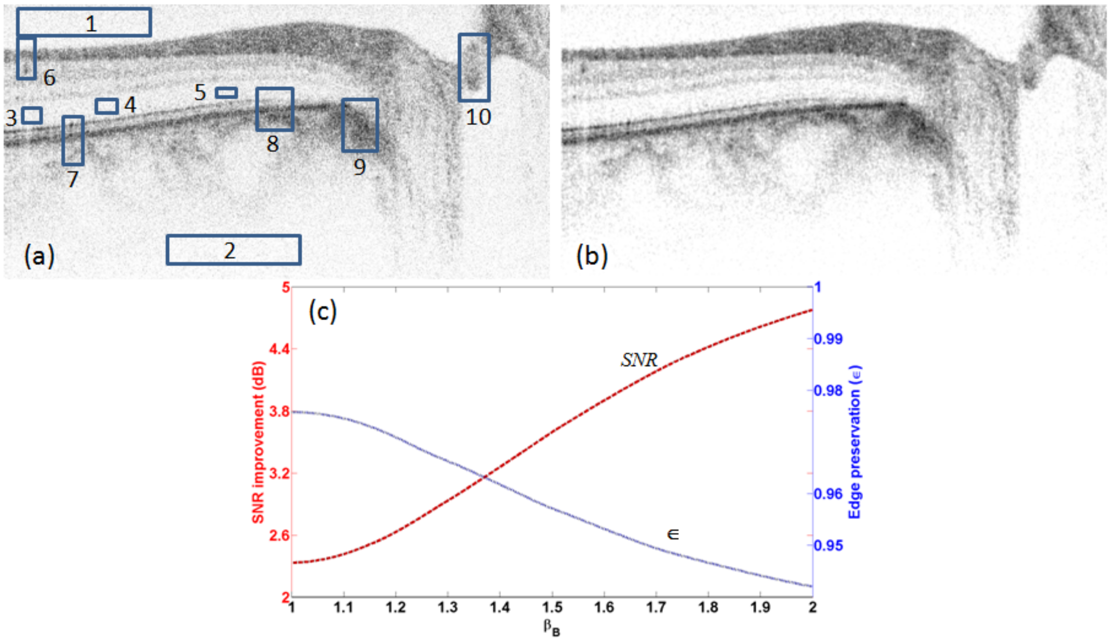

Figure 7.5: Fuzzy filtering of a human retinal (Optical Disk) image acquired with the FD-OCT 1060nm system: a) original image b) Interval type II fuzzy anisotropic diffusion filtered image with optimal SNR parameter c) SNR improvement and edge preservation curves for the interval type II fuzzy anisotropic diffusion algorithm using width of the footprint of uncertainty of fuzzy set B (β_B) as the optimization parameter. The images are 2000 x 512 (lateral x axial) pixels dimensions. The regions in (a), identified with numbers 1 to 10 are used for CNR and ENL image metrics.

Fig. 7.5(a) shows the unprocessed human optical disk that has grainy appearance due to the presence of speckle noise. Ten regions of interest on the image have been marked. These regions were used in the calculation for the image metrics CNR and ENL. Regions labelled (1 and 2) are the background, regions labelled (3, 4, and 5) are the homogeneous regions while the rest are the non-homogeneous regions.

These regions were selected because they contain blood vessels and important image features. The CNR and ENL image metrics are discussed in the algorithm comparison section 7.8. The processed image after it has been optimized for the parameter β_B is shown in Fig. 7.5(b). The optimization curve is displayed on Fig. 7.5(c). The parameter β_B is part of the fuzzy anisotropic diffusion algorithm and it controls the width of the footprint of uncertainty in the interval type II fuzzy set B which corresponds to high noisiness measure. The filtered image shows clear distinction between the outer nuclear layer and external limiting membrane with reduced granular appearance. The trade-off between the SNR improvement and edge details can be seen in the optimization curve. Maximum SNR improvement of $4.78dB$ is achieved for $\beta_B = 2$. The SNR continues to improve for $\beta_B > 2$, however as mentioned before, β_B value greater than 2 is not meaningful for image data [62]. Increase in SNR improvement results in reduction of edge sharpness.

7.5 Human Fingertip

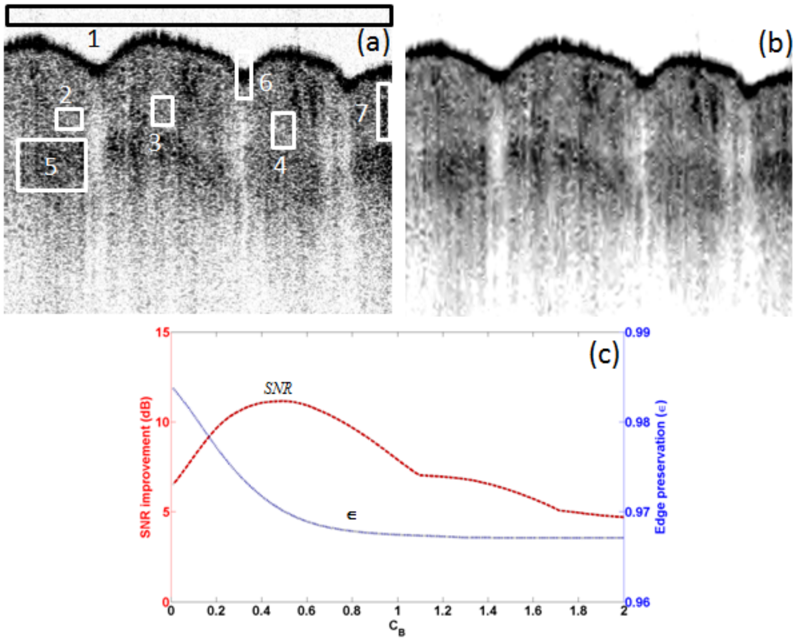

Figure 7.6: Fuzzy filtering of a human fingertip image acquired with the FD-OCT 1060nm system: a) original image b) Interval type II fuzzy wavelet filtered image with optimal SNR parameter c) SNR improvement and edge preservation curves for the interval type II fuzzy wavelet algorithm using the center of fuzzy set B (C_B) as the optimization parameter. The images are 1000 x 512 (lateral x axial) pixels dimensions. The regions in (a), identified with numbers 1 to 7 are used for CNR and ENL image metrics.

Fig. 7.6(a) shows the unprocessed human fingertip image that has grainy appearance due to the presence of speckle noise. Six regions of interest (homogeneous regions labelled 2, 3, and 4) and background region (labelled 1) above the tissue were selected and marked on the image. The rest are the non-homogeneous regions. These regions were used in the calculation for the image metrics CNR and ENL. These regions were selected because they contain sweat glands and important image features. The CNR and ENL image metrics are discussed in the algorithm comparison section 7.8. The processed image after it has been optimized for the parameter C_B is shown in Fig. 7.6(b). The optimization curve is displayed on Fig. 7.6(c). The center C_B is part of the fuzzy wavelet algorithm that controls the location of the membership function of the type II fuzzy set B which corresponds to the large correlation map value. The filtered image shows clear distinction between the ephithelium and basement membrane with reduced granular appearance. The trade-off between the SNR improvement and edge details can be seen in the optimization curve. Maximum SNR improvement of $11.15dB$ is achieved for $C_B = 0.49$. Increase in SNR improvement results in reduction of edge sharpness, however the edge sharpness taper off after maximum SNR improvement is achieved.

7.6 Rat Retina

Fig. 7.7(A) shows the unprocessed rat retinal image that has grainy appearance due to the presence of speckle noise. Seven regions of interest on the image have been marked. These regions were used in the calculation for the image metrics CNR and ENL. Regions labelled (1 and 2) are the background, regions labelled (3 and 4) are the homogeneous regions while the rest are the non-homogeneous regions. These regions were selected because they contain blood vessels and important image features. The CNR and ENL image metrics are discussed in the algorithm comparison section 7.8. The processed image after it has been optimized for the parameters β_B and β_A are shown in Fig. 7.7(B) and (C) respectively. The optimization curve is displayed on Fig. 7.7(D) and (E). The parameters β_B and β_A control the foot print of uncertainty of type II fuzzy set B in fuzzy wavelet algorithm and type II fuzzy set A in fuzzy anisotropic diffusion algorithm. Fuzzy set B corresponds to the large correlation map value and fuzzy set A corresponds to low edginess measure. The filtered images show clear distinction between the choriocapillaris and sclera layers with reduced granular appearance. The trade-off between the SNR improvement and edge details can be seen in the optimization curves. Maximum SNR improvement of $9.41dB$ for $\beta_B = 2$ and $3.16dB$ for $\beta_A = 2$ is achieved. Increase in SNR improvement results in reduction of edge sharpness. The SNR continues to improve for $\beta_B > 2$ and $\beta_A > 2$, however as mentioned before, β values greater than 2 is not meaningful for image data [62].

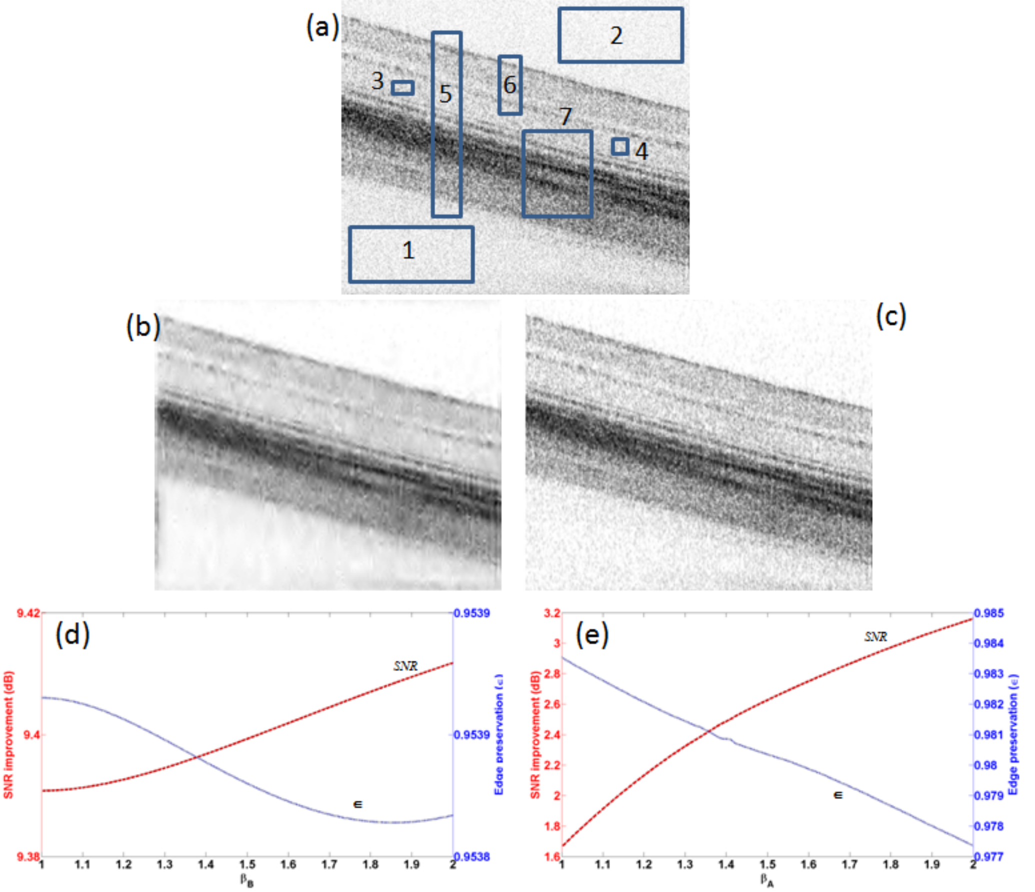

Figure 7.7: Fuzzy filtering of a rat retinal image acquired with the FD-OCT 1060nm system: a) original image b) Interval type II fuzzy wavelet filtered image with optimal SNR parameter c) Interval type II fuzzy anisotropic diffusion filtered image with optimal SNR parameter d) SNR improvement and edge preservation curves for the interval type II fuzzy wavelet algorithm using the width of the footprint of uncertainty of fuzzy set B (β_B) as the optimization parameter and e) SNR improvement and edge preservation curves for the interval type II fuzzy anisotropic diffusion algorithm using the width of the footprint of uncertainty of fuzzy set A (β_A) as the optimization parameter. The images are 1000 x 512 (lateral x axial) pixels dimensions. The regions in (a), identified with numbers 1 to 7 are used for CNR and ENL image metrics.

7.7 Comparison

The effect of interval type II fuzzy set versus type I fuzzy set on the despeckling algorithms can be seen on Fig. 7.8A and 7.8B. Fig. 7.8 A and B shows the optimization of SNR for the image in Fig. 7.11. Fig. 7.8A is the optimization curve for type I and type II fuzzy anisotropic diffusion algorithm. The algorithms were optimized for the iteration parameter N. It is clear that interval type II fuzzy anisotropic diffusion achieves optimum SNR faster at (N=50) and the edge preservation values are identical. Similarly, Fig. 7.8B is the optimization curve for type I and type II fuzzy wavelet algorithm. The optimization is done for the width (W) of the membership functions. Once again, the type II fuzzy set based algorithm reaches optimum SNR faster. The edge preservation ($\in$) values are identical for both type I fuzzy wavelet and type II fuzzy wavelet. For the same parameters, type II fuzzy set based algorithms (both anisotropic diffusion and wavelet) provide higher SNR values with almost identical edge preservation values. This indicates that the edginess in the image filtered by both type I and type II algorithms are the same but the algorithm based on interval type II fuzzy set gives higher SNR.

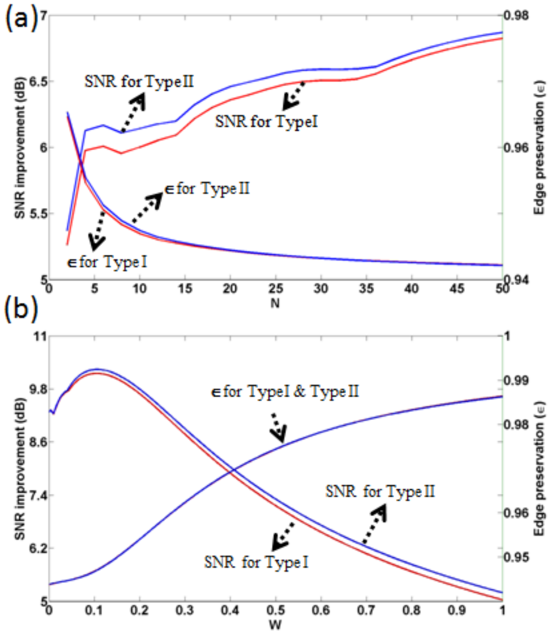

Figure 7.8: Comparison of interval type II and type I fuzzy algorithms a) SNR and edge preservation curves for both type I and type II fuzzy anisotropic diffusion algorithms with iteration number (N) as the optimization parameter b) SNR and edge preservation curves for both type I and type II fuzzy wavelet algorithms with width (W) of the membership function as the optimization parameter.

To evaluate the performance of the novel Fuzzy type II algorithms, they were applied to OCT images acquired in-vivo from a human fingertip and a human retina (optical disk), with a high speed, high resolution Fourier Domain OCT system (FD-

OCT) operating in the 1060nm wavelength region. To compare the performance of our algorithm with other, well established speckle reduction algorithms, Wiener filter [30] that was provided by Matlab via the *wiener2()* function, and a modified adaptive Lee filter implemented using an algorithm described in reference [33] were applied to the images as well. Also applied was the median filter. The Wiener filter and the adaptive Lee filter were previously applied to OCT images and they showed valuable results [41]. In addition, a type I fuzzy wavelet and type I fuzzy anisotropic diffusion algorithms were also applied to the fingertip and retinal images. This was done to directly evaluate the effect of the fuzzy type II set when combined with wavelet and anisotropic diffusion.

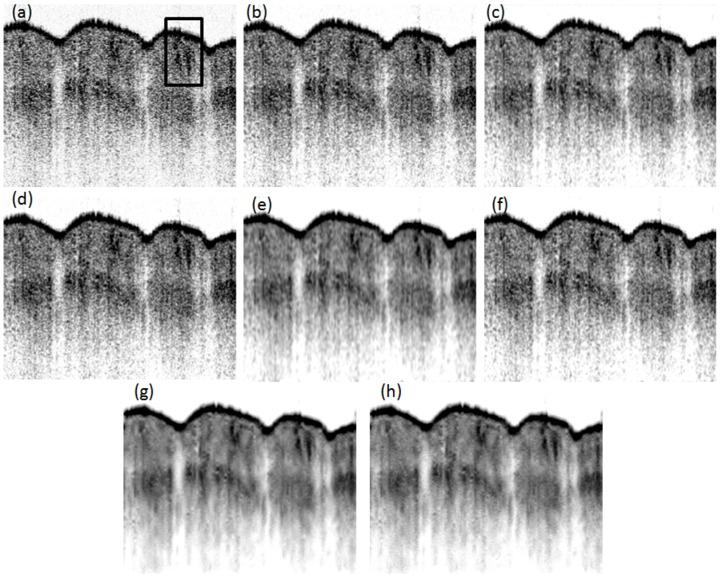

Figure 7.9: Denoising of a human fingertip image acquired with the FD-OCT 1060nm system: A) Original OCT image. B) Median filtered. C) Wiener filtered. D) Adaptive Lee filtered. E) Type I fuzzy anisotropic diffusion filtered. F) Type II fuzzy anisotropic diffusion filtered. G) Type I fuzzy wavelet filtered and H) Type II fuzzy wavelet filtered. The images are 1000 x 512 (lateral x axial) pixels dimension. The box in A) marks a sweat gland in the epidermis layer. This region has been enlarged and shown in Fig. 7.10.

First of all, the Wiener, the adaptive Lee, the median, fuzzy type I and fuzzy type II algorithms were applied to an OCT image of a human fingertip with dimensions 1000 x 512(A-scans x pixels). Fig. 7.9A shows the unprocessed OCT fingertip tomogram that has grainy appearance due to the presence of speckle. A region in the image, marked with a box and containing what we believe are sweat glands in the epidermal layer was enlarged by 2x and is shown in Fig. 7.10A. Fig. 7.9B shows the same image after median filtering and a similar enlarged region is shown in Fig. 7.10B. Similarly, Fig. 7.9C is the result of Wiener filtering with corresponding enlarged region in Fig. 7.10C. Fig. 7.9D through H shows the OCT image after adaptive Lee, type I fuzzy anisotropic diffusion, type II fuzzy

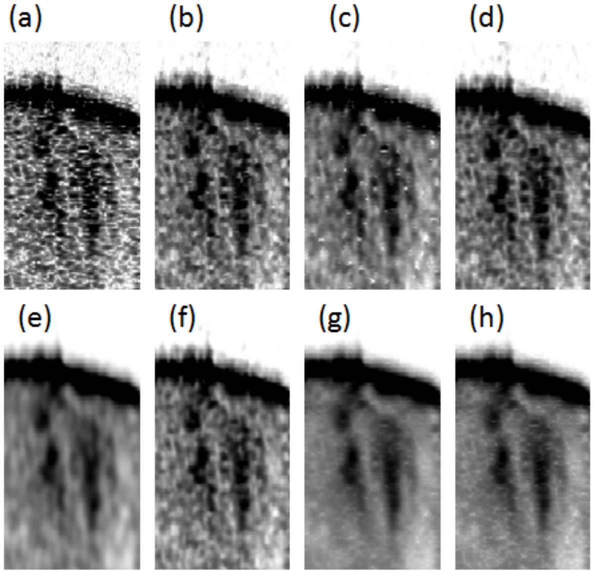

Figure 7.10: A region containing sweat glands from Fig. 7.9 has been enlarged 2x for close comparison of the performance of the algorithms. A) Original OCT image. B) Median filtered. C) Wiener filtered. D) Adaptive Lee filtered. E) Type I fuzzy anisotropic diffusion filtered. F) Type II fuzzy anisotropic diffusion filtered. G) Type I fuzzy wavelet filtered and H) Type II fuzzy wavelet filtered.

anisotropic diffusion, type I fuzzy wavelet and type II fuzzy wavelet filtering respectively and their enlarged region is shown in Fig. 7.10D through H. All the filters reduced the appearance of speckle pattern. Both the Wiener and Lee filters are based on the optimal minimum mean square error estimator of the true image. Both filters appear to reduce the speckle pattern, yet in homogenous regions some speckle patterns are still clearly visible. The type II fuzzy anisotropic diffusion filtered image, shown on Fig. 7.9F exhibits clear edges of tissue features (for example in the sweat glands) and significantly reduced appearance of speckle patterns as compared to the Wiener and Lee filtered images. Note that the same gray scale was used in all images and the scale was not altered after the application of the different filters. Enlarged views of the sweat gland region are presented in Fig. 7.10A (unprocessed image), 7.10B (median filter), 7.10C (Wiener filter), 7.10D (adaptive Lee filter), 7.10E (type I fuzzy anisotropic diffusion), 7.10F (type II fuzzy anisotropic diffusion), 7.10G (type I fuzzy wavelet) and 7.10 (type II fuzzy wavelet) for easy comparison of the effect of filtering on the presence of a speckle pattern. Fig. 7.10A-H show that the median, Wiener and adaptive Lee filters reduced the speckle noise in the images, while preserving edges of the sweat gland. However, for all three filters there are some residual speckle patterns still visible in the background tissue. The type I fuzzy anisotropic diffusion filtered image (7.10E) shows practically no presence of speckle noise, achieved at the expense of significant blurring of edges and tissue features such as the sweat glands. Both type I and type II fuzzy wavelet filtered images look blurred but less in comparison to type I anisotropic diffusion. However, there is still some residual speckle patterns visible. The fuzzy type II anisotropic diffusion filter shows significantly improved reduction in the speckle pattern with very good preservation of image features and edges. Note that both the regular anisotropic diffusion and the fuzzy type II anisotropic diffusion filters were run for the same number of iterations (N = 15).

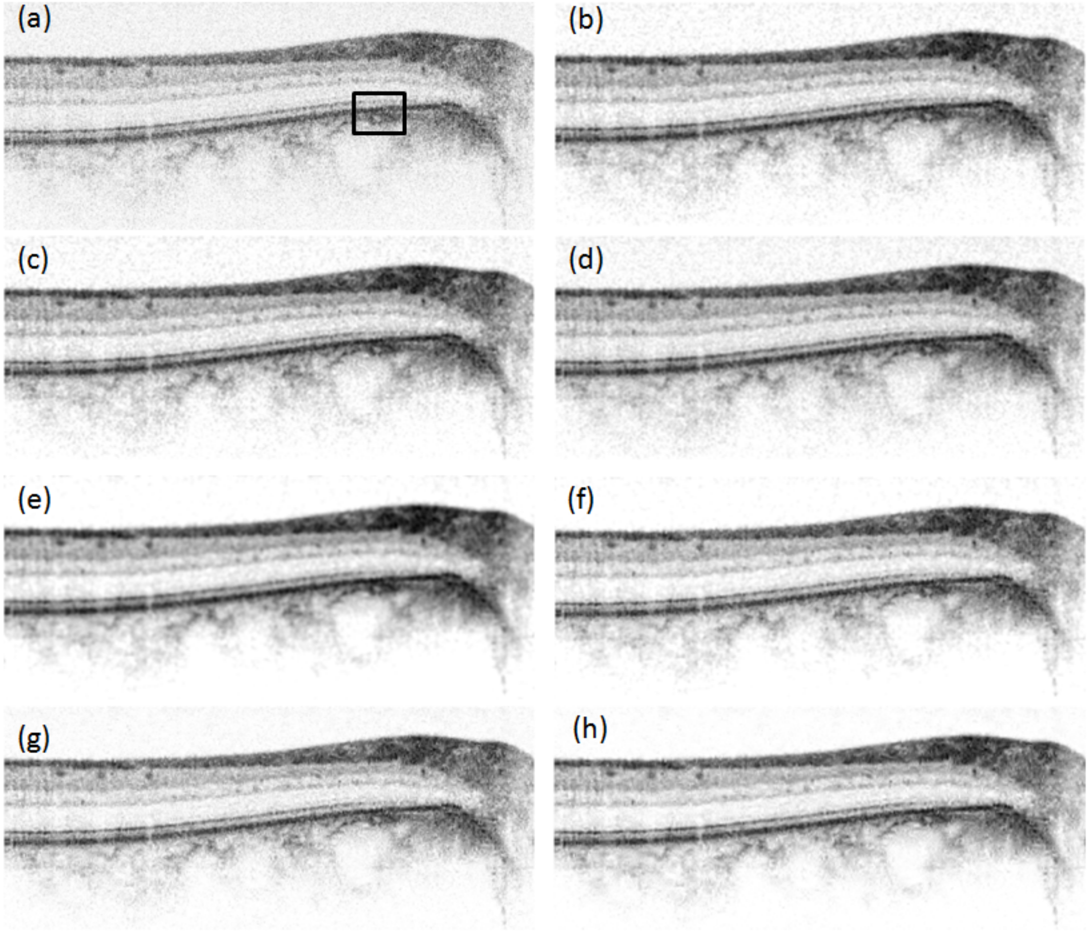

Figure 7.11: Denoising of a human optical disk image acquired with the FD-OCT 1060nm system: A) Original OCT image. B) Median filtered. C) Wiener filtered. D) Adaptive Lee filtered. E) Type I fuzzy anisotropic diffusion filtered. F) Type II fuzzy anisotropic diffusion filtered. G) Type I fuzzy wavelet filtered and H) Type II fuzzy wavelet filtered. The images are 2000 x 512 (lateral x axial) pixels dimension. The box in A) marks a region containing a blood-vessel. This region has been enlarged and shown in Fig. 7.12.

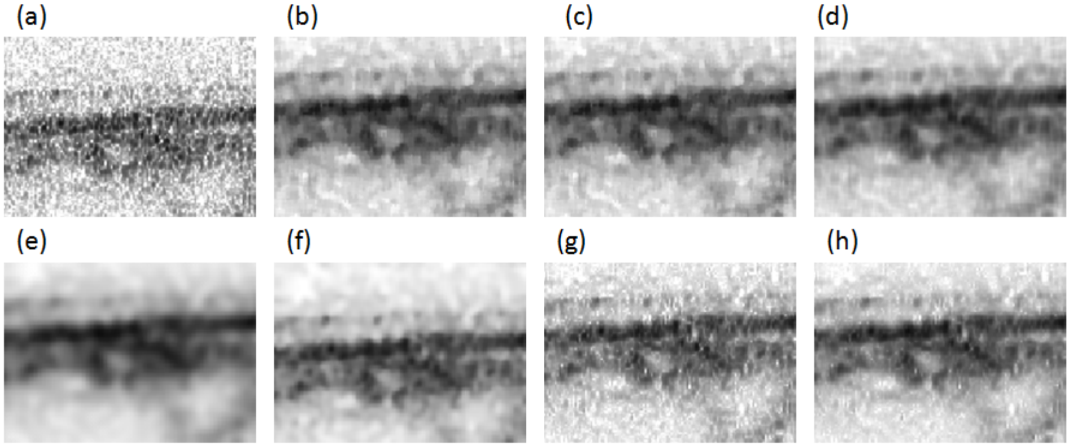

Figure 7.12: A region containing blood vessel from Fig. 7.11 has been enlarged 2x for close comparison of the performance of the algorithms. A) Original OCT image. B) Median filtered. C) Wiener filtered. D) Adaptive Lee filtered. E) Type I fuzzy anisotropic diffusion filtered. F) Type II fuzzy anisotropic diffusion filtered. G) Type I fuzzy wavelet filtered and H) Type II fuzzy wavelet filtered.

The filters were also applied to an OCT image of a human retina with dimensions 2000 x 512 (A-scans x pixels) acquired ex-vivo from human retina in the vicinity of the optical disk (7.11). Fig. 7.11A shows the unprocessed retinal tomogram that has grainy appearance due to the presence of speckle. A region in the image, marked with a box and containing a retinal blood vessel was enlarged by 2x and is shown in Fig. 7.12. The filtered images show clear visualization of the layered structures of the retina. Fig. 7.11 B, C and D shows the same OCT image in 7.11A after median, Wiener, and adaptive Lee filtering respectively. All three filters appear to reduce the speckle pattern, yet again in homogenous regions some speckle patterns are still clearly visible. Fig. 7.11E presents the image processed with the type I fuzzy anisotropic diffusion algorithm, which shows no residual speckle noise pattern and significant blurring of the edges of image features. The interval type II fuzzy wavelet filtered image, shown on Fig. 7.11H exhibits clear edges both in the case of the Retinal Pigmented Epithelium (RPE) and the walls of the small blood vessel (box in Fig. 7.11A), as well as significantly reduced appearance of speckle pattern. Note that the same gray scale was used in all filtered images and the scale was not altered after application of the different filters. Enlarged views of the magnified blood vessel are presented in Fig. 7.12A (unprocessed image), 7.12B (median filter), 7.12C (Wiener filter), 7.12D(adaptive Lee filter), 7.12E (type I fuzzy anisotropic diffusion filter), 7.12F (type II fuzzy anisotropic diffusion filter), 7.12G (type I fuzzy wavelet filter), and 7.12H (type II fuzzy wavelet filter) for easy comparison of the effect of filtering on the presence of a speckle pattern. It is clear from Fig. 7.12A-H, that the median, the Wiener and the adaptive Lee filters reduce significantly speckle noise in the images, while preserving the edges of the blood vessel walls. Some residual speckle pattern is still visible in the background tissue on Fig. 7.12B, C and D. The type I fuzzy anisotropic diffusion filtered image (Fig. 7.12E) shows practically no presence of speckle noise, achieved at the expense of significant blurring of edges of tissue features such as the blood vessel. The interval type II fuzzy wavelet filter shows improved reduction in the speckle pattern in fairly homogeneous parts of the OCT tomogram with very good preservation of image features and edges. Note that both the type I and type II fuzzy wavelet filters were run for the same parameters that were optimized for the best combination of SNR.

Table 7.2: Image quality metrics evaluated for the human cornea image. CNR, SNR and ENL values are all improvements from the original image. See 7.1(a) for the image.

	CNR(dB)	SNR(dB)	ENL	EDGINESS ($\in$)	SSIM
Wiener	3.36	5.22	951	**0.96**	0.67
Median	2.38	4.52	583	0.94	0.61
Adaptive Lee	3.03	4.80	1062	0.92	0.61
Fuzzy I Wavelet	**5.61**	4.87	2362	0.94	0.47
Fuzzy II Wavelet	4.37	**6.47**	**3332**	**0.96**	0.63
Fuzzy I anisotropic diffusion	2.43	5.71	434	**0.96**	**0.80**
Fuzzy II anisotropic diffusion	3.12	5.89	763	0.95	0.68

Table 7.3: Image quality metrics evaluated for the human fingertip image. CNR, SNR and ENL values are all improvements from the original image. See 7.1(d) for the image.

	CNR(dB)	SNR(dB)	ENL	EDGINESS ($\in$)	SSIM
Wiener	2.57	3.37	430	**0.98**	**0.90**
Median	2.05	5.22	217	0.96	0.89
Adaptive Lee	2.52	4.55	322	0.96	0.89
Fuzzy I Wavelet	**3.79**	7.52	**823**	**0.98**	0.89
Fuzzy II Wavelet	**3.79**	11.15	766	0.97	0.87
Fuzzy I anisotropic diffusion	2.45	6.67	197	0.97	**0.90**
Fuzzy II anisotropic diffusion	2.53	**13.07**	220	0.96	0.89

Quantitative comparison of the filtering effect for all the algorithms was performed by evaluating the image quality metric values for all test images (see Fig. 7.1A-E and 7.11A). The results from the quantitative analysis are presented in Tables 7.2, 7.3, 7.4, 7.5, 7.6 and 7.7. Looking at Table 7.2, the use of the median, Wiener and adaptive Lee filters results in some improvement in the image SNR and CNR for the human cornea image. The application of the interval type II fuzzy

Table 7.4: Image quality metrics evaluated for the human fovea. CNR, SNR and ENL values are all improvements from the original image. See 7.1(c) for the image.

	CNR(dB)	SNR(dB)	ENL	EDGINESS (∈)	SSIM
Wiener	3.04	6.11	1389	0.94	0.78
Median	3.42	4.72	1828	0.91	0.70
Adaptive Lee	3.87	6.47	**3311**	0.91	0.70
Fuzzy I Wavelet	**4.91**	9.35	1087	0.92	0.66
Fuzzy II Wavelet	4.82	**10.53**	1335	0.92	0.68
Fuzzy I anisotropic diffusion	1.11	2.85	134	**0.96**	**0.97**
Fuzzy II anisotropic diffusion	1.56	3.90	237	0.95	0.94

Table 7.5: Image quality metrics evaluated for the human optical disk image. CNR, SNR and ENL values are all improvements from the original image. See 7.1(b) for the image.

	CNR(dB)	SNR(dB)	ENL	EDGINESS (∈)	SSIM
Wiener	3.20	3.04	1020	0.95	0.78
Median	3.60	3.06	1353	0.92	0.69
Adaptive Lee	4.04	4.36	2575	0.92	0.70
Fuzzy I Wavelet	**4.88**	3.28	7199	0.92	0.66
Fuzzy II Wavelet	4.85	**6.29**	**8784**	0.92	0.67
Fuzzy I anisotropic diffusion	1.03	2.33	98	**0.98**	**0.97**
Fuzzy II anisotropic diffusion	2.46	4.78	476	0.94	0.87

Table 7.6: Image quality metrics evaluated for the rat retina image. CNR, SNR and ENL values are all improvements from the original image. See 7.1(e) for the image.

	CNR(dB)	SNR(dB)	ENL	EDGINESS (∈)	SSIM
Wiener	3.29	7.34	1179	0.96	0.86
Median	2.57	3.86	498	0.95	0.84
Adaptive Lee	4.08	4.33	2524	0.95	0.81
Fuzzy I Wavelet	4.77	9.39	8286	0.95	0.81
Fuzzy II Wavelet	**4.78**	**9.41**	**8461**	0.95	0.81
Fuzzy I anisotropic diffusion	1.22	2.68	54	0.97	**0.96**
Fuzzy II anisotropic diffusion	1.56	3.16	122	**0.98**	**0.96**

Table 7.7: Image quality metrics evaluated for the human optical disk image. CNR, SNR and ENL values are all improvements from the original image. See comparison section 7.8 for the image.

	CNR(dB)	SNR(dB)	ENL	EDGINESS ($\in$)	SSIM
Wiener	3.05	4.94	965	**0.96**	**0.82**
Median	3.46	4.77	1537	0.94	0.76
Adaptive Lee	3.94	6.79	2414	0.94	0.76
Fuzzy I Wavelet	4.67	10.15	5285	0.95	0.77
Fuzzy II Wavelet	4.69	**10.24**	**5386**	0.95	0.77
Fuzzy I anisotropic diffusion	**5.91**	6.83	1125	0.94	0.72
Fuzzy II anisotropic diffusion	5.90	6.87	1140	0.94	0.72

wavelet filter results in more significant image quality improvement. It provides the best SNR,ENL and edginess measure. Edginess measure is closer to one indicating less smoothing effect. Type I fuzzy anisotropic diffusion algorithm filtered image remains relatively similar to the original image in terms of the luminance, contrast, and structure since its SSIM value is closer to 1. Looking at Table 7.3, the use of interval type II fuzzy anisotropic diffusion gives the optimum SNR improvement for human fingertip image. However, its edginess value is much less than the optimum value provided by the Wiener filter. Wavelet based algorithms provided the best CNR improvement. Similar results are found for the other test images (see Tables 7.4, 7.5, 7.6, and 7.7). Clearly, from the summarized results in the tables, the proposed type II fuzzy anisotropic based algorithm enhances the appearance of minute morphological features of human fingertip image, in this case, the presence of sweat glands in the epidermis. This is indicated by both the SNR improvement in table 7.3 and the enlarged image in Fig. 7.10F. The application of the interval type II fuzzy wavelet filter results in more significant image quality improvement for images obtained from an eye (human retina and rat retina). This is also apparent by the results summarized in the tables and by the change in image contrast in Fig. 7.11H and 7.12H.

7.8 Summary

The results show that speckle noise can be significantly reduced using an interval type II fuzzy set based thresholding in the wavelet domain and interval type II fuzzy set based anisotropic diffusion. The results from the experiments verify that interval type II fuzzy sets can reduce speckle pattern more effectively compared to standard filters. The algorithms provide overall better image quality in terms of SNR and edge preservation, and comparable performance in terms of the rest of the image metric functions. The Matlab implementation of the interval type II fuzzy wavelet algorithm took approximately $14 seconds$ and interval type II fuzzy anisotropic diffusion algorithm with 15 iterations took approximately $32 seconds$ to execute on a computer with Intel Core 2 DUO processor with 2.0 GB of RAM for test image dimensions of 1000 x 512 (lateral x axial) pixels. The interval type II fuzzy algorithms written in Matlab were optimized to use matrix manipulation by avoiding the use of nested loops. The wavelet transform was implemented with the FWT method from [20] with the help of Matlab built in convolution functions. The proposed speckle reduction algorithm requires significantly less run time as compared to previously published algorithms, while resulting in greater improvement in the image SNR [3]. The proposed algorithm requires a one-time optimization of the parameter each time the OCT system is set up. This is a somewhat time consuming task however, once optimization is achieved the algorithm can be applied to a batch of images with a very short image processing duration.

Chapter 8

Dispersion cancelled interferometry

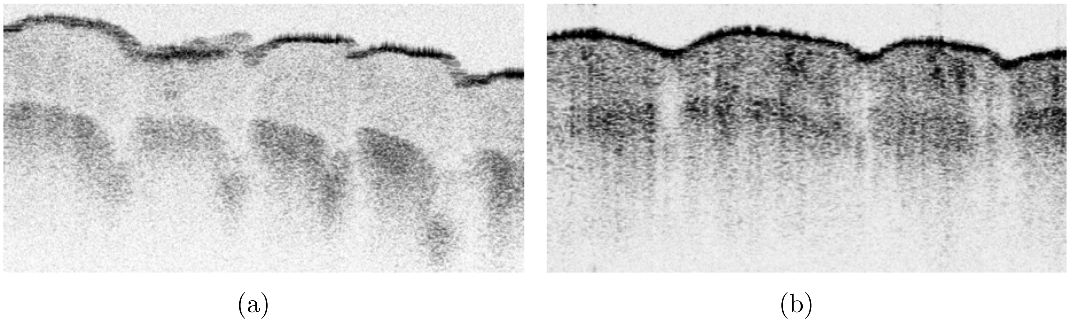

(a) (b)

Figure 8.1: a) Image without numerical dispersion compensation. b) Image processed by a numerical dispersion compensation algorithm mentioned in [66].

Fig. 8.1(a) and 8.1(b) shows human finger-tip images that were obtained with the FD-OCT system. The effect of dispersion compensation can be seen in these images. Fig. 8.1(a) is a non-compensated image and it has been degraded due to the effect of material dispersion. However, Fig. 8.1(b) is an image that has been compensated for dispersion via a numerical dispersion compensation algorithm from reference [66]. Dispersion compensated images show more detail than the non-compensated images. However, the numerical algorithm requires processing time and in a real-time application, this is not suitable. A novel technique to remove the effect of dispersion is needed so that it can be applied in real-time.

As mentioned before in Eqn. 2.4, the bandwidth of the low-coherence light source plays a vital role in the determination of the axial resolution in OCT. However, use of broad bandwidth light source creates a problem for OCT. A phenomena known as, “chromatic (group velocity) dispersion”, limits the axial resolution in OCT. This phenomena is due to the use of broad bandwidth light source and it broadens the interferometric autocorrelation function (axial point spread function).

Due to the chromatic dispersion, the different frequencies which make up the broad bandwidth light source, propagate at different velocities. This changes the phase of the optical signal but not the bandwidth of the signal [11]. In the Michelson interferometer in Fig. 2.2, if there is a significant mismatch in the dispersion of group velocity between the reference and the sample arms, then the interferometric autocorrelation function will broaden and thus will decrease the axial resolution [11].

In optical coherence tomography, there will be significant dispersion in the fiber optics based Michelson interferometer and the sample itself, especially if the sample is a human eye. As the optical bandwidth and the sample thickness increases, the effect of broadening becomes more severe. Due to the dispersion mismatch between the interferometer arms of the OCT system, the peak hieght of the interference envelope is also degraded [11]. This results in the reduction of the system's dynamic range and will reduce the contrast of the OCT images.

The effects of dispersion can be compensated by a computational algorithm given in reference [66]. This is an iterative procedure that modifies the phase of the interferogram by optimizing for image sharpness. A similar procedure is described in [8]. Both of these algorithms require computational time once the data has been obtained. This is not suitable for real-time application. Thus, an efficient way to compensate for dispersion is required.

In quantum metrology, quantum mechanical features, such as entanglement and squeezed light are used to improve the sensitivity of measurement devices [18], [28]. In references [58, 59, 14], a two-photon interferometer, based on frequency-entangled photon pairs, has been demonstrated to be insesntive to all even orders of dispersion. Using this "Quantum dispersion cancellation" effect, a quantum-optical coherence tomography was developed in reference [1] and a proof-of-principle was demonstrated experimentall in reference [40].

Dispersion cancellation is staightforward in quantum interferometry, but the methods proposed so far in classical interferometry are not. Can we use the intuition derived from quantum technologies to achieve dispersion cancellation in a simpler way in a classical interferometer [6, 45]? In the work that follows, dispersion cancellation achieved using only a classical light source, linear optics, and frequency-correlated detection is shown.

8.1 Theory

A nonclassical two-photon interferometer is shown in Fig. 8.2a. The upper path is of length, L_1, and the lower path is of length, $L_2 = L_1 + \Delta$. A nonlinear crystal, pumped by a narrow bandwidth laser of frequency $2\omega_0$, generates photon pairs with central frequency ω_0, via parametric down-conversion into the upper and lower paths of the interferometer in the state given by Eqn. 8.1,

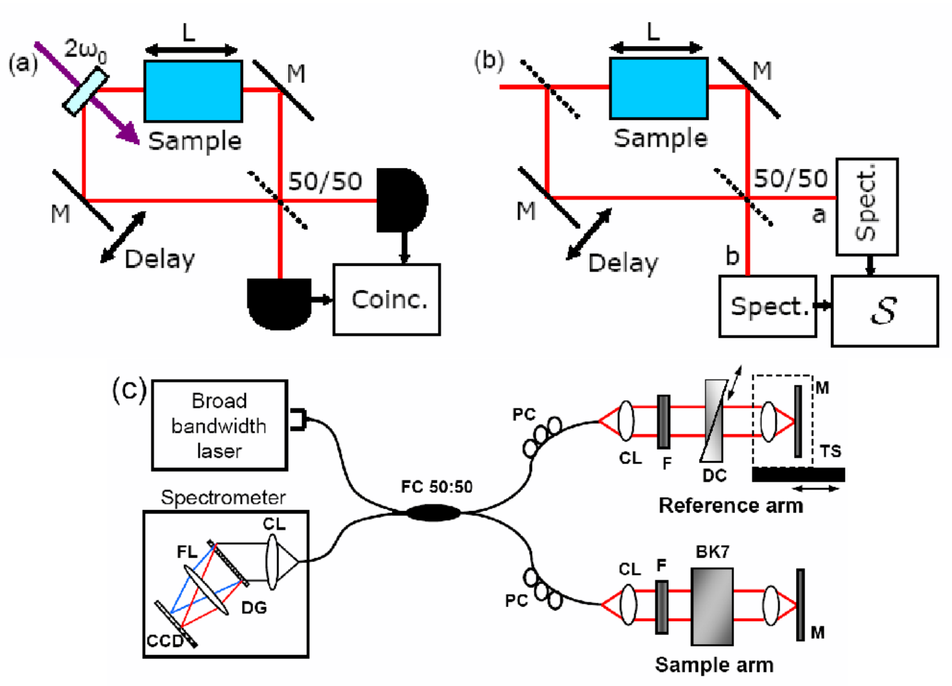

Figure 8.2: Dispersion cancellation interferometry in a a) Two photon interferometer using frequency-entangled photon pairs [58, 59], and b) a white-light Mach-Zehnder interferometer with frequency-correlated detection. These interferometers and their expected output signals are described in the text. Coinc. is coincidence detection; S describes a function of the output from the spectrometers. c) Experimental realization. A broadband laser is the source for a fibre-based two-path (Michelson) interferometer. The setup uses a 50/50 beamsplitter (FC 50 : 50), polarization controllers (PC), collimating lenses (CL), neutral-density filters (F), two BK7 prisms for dispersion control (DC), a translation stage (TS), mirrors (M), and a spectrometer. The spectrometer contains a CL, a diffraction grating (DG), and focusing lens (FL). The image is obtained from [46] with the authors permission.

$$|\psi\rangle = \int d\delta\omega A(\omega_0 + \delta\omega)|\omega_0 + \delta\omega\rangle_1 |\omega_0 - \delta\omega\rangle_2 \tag{8.1}$$

The subscripts 1 and 2 are mode labels, and $A(\omega_0 + \delta\omega)$ is the amplitude for a pair of photons of frequencies $\omega_0 + \delta\omega$ in mode 1 and $\omega_0 - \delta\omega$ in mode 2. Due to energy conservation, the sum of the frequencies in each term of the superposition is fixed - this is a frequency-entangled state with perfect frequency anti-correlation. At the 50/50 beamsplitter the photons are interferometrically combined and are detected by two single-photon counting detectors. The number of coincident photon detected as a function of the optical delay, Δ is the signal of interest.

Insertion of a dispersive, lossless medium of length, L, in the upper path of the interferometer results in a frequency-dependent phase shift, $\phi_M(\omega) = k_M(\omega)L$, where $k_M(\omega)$ is the wavevector at frequency, ω, in the material. Eqn. 8.2 shows the series expansion of $k_M(\omega)$ about ω_0:

$$k_M(\omega) \approx k(\omega_0) + \frac{dk}{d\omega}\,|_{\omega_0}\,\delta\omega + \frac{1}{2}\frac{d^2k}{d\omega^2}\,|_{\omega_0}\,\delta\omega^2 + ... \tag{8.2}$$

The inverse of the group velocity, v_g at ω_0 is represented by the first derivative and leads to a shift in the centre of the interference pattern. The second derivative is the leading-order dispersive term. Due to this second derivative, there is loss of both spatial resolution and contrast in low-coherence interferometry. This loss is represented by the broadening of the width and reduction of height (visibility) of the interference pattern.

Following [59], the following assumption is made: $A(\omega_0 + \delta\omega) = A(\omega_0 - \delta\omega)$, i.e., the amplitude is symmetric about the central frequency ω_0. This leads to Eqn. 8.3, which is the expected coincidence rate, as a function of Δ.

$$c(\Delta) \propto \int d\delta\omega |A(\omega_0 + \delta\omega)|^2 \left\{1 - cos\left[\frac{2\delta\omega(L+\Delta)}{c} - 2L\frac{dk}{d\omega}\delta\omega\right]\right\} \tag{8.3}$$

The expression is in agreement with reference [59], but uses slightly different notation. Notice that the second derivative does not appear - this is the dispersion cancellation. In fact, all higher-order even derivatives are cancelled. Maximum destructive interference occurs when the argument of the cosine term is zero for every frequency in the integral. This happens when the extra group delay imposed by the material is balanced by extra optical delay in the other arm of the interferometer. We will refer back to this expression when describing our classical system.

Now consider the Mach-Zehnder interferometer in Fig. 8.2b. The dimensions and mode labels of this interferometer are identical to that described in Fig. 8.2a, as is the dimension of the dispersive material; both beamsplitters are 50/50. $I(\omega)$ is the intensity spectrum of the input light. The intensities registered by the spectrometers for a delay position, Δ, and frequency, ω, in the outputs are labeled a and b. Eqn. 8.4 and 8.5 represents the registered intensities.

$$I_a(\omega, \Delta) = I(\omega)cos^2\left[\frac{(\Delta + L)\frac{\omega}{c} - \phi_M(\omega)}{2}\right] \tag{8.4}$$

$$I_b(\omega, \Delta) = I(\omega)sin^2\left[\frac{(\Delta + L)\frac{\omega}{c} - \phi_M(\omega)}{2}\right] \tag{8.5}$$

Each of these intensities is affected by all orders of dispersion in the series expansion of $\phi_M(\omega)$.

Quantum dispersion cancellation is a result of frequency-entanglement in fourth-order, i.e., coincidence, detection. Our approach seeks to mimic this effects as closely as classical physics allows. We use frequency correlations, the classical analogue to entanglement, and measure a fourth-order signal, achieved by multiplying pairs of intensity measurements. Specifically, we measure the signal, S,

$$S(\Delta) = \int d\delta\omega I_a(\omega_0 + \delta\omega) I_b(\omega_0 - \delta\omega) \tag{8.6}$$

The integrand of this function is the product of two intensities with an energy sum of $2\omega_0$. We use Eqn. 8.4 and 8.5 and assume, as we did in the quantum case, that the input spectrum is symmetric about ω_0, i.e., $I(\omega_0 + \delta) = I(\omega_0 - \delta)$, to obtain Eqn. 8.7.

$$S(\Delta) = \int d\delta\omega [I(\omega_0 + \delta\omega)]^2 \left\{ \begin{array}{l} 1 - \frac{1}{2} cos\left[\frac{2\delta\omega(L+\Delta)}{c} - 2L\frac{dk}{d\omega}\delta\omega\right] \\ -\frac{1}{2} cos\left[\frac{2\omega_0(L+\Delta)}{c} + 2Lk_0 + L\frac{d^2k}{d\omega^2}(\delta\omega)^2\right] \end{array} \right\} \tag{8.7}$$

Eqn. 8.7 represents the signal of interest from our classical system and can be directly compared with the quantum signal in Eqn. 8.3. The argument in the first cosine term is identical to the quantum expression and describes a dispersion cancelled interference dip. The second cosine term does not appear in the quantum case. However, its argument has only weak dependence on the frequency difference $\delta\omega$ (the integration variable) through the dispersion term. The second term describes a rapidly oscillating component, with wavelength $\lambda_0 = \frac{\pi c}{\omega_0}$, with a slowly decaying envelope. Due to the separation of length-scales between the first and the second term, the unwanted fast oscillation in the final data can be removed with a low-pass Fourier filter. The other feature of interest in the classical expression of Eqn. 8.7 is that the first term is multiplied by 1/2. This imposes the well-known classical limit of 50% on the destructive interference visibility in two-photon interferometers [23, 17]. The signal S is the classical analogue to the Hong-Ou-Mandel dip [23] and contains the same resistance to dispersion as its quantum counterpart.

8.2 Experimental Results

The experimental setup is shown in Fig. 8.2c. A compact, fiber-pigtailed, femtosecond laser (Femtolasers Inc., centre wavelength $792nm$, bandwidth FWHM $154nm$, average power $60mW$) was coupled to a fiber-based Michelson interferometer. Broad bandwidth optical and fiber optic components were chosen to support propagation of the entire laser bandwidth with minimal spectral and power losses. A pair of BK7 prisms mounted on miniature translation stages in the reference arm of the system were used to precisely compensate material dispersion mismatch between the two arms of the interferometer. The focusing lens and the mirror in the reference arm of the system were mounted on a computer-controlled translation stage for variable optical delay. The interference pattern generated by light reflected from the sample and reference mirrors was detected with a high-resolution ($0.09nm$) and high-speed ($20kHz$ readout rate) spectrometer and recorded by a computer. The spectrometer utilized a 4096 pixel linear-array CCD camera and it was calibrated for the spectral range $607nm$ to $1012nm$.

The correlation signal function S is calculated in the following way. $I_a(\lambda, \Delta)$ was obtained by reading the spectrometer for each motor position. The scale was converted from wavelength to frequency and a non-linear interpolation was used to extract intensities at evenly spaced intervals. $I(\omega)$ was obtained by measuring the intensity from the sample and reference arm separately and doubling their sum. Using the Energy conservation, $I(\omega) = I_a(\omega, \Delta) + I_b(\omega, \Delta)$, the value of $I_b(\omega, \Delta)$ was obtinaed. Note, there was no need for a second spectrometer. This is not the case in the previous experiments. To satisfy the assumption in our theory that $I(\omega) = I(2\omega_0 - \omega)$, $I(\omega)$ and $I_a(\omega)$ was multiplied by a mirror version of $I(\omega)$ with respect to the center frequency ω_0. The integral S was approximated by a discrete sum over 4096 equally spaced energies. For comparison purpose, the total intensity registered by the spectrometere was obtained by adding the intensity measured at each pixel at a fixed translation stage position. This signal is equivalent to a signal that one would have been measured by a square-law detector, such as a photo-diode.

8.2.1 Experiment 1

To demonstrate dispersion cancellation with the classical interferometer, several different experiments were conducted. First of all, measurements were made in a dispersion-balanced system with a mirror and when a flat, uncoated, BK7 optical window of thickness $16.80.009mm$ was introduced into the sample arm. Fig. 8.3, shows the results of this experiment. For each measurement, the reference mirror was translated in steps of $0.1\mu m$ and the spectral interference fringes were acquired with a readout time of $60\mu s$ per step at least 4 orders of magnitude shorter as compared with typical measurement times in entangled photon experiments. Fig. 8.2a and 8.3b shows two examples of the total intensity measured as a function of the translation stage position for the cases where no glass (a) and a $16.800 \pm 0.009mm$ thick BK7 glass window (b) were inserted into the sample arm of the interferometer. Due to the material dispersion, the intensity interference pattern is dramatically broadened, from $(2.04 \pm 0.03)\mu m$ to $(88.6 \pm 0.9)\mu m$, and the visibility of the fringe is reduced [46], from 78% to 14%. According to [46], visibility is a measure of the contrast of interference. For oscillating interference, visibility is $V_osc = \frac{(I_Max - I_Min)}{(I_Max + I_Min)}$, where I_Max and I_Min are the maximum and minimum of the pattern. For interference dips the visibility is conventionally $V_dip = \frac{(I_Max - I_Min)}{I_Max}$. Fig. 8.3 clearly shows the detrimental effect that dispersion has on interference.

The corresponding correlation signal function, S, for the two cases of no material dispersion and $16.800mm$ BK7 glass are shown in Fig. 8.3c) and 8.3d), respectively. Each of these signals has a sharp dip in addition to a rapidly oscillating component

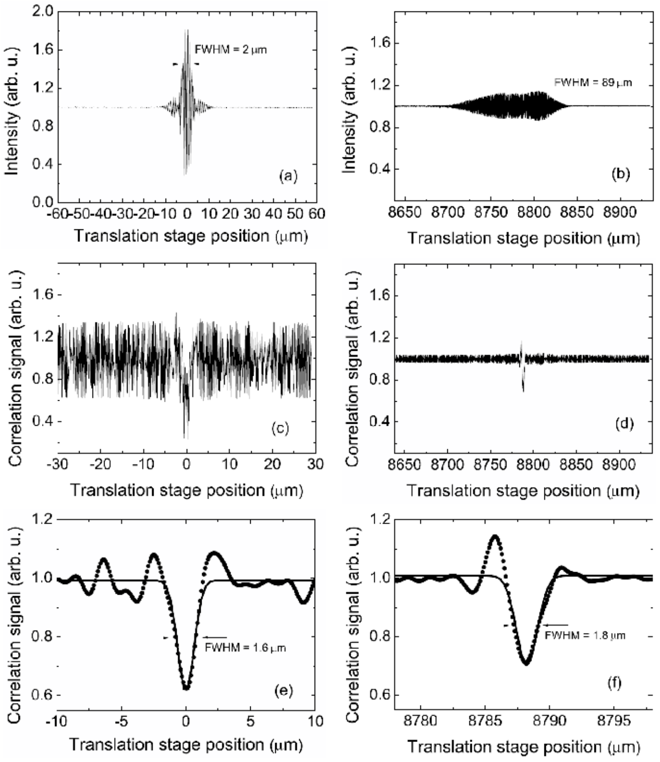

Figure 8.3: Dispersion cancelled interferometry experimental data 1. a) & b) Total intensity, as measured by summing the intensities measured at each frequency by the spectrometer, versus motor position with 0 and 2 passes through $(16.800 \pm 0.009)mm$ of BK7 glass in the sample arm of the interferometer, respectively. c) & d) S versus motor position with no BK7 and $16.8mm$ of BK7 in the sample arm. In e) & f), the data from c) & d) have been subject to a Fourier low-pass filter to remove rapidly oscillating terms. The solid curves are Gaussian fit to the experimental data to obtain the FWHM. These data show that S broadens by only about 14% by addition of the glass while the standard intensity interference pattern is broadened by 4250%.

that corresponds to the final cosine term in 8.7. It is important to note that the magnitude of the fast oscillating signal is reduced when a large amount of dispersion is present in the interferometer. A similar effect was observed when the measurements were simulated with a computer model. Fig. 8.3e and 8.3f is obtained after applying a low-pass Fourier filter to the data from Fig. 8.33c) and 8.3d) to remove the fast oscillating term. By fitting a Guassian function to the dips, the full width half maxima (FWHM) and the centers were obtained. While the intensity interference pattern is broadened by 4250% of its original size due to material dispersion, the correlation signal S is broadened only by 14%. The visibilities of the correlation signal dip [46] is reduced from (40.80.14)% and (30.00.3)% for Fig. 8.3e) and 8.3f), respectively (recall that the theoretical maximum visibility is 50%). The deviations from the Gaussian shape of the fitting function are due partially to the non-Gaussian spectrum of the laser as well as the present of higher-order material dispersion.

8.2.2 Experiment 2

The second term of Eqn. 8.7 describes cross-correlation term in the correlated signal, S. In OCT, cross correlation terms appear for every pair of reflective interfaces in the imaged sample. In reference [1], the presence of such cross-correlated terms, located exactly midway between every pair of correlation dips was described theoretically and observed experimentally for the case of Quantum OCT. The cross-correlation terms can be either a dip or a peak. The sign (dip or peak) and magnitude of the cross-correlation terms are dependent on the phase difference between the corresponding pairs of reflective interfaces in the imaged object, while the FWHM of the cross-correlation terms are determined by the dispersion of the medium between the pair of reflective interfaces.

Since regular OCT uses the subtle refractive index changes between cellular components, for example cell membranes, organelles and cytoplasm in biological tissue, to construct a reflectivity map (an image) of the imaged object, the application of DC-OCT for imaging biological media is impeded by the presence of numerous cross-correlation terms that will appear as image artefacts. A novel technique has been developed for removing or suppressing cross-correlation peaks in the correlated OCT signal. The goal of the following experiments is to evaluate the effectiveness of this method as the number of reflective interfaces in the imaged sample increases.

The position and magnitude of the cross-correlation peak is dependent on the phase difference between the two glass interfaces, and thus is related to the refractive index and physical thickness of the glass coverslip. The cross correlation peak can be removed by reprocessing the same data set to induce an additional 2π phase shift that will flip the sign, but preserve the magnitude of the cross-correlated peak, without affecting the correlation dips. If the optical thickness, equal to the product of the refractive index and the physical thickness of the glass slide, is known, a 2π phase shift can be induced by shifting the central wavelengths of the reference and sample interference spectra by a difference $\Delta\lambda = \frac{\lambda^2}{2 * nL}$, where $\Delta\lambda$ is the shift in wavelengths, λ is the central wavelength of the spectra, n is the refractive index and L is the physical thickness of the glass coverslip. In our case, the thickness and refractive index of the glass slide can be measured separately, or the optical thickness of the sample can be evaluated precisely from the locations of the intensity peaks of in the case of dispersion compensated measurement. The second method is more general and can be applied in cases when the imaged object has a multilayered structure. By summing the original and reprocessed data set, the cross-correlation peak can be cancelled with high precision. The summation of the data sets also reduces the residual random noise which results in improvement of the SNR of the correlated OCT signal.

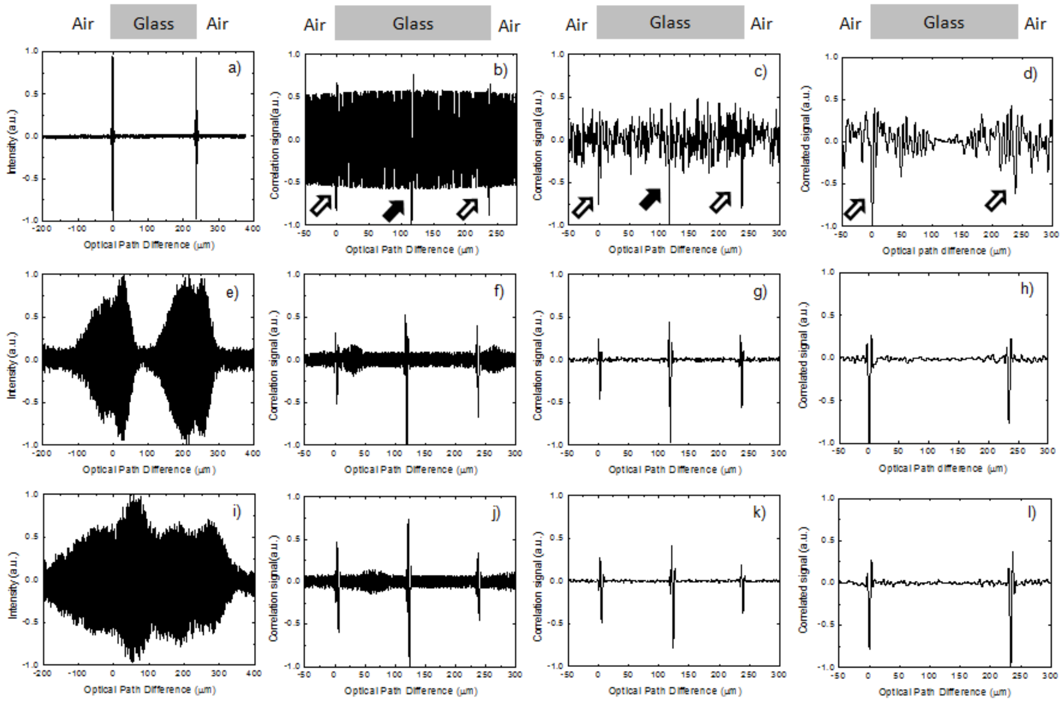

Figure 8.4: Dispersion cancelled interferometry experimental data acquired from a single glass coverslip (schematic of the sample shown above the graphs). Regular OCT intensity data containing the interference fringes corresponding to the air-glass and glass-air interfaces (a), raw correlation signal containing 2 correlation dips corresponding to the air-glass and glass-air interfaces (box arrows) and an autocorrelation peak (dark arrow) located midway between the correlation dips (b), filtered correlation signal (c) and filtered correlation signal with autocorrelation peaks removed (d) acquired with a an OCT system dispersion compensated to the front interface of the glass coverslip. Similar signals acquired with a dispersion mismatched OCT system with $19mm$ (e - h) and $38mm$ (i - l) BK7 glass windows placed in the sample arm of the imaging system.

The next experiment involved imaging a single glass coverslip with approximate thickness of $150\mu m$ and refractive index of 1.54. Data was acquired under three different conditions: i) with dispersion compensated OCT system (dispersion is matched for the front interface of the glass coverslip), ii) with a dispersion mismatched OCT system, with $19mm$ thick BK7 window placed before the sample and iii) with a dispersion mismatched OCT system, with $38mm$ thick BK7 window placed before the sample. Results from this experiment are presented in Fig. 8.4. The first column of Fig. 8.4 (a, e and i) shows the intensity fringe pattern detected with the standard OCT method. In the case of dispersion compensated system (a), the intensity signal shows clearly distinct fringes that correspond to the front and back coverslip interfaces. As BK7 glass windows are added infront of the coverslip, the fringe patterns broaden assymetrically (e) to the extent that the two fringe patters overlap (i) and the signal intensity is reduced dramatically. Under such conditions the regular OCT detection cannot resolve the two glass coverslip interfaces and the contrast of the OCT image is significantly reduced. The second column of Fig. 8.4 (b, f, j) shows the raw dispersion compensated OCT correlation signal, which as theoretically predicted, contains two dips that correspond to the coverslip interfaces and one cross-correlation peak positioned midway between the dips. The large rapidly oscillating background noise component in the graphs corresponds to the final cosine term in Eqn. 8.7 and can be easily removed with a band pass frequency filter (Fig. 8.4 c, g, k). Results from the data processing are presented in Fig. 8.4 (d, h, l) for the three cases of dispersion mismatch in the OCT imaging systems. The figures clearly show that the cross correlation peak can be successfully removed from the DC-OCT data.

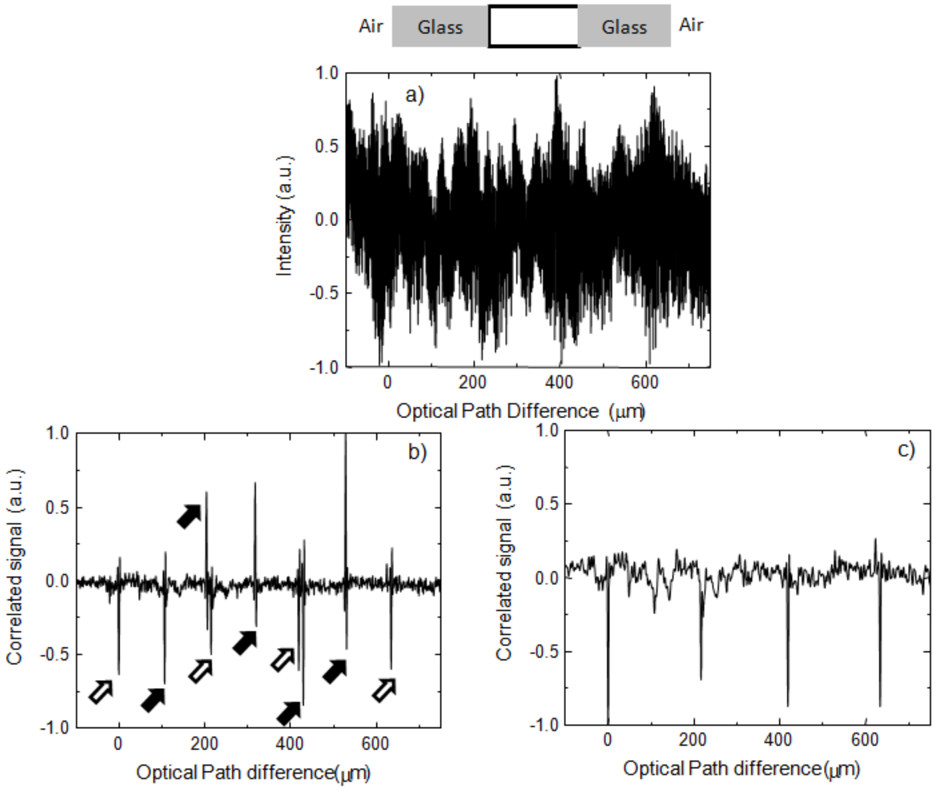

Figure 8.5: Dispersion cancelled interferometry experimental data acquired from a sample composed of 2 glass coverslips separated by an air gap of $230\mu m$ (schematic of the sample shown above the graphs). Regular OCT intensity data containing the interference fringes corresponding to the air-glass and glass-air interfaces (a), raw correlation signal containing 4 correlation dips corresponding to the air-glass and glass-air interfaces (box arrows) and 6 cross-correlation peaks (dark arrows) located midway between each pair of correlation dips (b), filtered correlation signal with the cross-correlation peaks removed (c), acquired with a dispersion mismatched OCT system with $38mm$ BK7 glass windows placed in the sample arm of the imaging system.

Although removal of the cross correlation peak may be straight forward, such a procedure becomes more complicated with increasing the number of layers in the imaged object. Fig. 8.5 shows the results from an OCT measurement from a sample comprised of 2 glass coverslips separated by an air gap. A schematic of the multilayered sample is shown above the graphs in Fig. 8.5. A $38mm$ thick BK7 window was placed above the sample to induce significant dispersion mismatch in the OCT system. The effect of the dispersion mismatch is observed as partial overlap between the fringe patterns in the regular OCT signal, which makes the glass-air interfaces indistinguishable from a standard OCT image. The length of the air gap was chosen to match almost exactly the optical thickness of a single glass coverslip. In this case, the 4 air-glass and glass-air interfaces in the sample result in 4 correlation dips (box arrows) and 6 cross-correlation peaks (dark arrows) in the dispersion compensated OCT data. Since the thickness of the air gap was designed to match the optical thickness of a single coverslip, Fig. 8.5b shows only 5 cross-correlation peaks, since the two peaks corresponding to the pairs $1 - 4$ and $2 - 3$ of the glass-air interfaces overlap each other. Notice also that some of the cross-correlation peaks are actually 'dips', resulting from the fact that they correspond to slightly different phase shifts. Because of this condition, simultaneous and complete removal of all cross-correlation peaks by inducing a single 2π phase shift and summing 2 data sets is not possible. Fig. 8.5c shows the removal of all cross-correlation peaks by inducing multiple phase shifts and summing the resulting data sets.

Chapter 9

Conclusions and Future Work

For the first time, a high speed, ultrahigh resolution FD-OCT system operating in the 1060nm wavelength range has been built. This system provides the dual advantage of better visualization of choroidal and scleral tissue and the potential for simultaneous in-vitro or in-vivo imaging of retinal morphology and function.

Two novel algorithms for reducing speckle noise in OCT images, based on interval type II fuzzy set was introduced in this manuscript. One algorithm involved thresholding in the wavelet domain and the other involved anisotropic diffusion. The algorithms improved the SNR, CNR, and ENL values and the improvement is higher than the values for the previously published speckle reduction algorithms that have proven to provide excellent results (Wiener and adaptive Lee algorithms). The fuzzy type II technique is relatively slower as compared to fast processing algorithms such as Wiener, median, and adaptive Lee. The effectiveness of the algorithm in reducing speckle noise was shown by applying it to six different OCT images. The interval type II fuzzy wavelet algorithm performs well for images involving the eye while the interval type II fuzzy anisotropic diffusion algorithm performs well for human fingertip images. SNR improvement of $\sim 13dB$ for a human fingertip image was achieved by type II fuzzy anisotropic diffusion algorithm. Similarly, SNR improvement of $\sim 11dB$ for a human fovea image by type II fuzzy wavelet algorithm was achieved.

The algorithms can be changed effortlessly to include other information from the image to further improve speckle reduction performance. For example, by adding new fuzzy rules that take into account the image features of interest, the algorithms can be tuned specifically for different type of images. For interval type II fuzzy anisotropic diffusion algorithm, in addition to the image gradient, the second derivative of the image can be used to calculate the diffusion coefficient. This will be done in the future work.

Theory for cancelling even-order dispersion in low-coherence interferometry was derived and experimentally demonstrated. Dispersion cancellation need not be complicated; the scheme introduced in this manuscript is a completely classical, linear-optical system with no exotic light sources or nonlinear optics. Both the quantum and classical techniques obtain their power from two seemingly contradictory constraints: a wide bandwidth of frequencies provides good time resolution, whereas narrow frequency correlations reduce sensitivity to dispersion. The approach presented here should be applied to other quantum effects to understand which are due to classical correlation, as opposed to entanglement. The experimental barrier for dispersion cancellation in low-coherence interferometry and optical coherence tomography has been reduced. The next step would be to apply the technique to 2D OCT tomograms.

References

[1] A. F. Abouraddy, M. B. Nasr, B. E. A. Saleh, A. V. Sergienko, and M. C. Teich. Quantum-optical coherence tomography with dispersion cancellation. *Physical Review A*, 65(5):053817–6, 2002. 63, 69

[2] T. Acharya and A. K. Ray. *Image Processing Principles and Applications.* A John Wiley and Sons, Inc., Hoboken, New Jersey, 2005. 18

[3] D. C. Adler, T. H. Ko, and J. G. Fujimoto. Speckle reduction in optical coherence tomography images by use of a spatially adaptive wavelet filter. *Optics Letters*, 29(24):2878–2880, 2004. 14, 15, 16, 17, 31, 42, 43, 61

[4] S. Aja, C. Alberola, and J. Ruiz. Fuzzy anisotropic diffusion for speckle filtering. In *Proc. IEEE International Conference on Acoustics, Speech, and Signal Processing.*, pages 1261–1264, 2001. 16, 35, 39

[5] P. Baroni, G. Guida, and S. Mussi. Enhancing cognitive plausibility of uncertainty calculus: A common-sense-based approach to propagation and aggregation. *IEEE Trans. Systems, Man, and Cybernetics*, 28:394–407, 1998. 24

[6] R. S. Bennink, S. J. Bentley, and R. W. Boyd. Two-photon coincidence imaging with a classical source. *Physical Review Letter*, 89:113601–113605, 2002. 63

[7] F. Catte, P. L. Lions, J. M. Morel, and T. Coll. Image selective smoothing and edge detection by nonlinear diffusion. *SIAM J. Numer. Anal.*, 29:182–193, 1992. 34

[8] B. Cense, N. Nassif, T. Chen, M. Peirce, S. H. Yun, B. Park, B. Bouma, G. Tearney, and J. de Boer. Ultrahigh-resolution high-speed retinal imaging using spectral-domain optical coherence tomography. *Optics Express*, 12(11):2435–2447, 2004. 6, 9, 63

[9] A. E. Desjardins, B. J. Vakoc, W. Y. Oh, S. M. R. Motaghiannezam, G. J. Tearney, and B. E. Bouma. Angle-resolved optical coherence tomography with sequential angular selectivity for speckle reduction. *Optics Express*, 15:6200–6209, 2007. 17

[10] C. Dorrer, N. Belabas, J.P. Likforman, and M. Joffre. Spectral resolution and sampling issues in fourier-transform spectral interferometry. *J. Opt. Soc. Am. B*, 17(10):1795–1802, 2000. 8, 9

[11] W. Drexler. Ultrahigh-resolution optical coherence tomography. *J. Biomed. Opt.*, 9(1):47–74, January 2004. 1, 13, 63

[12] D. C. Fernandez and H. M. Salinas. Evaluation of a nonlinear diffusion process for segmentation and quantification of lesions in optical coherence tomography images. In *Proc. Society Of Photo Optical Engineers. 5747*, pages 1834–1843, San Jose, CA, 2005. 16

[13] D. C. Fernandez, H. M. Salinas, and C. A. Puliafito. Automated detection of retinal layer structures on optical coherence tomography images. *Opt. Express*, 13:10200–10216, 2005. 16

[14] J. D. Franson. Nonlocal cancellation of dispersion. *Physical Review A*, 45:3126–3132, 1992. 63

[15] J. G. Fujimoto, S. De Silvestri, E. P. Ippen, C. A. Puliafito, R. Margolis, and A. Oseroff. Femtosecond optical ranging in biological systems. *Optics Letters*, 11(3):150–153, 1986. 3

[16] G. Gerig, O. Kubler, R. Kikinis, and F. A. Jolesz. Nonlinear anisotropic filtering of mri data. *IEEE Trans. Med. Imaging*, 11:221–232, 1992. 39, 40

[17] R. Ghosh and L. Mandel. Observation of nonclassical effects in the interference of two photons. *Phys. Rev. Lett.*, 59:1903–1905, 1987. 66

[18] V. Giovannetti, S. Lloyd, and L. Maccone. Quantum-enhanced measurements: Beating the standard quantum limit. *Science*, 306:1330–1336, 2004. 63

[19] D. Gnanadurai and V. Sadasivam. Undecimated wavelet based speckle reduction for sar images. *Pattern Recognition Letters*, 26:793–800, 2005. 30

[20] R. C. Gonzalez and R. E. Woods. *Digital Image Processing.* Prentice Hall, Upper Saddle River, New Jersey, 2002. 28, 29, 31, 61

[21] T. Greiner, Ch. Loizou, M. Pandit, J. Mauruschat, and F. W. Albert. Speckle reduction in ultrasonic imaging for medical applications. In *Proc. IEEE International Conference on Acoustics, Speech and Signal Processing*, pages 2993–2996, New York, USA, April 1991. 16

[22] A. J. Healey and S. Leeman. A complex z-transform technique for speckle reduction. In *Proc. IEEE Ultrasonics Symposium*, pages 1109–12, FL, USA, December 1991. 15

[23] C. K. Hong, Z. Y. Ou, and L. Mandel. Measurement of subpicosecond time intervals between two photons by interference. *Phys. Rev. Lett.*, 59:2044–2046, 1987. 66

[24] S. Intajag, V. Tipsuwanpon, and F. Cheevasuwit. Anisotropic diffusion in synthetic aperture radars. In *Proc. Canadian Conference on Electrical and Computer Engineering*, pages 277–280, Saskatoon, Saskatchewan, 2005. 40

[25] F. O. Karray and C. de Silva. *Soft Computing and Intelligent Systems Design - Theory, Tools, and Applications.* Addison Wesley, London, England, 2005. 20

[26] J. Kim, D. T. Miller, E. Kim, S. Oh, J. Oh, and T. E. Milner. Optical coherence tomography speckle reduction by a partially spatially coherent source. *Journal of Biomedical Optics*, 10:64034–64039, 2005. 16

[27] J. Koenderink. The structure of images. *Biol. Cybern.*, 50:363–370, 1984. 33

[28] D. Leibfried, E. Knill, J. Britton, R. B. Blakestad, an dD. B. Hume J. Chiaverini, W. M. Itano, J. D. Jost, C. Langer, R. Ozeri, R. Reichle, and D. J. Wineland. Creation of a six-atom schrodinger cat state. *Nature*, 438:639–642, 2005. 63

[29] Y. Li and C. Moloney. Selective wavelet coefficient soft-thresholding scheme for speckle noise reduction in sar images. In *IEEE Workshop on Nonlinear Signal and Image Processing*, Mackinac Island, USA, 1997. 25, 26

[30] S.J. Lim. *Two-Dimensional Signal and Image Processing.* Prentice Hall, Upper Saddle River, New Jersey, 1990. 44, 54

[31] Z. Lin and Q. Shi. An anisotropic diffusion pde for noise reduction and thin edge preservation. In *Proc. 10th Int. Conf. Image Analysis and Processing*, pages 102–107, Los Alamitos, CA, 1999. 34

[32] T. Loupas, W. N. Mcdicken, and P. L. Allan. An adaptive weighted median filter for speckle suppression in medical ultrasonic images. *IEEE TRANSACTIONS ON CIRCUITS AND SYSTEMS*, 36(1):129–35, 1989. 15

[33] Y.H. Lu, , S.Y. Tan, T.S. Yeo, W.E. Ng, I. Lim, and C.B. Zhang. Adaptive filtering algorithms for sar speckle reduction. In *Proc. IEEE 1996 International Geoscience and Remote Sensing Symposium*, pages 67–69, New York, USA, May 1996. 15, 16, 44, 54

[34] R. Leitgeb A.F. Fercher M. Pircher, E. Gtzinger and C. K. Hitzenberger. Speckle reduction in optical coherence tomography by frequency compounding. *Journal of Biomedical Optics*, 8:565–569, 2003. 16

[35] S. G. Mallat. A theory for multiresolution signal decomposition: the wavelet representation. *Pattern Analysis and Machine Intelligence*, 11:674–693, 1989. 23

[36] J. M. Mendel. *Uncertain Rule-Based Fuzzy Logic Systems: Introduction and New Directions.* Prentice Hall, Upper Saddle River, New Jersey, 2001. 20

[37] J. M. Mendel and R. I. John. Type-2 fuzzy sets made simple. *IEEE Trans. Fuzzy Syst.*, 10(2):117–27, April 2002. 20, 21

[38] J. M. Mendel, R. I. John, and F. Liu. Interval type-2 fuzzy logic systems made simple. *IEEE Trans. Fuzzy Syst.*, 14(6):808–21, December 2006. 21

[39] B. E. Bouma N. Iftimia and G. J. Tearney. Speckle reduction in optical coherence tomography by path length encoded angular compounding. *Journal of Biomedical Optics*, 8:260–263, 2003. 17

[40] M. B. Nasr, B. E. A. Saleh, A. V. Sergienko, and M. C. Teich. Demonstration of dispersion-cancelled quantum-optical coherence tomography. *Physical Review Letters*, 91(8):083601–4, 2003. 63

[41] A. Ozcan, A. Bilenca, A. E. Desjardins, B. E. Bouma, and G. J. Tearney. Speckle reduction in optical coherence tomography images using digital filtering. *J. Opt. Soc. Am. A*, 24:1901–1910, 2007. 16, 17, 42, 54

[42] P. Perona and J. Malik. Scale-space and edge detection using anisotropic diffusion. *IEEE Trans. Pattern Anal. and Mach. Intell.*, 12:629–639, 1990. 33, 34, 40

[43] B. Povazay, K. Bizheva, B. Hermann, A. Unterhuber, H. Sattmann, A. Fercher, W. Drexler, C. Schubert, P. Ahnelt, M. Mei, R. Holzwarth, W. Wadsworth, J. Knight, and P. St. J. Russell. Enhanced visualization of choroidal vessels using ultrahigh resolution ophthalmic oct at 1050 nm. *Optics Express*, 11(17):1980–1986, 2003. 11

[44] P. Puvanathasan and K. Bizheva. Speckle noise reduction algorithm for optical coherence tomography based on interval type ii fuzzy set. *Optics Express*, 15(24):15747–15758, 2007. 17

[45] K. J. Resch, K. L. Pregnell, Prevedel1, A. Gilchrist, J. Pryde, J. L. OBrien, and A. G. White. Time-reversal and super-resolving phase measurements. *quant-ph*, 0511:0511214, 2005. 63

[46] K.J. Resch, P. Puvanathasan, J.S. Lundeen, M.W. Mitchell, and K. Bizheva. Classical dispersion-cancellation interferometry. *Optics Express*, 15(14):8797–8804, 2007. 64, 67, 68

[47] H. L. Resnikoff and R. O. Wells Jr. *Wavelet Analysis: The Scalable Structure of Information.* Springer, 1998. 23

[48] J. Rogowska and M. E. Brezinski. Evaluation of the adaptive speckle suppression filter for coronary optical coherence tomography imaging. *IEEE TRANSACTIONS ON CIRCUITS AND SYSTEMS*, 19(12):1261–1266, 2000. 15

[49] H. M. Salinas and D. C. Fernandez. Comparison of pde-based nonlinear diffusion approaches for image enhancement and denoising in optical coherence tomography. *IEEE Trans. Med. Imaging*, 26:761–771, 2007. 16, 42

[50] G. Sanchez-Ortiz and A. Noble. Fuzzy clustering driven anisotropic diffusion: Enhancement and segmentation of cardiac mr images. In *IEEE Nuclear Symp. and Med. Imag. Conf. 3*, pages 1873–1874, Piscataway, NJ, 1998. 35

[51] F. Sattar, L. Floreby, G. Salomonsson, and B. Lovstrom. Image enhancement based on a nonlinear multiscale method. *IEEE Trans. Image Process*, 6:888–895, 1997. 30

[52] J. M. Schmitt. Restoration of optical coherence images of living tissue using the clean algorithm. *Journal of Biomedical Optics*, 3(1):66–75, 1998. 15, 17

[53] J. M. Schmitt, S. H. Xiang, and K. M. Yung. Speckle in optical coherence tomography. *Journal of Biomedical Optics*, 4(1):95–105, 1999. 13, 14, 15

[54] J. M. Schmitt, S. H. Xiang, and K. M. Yung. Speckle in optical coherence tomography. *Journal of Biomedical Optics*, 4(1):95–105, 1999. 15

[55] S. Schulte, B. Huysmans, A. Pizurica, E. E. Kerre, and W. Philips. A new fuzzy-based wavelet shrinkage image denoising technique. *Lecture Notes in Computer Science*, 4179:12–23, 2006. 17, 20

[56] J. S. Schumann, C. A. Puliafito, and J. G. Fujimoto. *Optical Coherence Tomography of Ocular Diseases.* Slack Incoporated, Thorofare, New Jersey, second edition, 2004. 3, 4, 5

[57] J. Song and H.R. Tizhoosh. Fuzzy anisotropic diffusion: A rule-based approach. In *7th World Multiconference on Systemics, Cybernetics and Informatics Proceedings*, pages 241–246, Orlando, FL, 2003. 34, 35, 36, 40

[58] A. M. Steinberg, P. G. Kwiat, and R. Y. Chiao. Dispersion cancellation and high-resolution time measurements in a fourth-order optical interferometer. *Physical Review A*, 45:6659–6665, 1992. 63, 64

[59] A. M. Steinberg, P. G. Kwiat, and R. Y. Chiao. Dispersion cancellation in a measurement of the single-photon propagation velocity in glass. *Physical Review Letter*, 68:2421–2424, 1992. 63, 64, 65

[60] M. Mogensen F. Pedersen T. M. Jorgensen, L. Thrane and P. E. Andersen. Speckle reduction in optical coherence tomography images of human skin by a spatial diversity method. In *Proc. Society Of Photo Optical Engineers. 6627*, Munich, Germany. 16

[61] H. R. Tizhoosh. *Fuzzy Image Processing.* Springer-Verlag, 1997. 20

[62] H. R. Tizhoosh. Image thresholding using type ii fuzzy sets. *Pattern Recognition*, 38:2363–2372, 2005. 28, 36, 50, 51

[63] M. P. Wachowiak, R. Smolikova, A. S. Elmaghraby, and J. M. Zurada. Classification and estimation of ultrasound speckle noise with neural networks. In *Proc. IEEE International Symposium on Bio-Informatics and Biomedical Engineering*, pages 245–52, Los Alamitos, CA, November 2000. 16

[64] R. K. Wang. Reduction of speckle noise for optical coherence tomography by the use of nonlinear anisotropic diffusion. In *Proc. Society Of Photo Optical Engineers. 5690*, pages 380–385, San Jose, CA, 2005. 14, 15, 16

[65] Z. Wang and A. C. Bovik. A universal image quality index. *IEEE Signal Processing Letters*, 9:81–84, 2002. 42, 43

[66] M. Wojtkowski, V. Srinivasan, T. Ko, J. G. Fujimoto A. Kowalczyk, and J. Duker. Ultrahigh-resolution, high-speed, fourier domain optical coherence tomography and methods for dispersion compensation. *Optics Express*, 12(11):2404–2422, 2004. 6, 7, 8, 9, 62, 63

[67] K. M. Yung, S. L. Lee, and J. M. Schmitt. Phase-domain processing of optical coherence tomography images. *Journal of Biomedical Optics*, 4(1):125–36, 1999. 15

[68] L. A. Zadeh. Fuzzy sets. *Information Control*, 8:338–353, 1965. 18